The Astrophysical Journal, 933:80 (41pp), 2022 July 1 https://doi.org/10.3847/1538-4357/ac6d5e

Investigating Particle Acceleration by Dynamic Small-scale Flux Ropes behind Interplanetary Shocks in the Inner Heliosphere

Keaton Van Eck[1], Jakobus le Roux[1,2], Yu Chen[2], Ling Ling Zhao[1,2], and Noah Thompson[3]
[1] Department of Space Science, University of Alabama in Huntsville, Huntsville, AL 35805, USA; kte0002@uah.edu
[2] Center for Space Plasma and Aeronomic Research (CSPAR), University of Alabama in Huntsville, Huntsville, AL 35805, USA
[3] Department of Physics and Engineering, Whitworth University, Spokane, WA 99251, USA
Received 2022 February 2; revised 2022 May 3; accepted 2022 May 4; published 2022 July 5

Abstract

We recently extended our Parker-type transport equation for energetic particle interaction with numerous dynamic small-scale magnetic flux ropes (SMFRs) to include perpendicular diffusion in addition to parallel diffusion. We present a new analytical solution to this equation assuming heliocentric spherical geometry with spherical symmetry for all SMFR acceleration mechanisms present in the transport theory. With the goal of identifying the dominant mechanism(s) through which particles are accelerated by SMFRs, a search was launched to identify events behind interplanetary shocks that could be explained by our new solution and not classical diffusive shock acceleration. Two new SMFR acceleration events were identified in situ for the first time within heliocentric distances of 1 astronomical unit (au) in Helios A data. A Metropolis–Hastings algorithm is employed to fit the new solution to the energetic proton fluxes so that the relative strength of the transport coefficients associated with each SMFR acceleration mechanism can be determined. We conclude that the second-order Fermi mechanism for particle acceleration by SMFRs is more important than first-order Fermi acceleration due to the mean compression of the SMFRs regions during these new events. Furthermore, with the aid of SMFR parameters determined via the Grad–Shafranov reconstruction method, we find that second-order Fermi SMFR acceleration is dominated by the turbulent motional electric field parallel to the guide/background field. Finally, successful reproduction of energetic proton flux data during these SMFR acceleration events also required efficient particle escape from the SMFR acceleration regions.

Unified Astronomy Thesaurus concepts: Heliosphere (711); Interplanetary particle acceleration (826); Solar energetic particles (1491); Interplanetary physics (827)

1. Introduction

Since the late 1970s, the discussion surrounding increased fluxes of energetic particles has been dominated by shock acceleration and specifically diffusive shock acceleration (DSA; Jones & Ellison 1991). DSA describes the mechanism by which particles interact multiple times with the same shock via diffusive effects to amplify energy gain (Drury 1983). A single interaction with the shock would only result in miniscule energy gain proportional to the compression ratio, but diffusion effects allow the particles to interact with the shock multiple times, whereby the particles can achieve very high energies. The famous result of DSA is that the spectra for accelerated particles depends on the compression ratio of the shock (r) via a power-law index of $-3r/(r-1)$ (Jones & Ellison 1991). Steady-state DSA theory predicts that the accelerated energetic particle flux enhancements should peak at the shock structure itself, but numerous flux enhancements have been reported that do not coincide with shock structures. In order to address this issue, many studies have introduced time-dependent DSA effects (Cane et al. 1988; Lario et al. 2003; Zank et al. 2015). However, recent observations show unusual energetic particle flux enhancements that appear unrelated to DSA (Khabarova & Zank 2017), suggesting that acceleration processes that are related to magnetic reconnection in the solar wind could explain these anomalous flux enhancements (Khabarova et al. 2016; Khabarova & Zank 2017; Zhao et al. 2018). Many of these anomalous flux enhancements have been observed relatively far downstream of traveling shocks, i.e., farther than an effective diffusion length scale away from shock-accelerated particles (Zhao et al. 2018). Recent developments have stressed the intimate connection between shocks, strong turbulence, and magnetic reconnection (Karimabadi et al. 2014; Matsumoto et al. 2015; Zank et al. 2015; Vlahos & Isliker 2018).

While there has been a general consensus that efficient magnetic reconnection related energetic particle acceleration occurs in solar flare events near the surface of the Sun, until recently no evidence had been found that magnetic reconnection processes played an important role in energetic particle acceleration in the solar wind (e.g., Gosling et al. 2005). After reanalyzing the reconnection events studied by Gosling et al. (2005) on longer timescales, Khabarova & Zank (2017) discovered evidence for suprathermal particle acceleration. The authors theorized that the acceleration could be caused by dynamic magnetic islands in turbulent regions that often coexist with current sheets experiencing magnetic reconnection (Khabarova et al. 2016; Malandraki et al. 2019), and they suggested that the kinetic transport theories of Zank et al. (2014) and le Roux et al. (2015) could explain their findings. The necessity for these theories arises because fully kinetic simulations lack the ability to operate on the large scales needed to explain spacecraft observations.

The abovementioned kinetic transport theories describe how distributions of suprathermal particles in the solar wind are accelerated by a region of dynamic small-scale magnetic flux ropes (SMFRs). SMFRs may be defined as quasi-helical coherent nonlinear magnetic field structures that are advected with the solar wind flow (Zank et al. 2017). They consist of a twist ("island") component that exists in a 2D plane perpendicular to an axial ("guide") field (Cartwright & Moldwin 2010). These structures can be thought of as a manifestation of the perpendicular

wavenumber component of magnetohydrodynamic (MHD) shear Alfvén waves that have a zero phase speed (Zank et al. 2017), and are classified as part of a quasi-2D turbulence component that naturally forms perpendicular to a significant guide field (Zank et al. 2017). Two-dimensional MHD turbulence is considered by some to be the dominant MHD turbulence component in the large-scale inner heliospheric solar wind at lower helio latitudes (Matthaeus et al. 1990; Zank & Matthaeus 1992, 1993; Bieber et al. 1996; Hunana & Zank 2010; Zank et al. 2017). There is evidence that SMFRs form more densely near large-scale, turbulently reconnecting current sheets such as the Heliospheric Current Sheet and current sheets associated with Interplanetary Coronal Mass Ejections and Corotating Interaction Regions (Cartwright & Moldwin 2010; Khabarova et al. 2015, 2016; Khabarova & Zank 2017; Hu et al. 2018). A key aspect of SMFRs is that they are dynamic; they can merge (Khabarova et al. 2015, 2016; Chian et al. 2016; Zheng et al. 2017), contract, and expand. The dynamics of SMFRs generate electric fields that lead to particle acceleration. Building on the results from kinetic simulations (Drake et al. 2006, 2013; Li et al. 2015), Zank et al. (2014) and le Roux et al. (2015) developed comprehensive focused transport equations to describe the impact of a field of SMFRs on a distribution of energetic particles.

In these focused transport equations, there are four basic SMFR acceleration mechanisms that particles exploit for energy change: SMFR compression acceleration, SMFR parallel shear flow acceleration in the incompressible limit, acceleration by the component of the turbulent motional electric field force generated in merging SMFRs parallel to the guide/background magnetic field, and acceleration by the parallel component of the non-inertial force associated with the acceleration of the SMFR flow (le Roux et al. 2018). le Roux et al. (2015) showed how the systematic and stochastic acceleration rates due to these mechanisms yield first- and second-order Fermi acceleration rates. *It is not yet known which of these mechanisms dominates in the acceleration processes in the large-scale solar wind.*

Zank et al. (2014) and le Roux et al. (2015) derived Parker–Gleeson–Axford type (henceforth Parker) transport equations from their focused transport equations, to facilitate analytical studies. Even though this limited the applications of the theory to energetic particles with nearly isotropic distributions due to pitch-angle observed SMFR acceleration, observations were still well-reproduced. For example, Zhao et al. (2018) accurately modeled the flux enhancements and spectral characteristics of energetic particles in an SMFR region at 5 au by using mostly first-order Fermi SMFR compression acceleration in the 1D steady-state analytical solution of the Parker transport equation in planar geometry (see Figure 3 from that publication). le Roux et al. (2019) made further progress by presenting an analytical solution that, for the first time, unified all the SMFR acceleration mechanisms in their Parker transport equation. They showed that both first- and second-order Fermi mechanisms can reproduce enhanced energetic particle fluxes in SMFR regions at 1 au reported in Khabarova & Zank (2017). Both studies needed to introduce a simple escape term to steepen analytical spectral slopes of particles accelerated by SMFRs to be in agreement with observed spectral slopes. However, le Roux et al. (2019) discovered an increased hardening of the accelerated spectra deeper into the SMFR acceleration region that is significantly stronger for first-order Fermi SMFR acceleration. This highlights a key difference between systematic (first-order Fermi) and stochastic (second-order Fermi) acceleration that can potentially serve as a method for identifying the dominant SMFR acceleration mechanism in observations. *Identification of the dominant SMFR acceleration mechanism in the large-scale solar wind remains an unsolved problem that this paper intends to shed more light on.*

In this paper, the analytical solution of le Roux et al. (2019) in planar geometry is extended to a heliocentric spherical geometry in order to study the additional effects of solar wind expansion and the radial variation of transport mechanisms on the SMFR-accelerated particles. Solutions are presented for the case where all SMFR acceleration mechanisms are included, and then for individual SMFR acceleration mechanisms acting alone. A search was launched to find observational evidence of SMFR acceleration events within 1 au behind interplanetary shocks. We present two new SMFR acceleration events identified within 1 au for the first time. The solution including all SMFR acceleration mechanisms is fit to the two new events via a Metropolis–Hastings algorithm (Zhao et al. 2019), which is a Markov Chain Monte Carlo technique, giving an estimate for the transport parameters associated with each SMFR acceleration mechanism. The transport parameters associated with each SMFR acceleration mechanism are then scrutinized to determine their relative physical significance so that a dominant mechanism may be identified. On this basis, we present evidence below that second-order Fermi SMFR acceleration dominated first-order Fermi SMFR acceleration in these two events. Furthermore, Grad–Shafranov reconstructions of SMFRs occurring during these events were performed. As reported below, the evidence suggests that second-order Fermi SMFR acceleration is dominated by the SMFR mechanism associated with the parallel component of the turbulent motional electric field force. In addition, efficient particle escape from the SMFR acceleration region is necessary to reproduce observed spectral slopes and spatial profiles.

2. Analytical Approach

We recently extended our Parker-type transport equation for energetic particle interaction with numerous dynamic SMFRs (le Roux et al. 2015, 2016, 2018, 2019) to include perpendicular diffusion in addition to parallel diffusion (more detail will be presented in a future publication). In a somewhat simplified form, this equation reads

$$\frac{\partial f}{\partial t}+\left[\boldsymbol{u}_0-\frac{1}{3p^2}\frac{\partial}{\partial p}(p^3u_I^E\boldsymbol{b}_0)\right]\cdot\nabla f-[\nabla\cdot(\boldsymbol{u}_0^I+u_I^E\boldsymbol{b}_0)]\frac{p}{3}\frac{\partial f}{\partial p}$$
$$=\nabla\cdot(\kappa_I\cdot\nabla f)+\frac{1}{p^2}\frac{\partial}{\partial p}\left(p^2D_{pp}^I\frac{\partial f}{\partial p}\right)+\frac{2}{3}pu_I^E(\boldsymbol{b}_0\cdot\nabla)\frac{\partial f}{\partial p}-\frac{f}{\tau_{\rm esc}}+Q, \quad (1)$$

where $f(\boldsymbol{x}, p, t)$ is the direction-averaged energetic particle distribution function that depends on the particle position $\boldsymbol{x}$, momentum p, and time t. In Equation (1), $\boldsymbol{u}_0$ is the solar wind flow velocity, $u_E^I\boldsymbol{b}_0$ is the advection velocity along the background magnetic field with unit vector $\boldsymbol{b}_0$ induced by the particle interaction with the mean turbulent motional electric field in the SMFRs parallel to $\boldsymbol{b}_0$, $\nabla\cdot\boldsymbol{u}_0^I$ refers to the combined divergence of the solar wind flow velocity and the mean divergence of the SMFR flow velocity, κ_I is the energetic particle diffusion tensor, D_{pp}^I is the momentum diffusion coefficient for energetic particles undergoing second-order Fermi acceleration during interaction with SMFRs, $\tau_{\rm esc}$ is the timescale on which particles escape from the SMFR acceleration region, and Q is the particle source for injection into the SMFR acceleration region. Equation (1) models advection of energetic particles by the large-

scale solar wind flow and mean turbulent motional electric field in SMFRs (second term), adiabatic energy changes of energetic particles induced by the divergence of the solar wind flow and mean turbulent motional electric field in SMFRs (third term), energetic particle diffusion along and across the mean magnetic field due to scattering by SMFRs (fourth term), stochastic or second-order Fermi acceleration of energetic particles in response to SMFRs (fifth term), coherent transport along the average magnetic field and in p-space in response to the mean turbulent motional electric field (sixth term), particle escape from the SMFR acceleration region (penultimate term), and injection of particles into the SMFR acceleration region (last term).

In order to facilitate an analytical solution, we express Equation (1) in a heliocentric spherical coordinate system, imposing spherical symmetry. We assume spherical instead of Cartesian geometry (le Roux et al. 2019), thus allowing us to impart a more realistic radial dependence to the transport coefficients—instead of constant coefficients, as is the case for previous analytical solutions in Cartesian geometry—and model the effect of spherical solar wind expansion on energetic particle transport (Zhao et al. 2018; Adhikari et al. 2019; le Roux et al. 2019). Then Equation (1) becomes

$$\frac{\partial f}{\partial t} + [u_0 - u_I^E \cos(\psi)]\frac{\partial f}{\partial r} - \frac{1}{r^2}\frac{\partial}{\partial r}[r^2(u_0^I + u_I^E \cos(\psi))]\frac{p}{3}\frac{\partial f}{\partial p} = \frac{1}{r^2}\frac{\partial}{\partial r}\left(r^2\kappa_{rr}^I\frac{\partial f}{\partial r}\right) + \frac{1}{p^2}\frac{\partial}{\partial p}\left(p^2 D_{pp}^I\frac{\partial f}{\partial p}\right) + \frac{2}{3}u_I^E\cos(\psi)\frac{\partial}{\partial p}\left(p\frac{\partial f}{\partial r}\right) - \frac{f}{\tau_{\rm esc}} + Q, \quad (2)$$

where we assumed that both κ_{rr}^I and u_E^I are independent of p for simplicity. In Equation (2), we assumed a solar wind flowing out radially from the Sun according to $\boldsymbol{u}_0 = u_0\boldsymbol{e}_r$, where the solar wind speed u_0 is constant. The advection velocity $u_I^E\boldsymbol{b}_0$ is projected in the heliocentric radial direction according to $u_I^E(\boldsymbol{b}_0\cdot\boldsymbol{e}_r) = u_I^E\cos(\psi)$, where ψ is the average angle between the radial direction and the assumed spiral interplanetary magnetic field. In the adiabatic energy change term, we model

$$\begin{aligned} &-\frac{1}{r^2}\frac{\partial}{\partial r}[r^2(u_0^I + u_I^E\cos(\psi))] \\ &= -(2u_0 - r_0\langle\nu_{\rm COM}^I\rangle(r_0) + u_I^E(r_0)\cos(\psi(r_0)))\frac{1}{r} \\ &= -(2u_0 - \overline{\langle\nu_{\rm COM}^I\rangle} + u_{Er})\frac{1}{r}, \end{aligned} \quad (3)$$

where term 1 indicates adiabatic cooling of energetic particles in the radially expanding solar wind outflow, and term 2 represents adiabatic heating or first-order Fermi acceleration of energetic particles due to the mean SMFR compression rate defined as $\langle\nu_{\rm COM}^I\rangle = -\langle\nabla\cdot\delta\boldsymbol{U}_I\rangle$, where $\delta\boldsymbol{U}_I$ is the plasma flow velocity inside SMFRs. The last term models adiabatic cooling ($u_{Er} > 0$) or adiabatic heating ($u_{Er} < 0$) due to radial expansion or compression of u_{Er}. The radial diffusion coefficient κ_{rr}^I is determined from the projection of the parallel diffusion coefficient $\kappa_\parallel^I$ and perpendicular diffusion coefficient $\kappa_\perp^I$ in the heliocentric radial direction according to the expression

$$\kappa_{rr}^I = [\kappa_\parallel(r_0)\cos^2(\psi(r_0)) + \kappa_\perp(r_0)\sin^2(\psi(r_0))]\frac{r}{r_0} = \kappa r,$$

assuming that $\kappa_\parallel^I \propto r$. Furthermore,

$$D_{pp}^I = D_{pp}^I(r_0)\frac{r_0}{r} = p^2\frac{D_0}{r},$$

based on the assumption that $D_{pp}^I \propto 1/r$. We also model $\tau_{\rm esc} \propto 1/r$ according to $1/\tau_{\rm esc} = r_0/(r\tau_{\rm esc}(r_0)) = v_{\rm esc}/r$. Note that we specified u_0, $\overline{\langle\nu_{\rm COM}^I\rangle}$, u_{Er}, K, and D_0 are independent of r and p and have units of speed. Finally, we inject a source of energetic particles with momentum p_0 at a position r_0 into the SMFR acceleration region specified to be

$$Q = \frac{dN/dt}{16\pi^2 r_0^2 p_0^2}\delta(r - r_0)\delta(p - p_0),$$

where dN/dt is a constant rate at which particles are injected into the SMFR acceleration region. While, in reality, one would expect a full momentum spectrum from the background pool of suprathermal particles in the solar wind to be injected into the SMFR acceleration region with a minimum momentum of about $p = m_p u_0$, we believe injecting a monoenergetic source can be approximately justified by choosing $p_0 = m_p u_0$, where most particles in the suprathermal source spectrum can be found.

To set Equation (2) up for an analytical solution, we apply the above assumptions and introduce a new variable $z = \ln(p/p_0) > 0$, which results in

$$\frac{\partial^2 f}{\partial r^2} - \left[\frac{u_0 - u_{Er} - 3\kappa}{\kappa}\right]\frac{1}{r}\frac{\partial f}{\partial r} - \left[\frac{2/3(-u_0 - u_{Er} + \overline{\langle\nu_{\rm COM}^I\rangle}/2) - 3D_0}{\kappa}\right]\frac{1}{r^2}\frac{\partial f}{\partial z} + \frac{D_0}{\kappa r^2}\frac{\partial^2 f}{\partial z^2} + \frac{2u_{Er}}{3\kappa r}\frac{\partial^2 f}{\partial r\partial z} - \frac{f v_{\rm esc}}{\kappa r^2} = -\frac{dN/dt}{16\pi^2\kappa r_0^3 p_0^3}\delta(r - r_0)\delta(z). \quad (4)$$

Under these assumptions, the solution to Equation (4) is

$$f(r,p) = \frac{dN/dt}{32\pi^3\kappa r_0^2 p_0^3\sqrt{A^*}}\left(\frac{r}{r_0}\right)^{\tilde{a}-\tilde{a}B/2A}\left(\frac{p}{p_0}\right)^{-B/2A} \times K_0\left[b\sqrt{(\ln(r/r_0))^2 + \frac{1}{A^*}(\ln(p/p_0) + \tilde{a}\ln(r/r_0))^2}\right], \quad (5)$$

where K_0 is a modified Bessel function of the second kind and

$$A^* = \frac{D_0}{\kappa}\left(1 - \frac{u_{Er}^2}{9\kappa D_0}\right),$$

$$b = \sqrt{\left(1 - \frac{(u_0 - u_{Er})}{2\kappa}\right)^2 + \frac{v_{\rm esc}}{\kappa} + \frac{D_0}{4\kappa}\frac{(3 - (1/3D_0)[\overline{\langle \nu_{\rm COM}^I \rangle} - u_{Er}u_0/\kappa + u_{Er}^2/\kappa - 2u_0])^2}{(1 - u_{Er}^2/9\kappa D_0)}},$$

$$\frac{B}{2A} = \frac{1}{2}\frac{(3 - (1/3D_0)[\overline{\langle \nu_{\rm COM}^I \rangle} - u_{Er}u_0/\kappa + u_{Er}^2/\kappa - 2u_0])}{(1 - u_{Er}^2/9\kappa D_0)},$$

$$\overline{a} = -\left(1 - \frac{u_0 - u_{Er}}{2\kappa}\right),$$

$$\tilde{a} = -\frac{u_{Er}}{3\kappa}.$$

See Appendix A for details. This solution in spherical geometry is an improvement on the one presented in le Roux et al. (2015) because it includes all the transport effects of the parallel turbulent motional electric field parallel to the guide field (advection, adiabatic energy changes, acceleration effects from the mixed-derivative transport term, and second-order Fermi acceleration) while the earlier spherical solution only included the contribution from second-order Fermi acceleration. In order to avoid the solution becoming complex, which would be nonphysical, we require $A^* > 0$ so that $1 - (u_{Er}^2/9\kappa D_0) > 0$. Interestingly, this mirrors the requirement given in le Roux et al. (2019; see discussion after Equation (21)) that arose from the need to retain causality in their solution, otherwise particles would travel further than their speed would allow. le Roux et al. (2019) also found that imposing causality suggests that the acceleration by the turbulent motional electric field parallel to the guide/background magnetic field must be such that the contribution from second-order Fermi acceleration must dominate the contribution from the mixed-derivative transport term (third to last term in Equations (1) and (2)). This idea is supported by the data fits presented below (see Section 4), where acceleration by the mean turbulent motional electric field parallel to the guide field is suppressed even further than in the above limit.

2.1. High-energy Limit

In the high-energy limit $p/p_0 \gg 1$ for $r > r_0$, the full solution (5) simplifies to

$$f(r, p) = \frac{dN/dt}{32\pi^3\kappa r_0^2 p_0^3}\sqrt{\frac{\pi}{2}}\,(b\sqrt{A^*}\ln(p/p_0))^{-1/2}\left(\frac{r}{r_0}\right)^{\overline{a} - \tilde{a}B/2A}\left(\frac{p}{p_0}\right)^{-B/2A - b/\sqrt{A^*}}, \quad (6)$$

after taking the large-argument limit of the modified Bessel function. See Appendix B for details. Because in this limit the p/p_0-term dominates in the Bessel function, the limit behaves as the solution would near the source (i.e., $r = r_0$). Rearranging the exponent of the r/r_0-term in the limit shows

$$\overline{a} - \tilde{a}\frac{B}{2A} = -1 + \frac{-\overline{\langle \nu_{\rm COM}^I \rangle} + 2u_0}{2u_{Er}}\left[\frac{1}{1 - u_{Er}^2/9\kappa D_0} - 1\right] + \frac{u_0}{2\kappa}\left[\frac{1}{1 - u_{Er}^2/9\kappa D_0}\right].$$

Again, see Appendix B for details. If the requirement $9D_0\kappa > u_{Er}^2$ is satisfied as we assume, then it is easy to see that, if $\overline{\langle \nu_{\rm COM}^I \rangle}/2 > u_0 > 2\kappa$, the exponent of the r/r_0-term is positive, as is required for spatial peaks to form in the solution. The latter inequality needs to be imposed because we assumed $u_{Er} < 0$, as was done in previous studies (Zank et al. 2014, 2015; le Roux et al. 2016, 2018, 2019). It is important to note that the exponent is only positive (i.e., there is an increase in the particle distribution function with increasing radial distance) for $u_0 > 0$ when particle advection by the radially outward solar wind flow and radial particle diffusion both occur in the radially outward direction beyond the injection position ($r > r_0$) as was discussed in le Roux et al. (2018, 2019). The large radial distance limit (see Section 2.2 below; i.e., $r \gg r_0$ and $p > p_0$) will show a decrease in the distribution function as the radial position increases. Combining that with the results from this section means that peaks naturally form in the solution upstream of the injection point ($r > r_0$), indicating that particles are "injected" into the SMFR field closer to the Sun than where the peaks in the distribution function are occurring. It appears that, in previous modeling efforts, it was assumed that peaks in the particle spatial profiles formed closer to the Sun than the injection position, which implies that the observer is in a moving frame in which the solar wind flow appears to go sunward (Zhao et al. 2018; Adhikari et al. 2019) in order to ensure that particle advection by the solar wind and particle diffusion is in the same direction. Because we chose a heliocentric spherical geometry and we operate in the observer frame (i.e., the spacecraft frame), we view the events in the opposite manner, i.e., particles are injected closer to the Sun and peaks in the spatial profiles form further away from the Sun.

2.2. Large Radial Distance Limit

In this limit, where $r \gg r_0$ and $p > p_0$, we find that the full solution (5) simplifies to

$$f(r,p) = \frac{dN/dt}{32\pi^3\kappa r_0^2 p_0^3}\sqrt{\frac{\pi}{2}}\left(b\sqrt{D_0 A^*/\kappa}\,\ln(r/r_0)\right)^{-1/2}\left(\frac{r}{r_0}\right)^{\bar{a}-\bar{a}B/2A-b\sqrt{D_0/\kappa A^*}}\left(\frac{p}{p_0}\right)^{-B/2A}, \quad (7)$$

and if the condition

$$\frac{v_{\rm esc}}{\kappa} - 2\left(1 - \frac{(u_0 - u_{Er})}{2\kappa}\right)\sqrt{\frac{D_0}{4\kappa}}\frac{\kappa q}{D_0 A^*} > 0$$

is met (where $q = (3 - (1/3D_0)[\overline{\langle \nu^I_{\rm COM}\rangle} - u_{Er}u_0/\kappa + u_{Er}^2/\kappa - 2u_0])$), the exponent of r/r_0 will be negative overall. See Appendix C for details. In Section 4, we will show that the data fits suggest that $v_{\rm esc}$ (which accounts for particle escape from the SMFR region) is the dominant parameter in this inequality, thus resulting in its fulfillment. Therefore, when $r/r_0 \gg 1$, the distribution function decays with increasing radial distance. Assuming that the distribution function is continuous and thus a differentiable function from $r \approx r_0$ to $r \gg r_0$ implies that, since the high-energy limit at $r \approx r_0$ yielded an increasing distribution function and the large radial distance limit a decreasing distribution function with increasing radial distance, there must be a peak in the distribution function in between.

2.3. Individual SMFR Acceleration Mechanism Limits

2.3.1. Second-order Fermi Acceleration

To reach the limit in the complete solution where second-order Fermi acceleration by SMFRs is the dominant SMFR acceleration mechanism, we let $u_{Er} \to 0$ and $\overline{\langle \nu^I_{\rm COM}\rangle} \to 0$. This gives the result

$$f(r,p) = \frac{dN/dt}{32\pi^3 r_0^2 p_0^3\sqrt{\kappa D_0}}\left(\frac{r}{r_0}\right)^{-(1-u_0/2\kappa)}\left(\frac{p}{p_0}\right)^{-3/2(1+2u_0/9D_0)} K_0[b^*\sqrt{(\ln(r/r_0))^2 + \kappa z^2/D_0}], \quad (8)$$

where

$$b^* = \sqrt{1 + \left(\frac{u_0}{2\kappa}\right)^2 + \frac{v_{\rm esc}}{\kappa} + \frac{9D_0}{4\kappa} + \frac{u_0^2}{9D_0\kappa}}.$$

See Appendix D for details. By comparing this solution to the solution for second-order Fermi acceleration in the case of planar geometry (see Equation (28) in le Roux et al. 2019), we see that our solution includes additional effects related to spherical geometry. For example, the factor $u_0/2\kappa$ in the argument of the exponential that contains $x - x_0$ in le Roux et al. (2019) becomes the exponent of r/r_0 with the addition of a geometric factor ($u_0/2\kappa \to -(1 - u_0/2\kappa)$), and the exponent of (p/p_0) gets modified by the term $-u_0/3D_0$ ($-3/2 \to -3/2(1 + 2u_0/9D_0)$). The former indicates that, for a peak in the particle distribution to form upstream of the injection point, the $(r/r_0)^{-1}$ factor must be overcome, while the latter implies a competition between adiabatic cooling by the radially expanding solar wind that steepens the accelerated particle spectrum and second-order Fermi acceleration by SMFRs that has a hardening effect on the spectrum.

If we choose $D_0 \gg u_0; \kappa; v_{\rm esc}$ to determine the hardest possible accelerated spectrum due to second-order Fermi acceleration, which occurs upstream of the injection point $r > r_0$, we get

$$f(r,p) = \frac{dN/dt}{32\pi^3 r_0^2 p_0^3\sqrt{D_0}}\sqrt{\frac{\pi}{3\sqrt{D_0\kappa}\ln(r/r_0)}}\left(\frac{r}{r_0}\right)^{-(1-u_0/2\kappa)-3/2\sqrt{D_0/\kappa}}\left(\frac{p}{p_0}\right)^{-3/2}. \quad (9)$$

Because adiabatic cooling becomes negligible in the limit of strong second-order Fermi acceleration, the hardest possible spectrum has the same power-law index as in the case of planar geometry, namely, $-3/2$ (see Equation (28) in le Roux et al. 2019). The hardest possible spectrum at the injection position $r = r_0$ for high-energy particles is obtained when we take the limit $r \to r_0$ and apply the large-argument limit to the modified Bessel function that results in

$$f(r,p) = \frac{dN/dt}{32\pi^3 r_0^2 p_0^3\sqrt{D_0\kappa}}\sqrt{\frac{\pi}{3\ln(p/p_0)}}\left(\frac{p}{p_0}\right)^{-3}. \quad (10)$$

Thus, the hardest possible accelerated spectrum for second-order Fermi acceleration in the test-particle limit at high energies has a power-law index that varies between -3 at the injection position to $-3/2$ beyond the injection position ($r > r_0$) inside the SMFR region, indicating spectral hardening beyond the injection position as monoenergetic source particles are accelerated to increasingly high energies in a diffusive manner.

2.3.2. Acceleration by the Mean Turbulent Motional Electric Field Parallel to the Guide/Background Magnetic Field

This limit follows by letting $D_0 \to 0$, $\overline{\langle \nu^I_{\rm COM}\rangle} \to 0$ and allowing $-u_{Er} = u^*_{Er} \gg 1$ to dominate. Then,

$$f(r,p)=\frac{3dN/dt}{32\pi^2 u_{Er}^* r_0^2 p_0^3}\left(\frac{r}{r_0}\right)^{-(1-u_0/u_{Er}^*)}\left(\frac{p}{p_0}\right)^{3K/u_{Er}^*(u_0/u_{Er}^*-(u_0+u_{Er}^*)/2\kappa)}$$
$$\times I_0\left[\nu^*\left(\frac{3\kappa}{u_{Er}^*}\right)\sqrt{z}\sqrt{z+\frac{2u_{Er}^*}{3\kappa}\ln(r/r_0)}\right]\left[[1-H(r-r_0)]H\left(\frac{3\kappa}{u_{Er}^*}z+2\ln(r/r_0)\right)+H(r-r_0)\right], \quad (11)$$

where I_0 is the modified Bessel function of the first kind and

$$\nu^*=\sqrt{-\left(1-\frac{u_0}{u_{Er}^*}\right)\left(1+\frac{u_0}{u_{Er}^*}-\frac{u_0+u_{Er}^*}{\kappa}\right)-\frac{v_{\rm esc}}{\kappa}}.$$

See Appendix E for details. Note that this solution limit models acceleration effects from the average turbulent motional electric field parallel to the guide/background field through both the mixed-derivative transport term and the term that includes the large-scale divergence of $u_{Er}^\star$ (see Equations (2) and (3)). We use the latter term to model adiabatic heating ($u_{Er}^\star > 0$) of energetic particles and how it weakens with increasing radial distance from the Sun. This solution improves on the one presented in le Roux et al. (2019; see Equation (30)) because it utilizes the modified Bessel function of the first kind (I_0) rather than an ordinary Bessel function of the first kind (J_0), which oscillates between positive and negative numbers. Thus, unphysical negative values for the distribution function are avoided when the argument of J_0 grows too large with increasing momentum values and distance relative to the injection position as a consequence of the presence of the escape term. In the new solution, the modified Bessel function ensures that such oscillations in the distribution function do not occur. This improvement came about because, in spherical geometry, the divergence of u_{Er} contributes to particle energy changes, whereas in previous solutions in Cartesian geometry, this effect is absent. Another consequence of the divergence of the u_{Er} is that the distribution function forms a smooth peak beyond the injection position, similarly to the other SMFR acceleration mechanisms, instead of a plateau as predicted by the original solution of Zank et al. (2014) without escape effects. If we take $u_{Er}^* \gg u_0$, we recover the same accelerated spectrum limit at the source as Zank et al. (2014) and le Roux et al. (2019), i.e., $f(r_0,\ p)\propto p^{-3/2}$. Similarly, if we take $u_{Er}^* \gg u_0$ and $u_{Er}^* \gg v_{\rm esc}$, we can recover the result from Zank et al. (2014) where the spatial profile resembles a plateau.

2.3.3. First-order Fermi (Compression) Acceleration

When $u_{Er}\to 0$ and $D_0\to 0$, the full solution yields the limit of mean SMFR compression acceleration given by

$$f(r,p)=\frac{dN/dt}{32\pi^3 r_0^2 p_0^3}\sqrt{\frac{3\pi}{\kappa(\overline{\langle\nu_{\rm COM}^I\rangle}-2u_0)\ln(p/p_0)}}\left(\frac{p}{p_0}\right)^{-3\kappa\frac{(1-u_0/2K)^2+v_{\rm esc}/\kappa}{\overline{\langle\nu_{\rm COM}^I\rangle}-2u_0}}\left(\frac{r}{r_0}\right)^{-(1-u_0/2\kappa)}$$
$$\times\exp\left[-\frac{1}{4}(\ln(r/r_0))^2\frac{\overline{\langle\nu_{\rm COM}^I\rangle}-2u_0}{3\kappa\ln(p/p_0)}\right]. \quad (12)$$

See Appendix F for details. This solution mirrors that given in le Roux et al. (2019; see Equation (27)), with the exception that the factor $u_0/2\kappa$ in the argument of the exponential that contains $x-x_0$ in le Roux et al. (2019) becomes the exponent of $r=r_0$ here with the addition of a geometric factor ($u_0/2\kappa\to-(1-u_0/2\kappa)$). As in le Roux et al. (2019), when the compression rate increases (larger values of $\overline{\langle\nu_{\rm COM}^I\rangle}$), the acceleration due to the SMFRs becomes more efficient across all energies. When $\overline{\langle\nu_{\rm COM}^I\rangle}/u_0 \gg 1$, the acceleration spectrum approaches $f(r,p)\propto p^0$. As will be shown in the data fits later, $u_0>\kappa$ in the two events examined in this study. Thus, the exponent of r/r_0 will be positive while the exponential including $(\ln(r/r_0))^2$ will be negative if $\overline{\langle\nu_{\rm COM}^I\rangle}>u_0$, disposing the solution to form peaks upstream of the injection point $r=r_0$. Again, like le Roux et al. (2019), we find that the downstream spectrum cuts off at the injection momentum because first-order Fermi acceleration systematically energizes the source particles with $p=p_0$.

3. SMFR Acceleration Events Observed within 1 au

This study considered SMFR acceleration events observed by the Helios A spacecraft within 1 au. Previous modeling attempts have been limited to SMFR acceleration events observed at 1 au and beyond. Events were identified by examining energetic particle counts behind interplanetary shocks observed by Helios A's Experiment 8 (E8), the Low-Energy Electron and Ion Spectrometer (Porsche 1975). We decided to use data from the E8 detector because of its suitability for investigating the nonrelativistic suprathermal particle populations described by our transport theory. We chose to search behind interplanetary shocks because of the potential for particles being accelerated by these SMFRs to serve as an injection source for DSA. Fast forward shocks were chosen from the ipshock.fi[4] database. SMFR acceleration events were identified when enhancements in the energetic particle flux were found to coincide with the occurrence of SMFRs in Helios data identified by Chen & Hu (2020) using Grad–Shafranov reconstruction methods. In support of this approach, we note that previous analyses of low-frequency turbulence properties during potential SMFR acceleration events confirmed that the turbulence is dominated by SMFRs rather than Alfvén waves (Malandraki et al. 2019;

[4] http://www.ipshocks.fi/

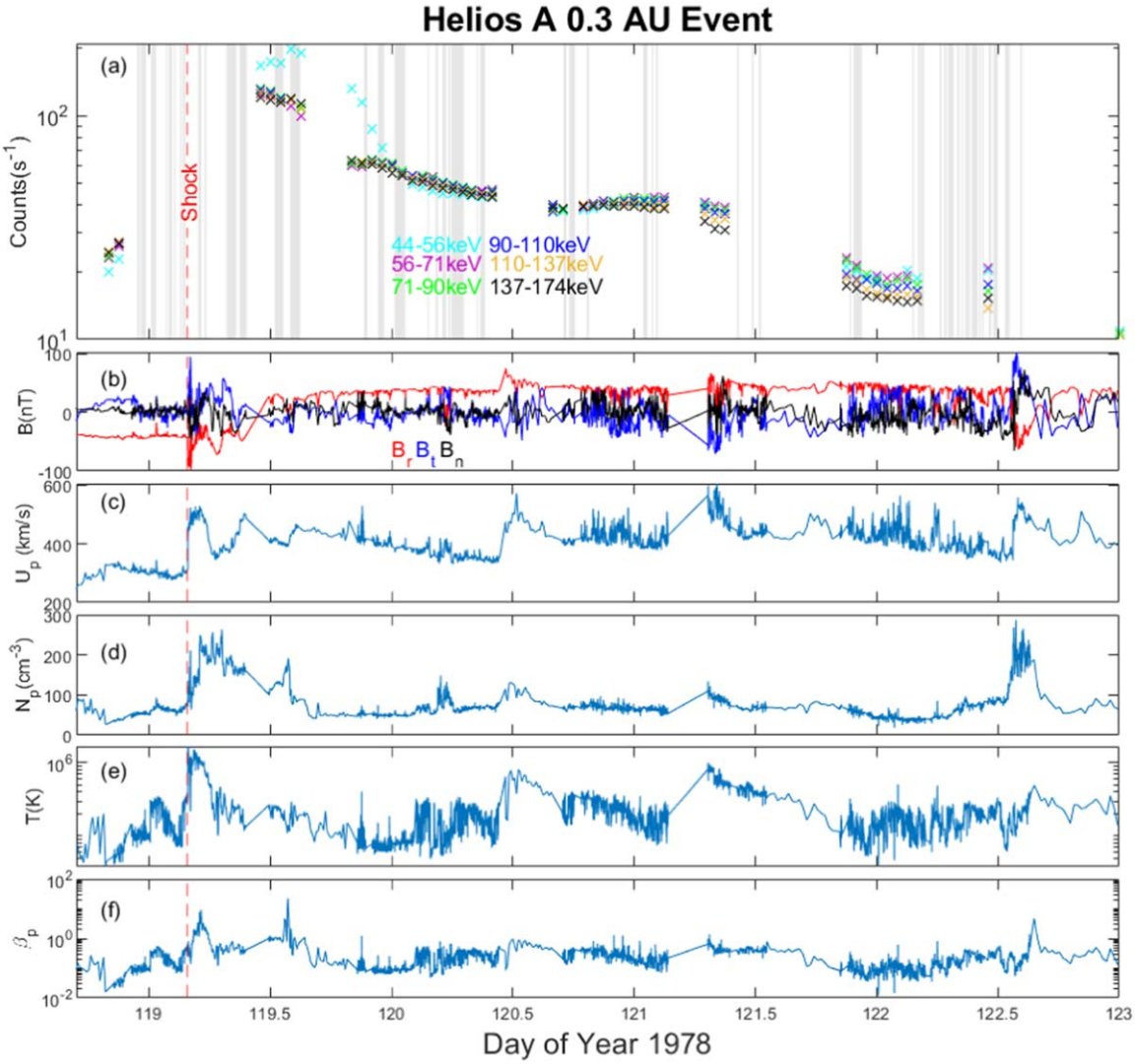

Figure 1. (a) The particle counts from 44 to 174 keV registered by the E8 detector on Helios A. The interplanetary shock that passed by Helios A on 29 April 1978 at 03:49:33 UT is denoted by the dashed red line. The gray bars represent the time and duration of SMFRs identified by Chen & Hu (2020). (b) The magnetic field presented in the RTN coordinate system, (c) the proton flow speed as measured in the spacecraft frame, (d) the proton number density, (e) the proton temperature, (f) and the plasma beta presented as time series.

Zhao et al. 2019) because of the strong negative residual energy, small cross helicity, and large uniform magnetic helicity, for example. While difficulties arose due to gaps in the Helios A data, two events with profiles fitting the theoretical predictions were found.

3.1. SMFR Acceleration Event of 29 April 1978

The first event occurred behind an interplanetary shock which passed Helios A at 03:49:33 UT on 29 April 1978 (day 119.16) when the spacecraft was near its perihelion (∼0.3 au), which is closer to the Sun than any previously reported SMFR acceleration event. Figure 1(a) displays the particle counts for six different energy channels from 44 to 174 keV of the E8 detector. Although there is a significant data gap near the time of the interplanetary shock (denoted by the red dashed line labeled "Shock"), it is reasonable to conclude that the particle counts for each energy channel are peaking near the interplanetary shock, as is predicted by classical DSA theory. The particle count decreases with time behind the interplanetary shock during days 119–120.5 until a new peak occurs during the period from days 120.5–122. This peak cannot be easily be explained by classical DSA theory, because the associated particles are more than an effective diffusive length scale away from shock-accelerated particles at these energies (Zhao et al. 2018). Panel (b) displays the magnetic field in the RTN coordinate system gathered from the Helios A (E2) 40 s data. Panels (c)–(f) show the average proton flow speed, the proton density, the proton temperature, and the plasma beta, respectively. All the results presented in this figure are direct plots of Helios A (E1) 40 s data, except for the plasma beta values, which were calculated using the magnetic field, proton density, and proton temperature data.

Based on the combination of plasma and magnetic field data, we note an apparent interplanetary shock that occurs at around 14:00:00 UT on 2 May 1978 (day 122.6), which is not recorded in the ipshock.fi database. This omission could be caused by data gaps immediately following the time that the apparent interplanetary shock passes the spacecraft. Because of the significant gaps in the energetic particle data, we cannot conclusively state that particle counts peak at the interplanetary shock location, but the corresponding jumps in the magnetic

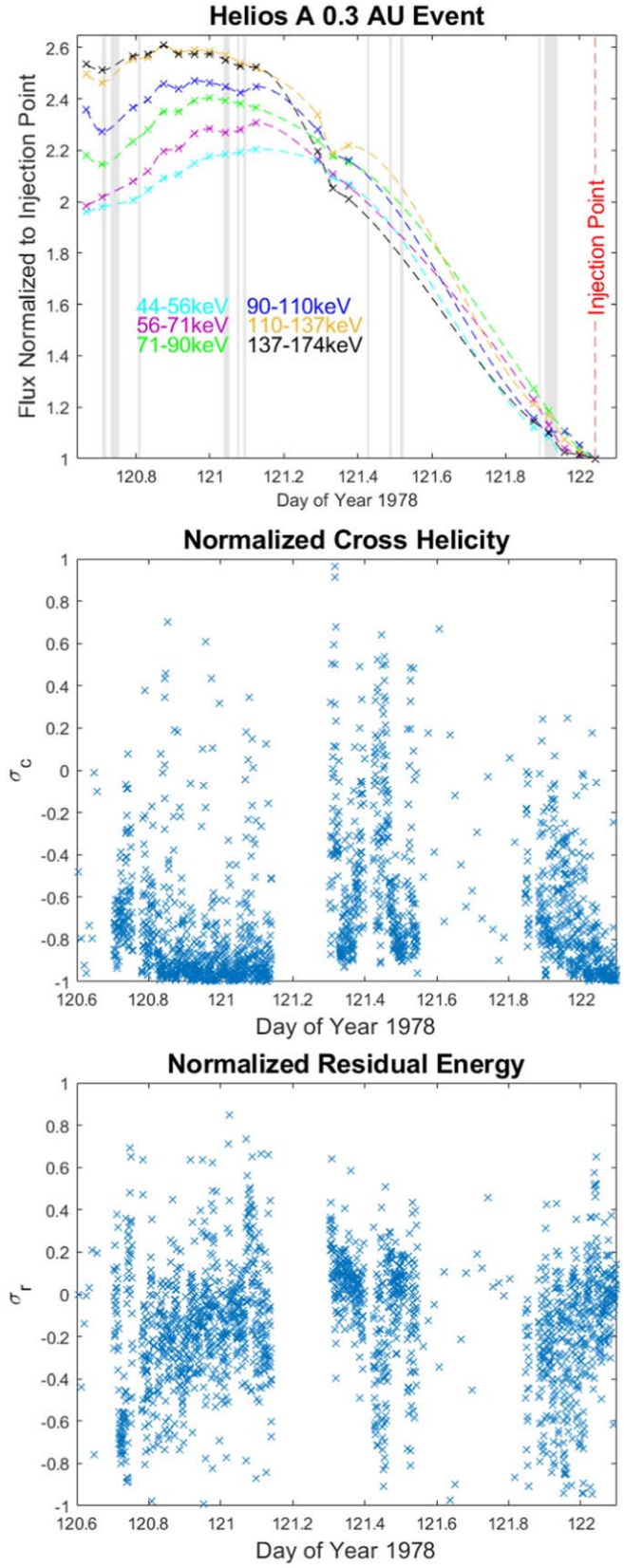

Figure 2. Top: The flux-enhancement profile we attribute to SMFR acceleration occurring downstream of the shock that passed by Helios A on 29 April 1978 at 03:49:33 UT (see Figure 1). The "x" symbols represent the measured flux normalized to the chosen injection point (dashed vertical line), and the dashed lines are a cubic interpolation of the measurements. Middle: The normalized cross helicity. Bottom: The normalized residual energy.

field, proton flow speed, proton density, and proton temperature (the proton temperature dips just before the corresponding jump, making it appear to decrease while the other quantities increase) around that time indicate that an interplanetary shock is present. We do not believe that this interplanetary shock contributes to the acceleration of particles in the region of interest (days 120.5–122) either, because the associated particles are clearly more than an effective diffusive length scale away from shock-accelerated particles at these energies (Zhao et al. 2018). Two periods where particle acceleration could be influenced by mechanisms not associated with SMFRs are days 120.5–120.75 and 121.25–121.5. Both periods are marked by noticeable increases in the proton flow speed and proton temperature, with less significant increases in the proton density. However, because significant portions of the data including energetic particle fluxes are missing, no conclusive interpretation of these two periods in terms of efficient particle acceleration by shocks or compression regions can be made. We admit that these periods could have some effect on the particle acceleration during the entire time interval we associate with SMFR acceleration, but in the absence of clear evidence to the contrary, we chose to model the entire time interval as if it were dominated by SMFR acceleration.

Focusing on the data that do not appear to follow classical DSA theory (days 120.6–122), we normalize the particle fluxes to a selected injection point (see Figure 2 top) in order to demonstrate that it follows the prediction of our SMFR transport theory. The gray bars represent the time and duration of SMFRs identified and reconstructed using the Grad–Shafranov method in Chen & Hu (2020). We also use the combined magnetometer (E1) and plasma data (E2) to search for evidence of Alfvén waves propagating in the region we attribute to SMFR acceleration (days 120.6–122), as they can also accelerate particles.

To identify regions where Alfvén waves are present, we calculate the normalized cross helicity and normalized residual energy using the method of Zank et al. (2011; see Equations (2)–(6) in the publication). Alfvén waves propagating solely in one direction are identifiable by a normalized cross helicity of ± 1 and a normalized residual energy that approaches zero. We note that the period between day 120.8–121.2 corresponds to the normalized cross helicity maintaining a value of ~ -1 and the normalized residual energy hovering around a value of zero (see Figure 2 middle and bottom). This lends credibility to the idea that Alfvén waves are propagating during this time period and are moving antiparallel to the magnetic field. Although Alfvén waves are expected to accelerate suprathermal particles in general, we note that standard quasi-linear theory predicts that the associated Parker-type transport for energetic particle interaction with parallel propagating Alfvén waves will only efficiently accelerate energetic particles (those with speed $v \gg v_{A0}$) stochastically if significant Alfvén wave propagation occurs in both directions, i.e., parallel and antiparallel to the magnetic field (e.g., see Equation (114) in le Roux & Webb 2007). On this basis, we rule out any significant acceleration contribution from Alfvén waves.

A selected few of the identified SMFRs for this SMFR acceleration event were fully reconstructed and displayed in Figure 3. SMFR parameters that are found in the theoretical expressions of the SMFR acceleration mechanisms were calculated for all identified SMFRs of this SMFR acceleration

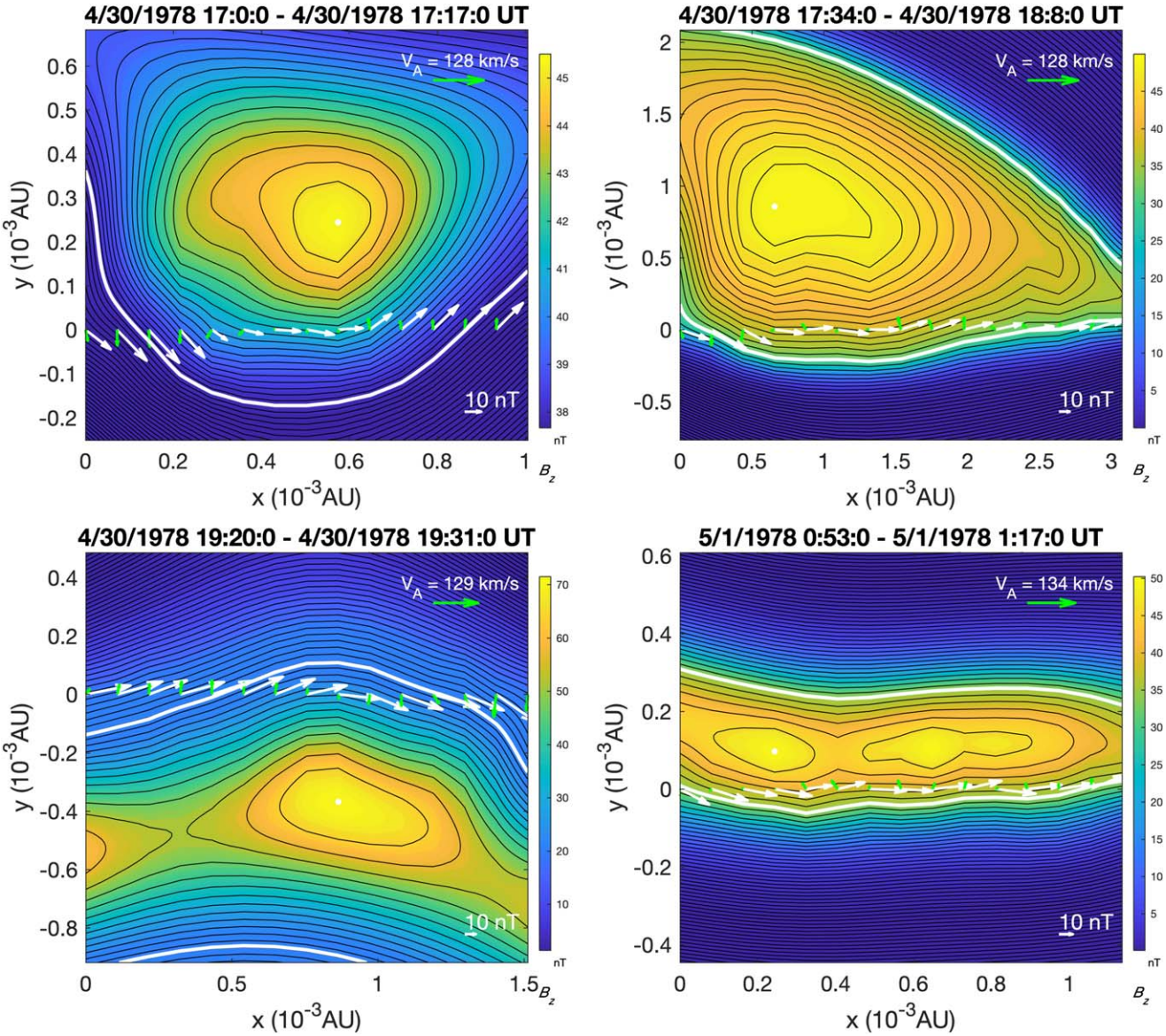

Figure 3. Grad–Shafranov reconstructions of some SMFRs from the 29 April 1978 event identified by Chen & Hu (2020). Displayed are the 2D SMFR twist or island field component (black contour lines) and the out-of-plane axial (guide) field component (colored regions). The white and green arrows indicate the magnetic field and flow vectors, respectively, along the spacecraft path.

event and presented in Table 1. The bottom two reconstructions in Figure 3 indicate that some identified SMFRs could be merging (note the presence of x points, which suggest the merging to be caused by magnetic reconnection at the adjacent boundaries between the SMFRs). This suggests that these SMFRs are dynamic and may be generating reconnection electric fields that can accelerate particles (Drake et al. 2013).

Compared to SMFRs identified in Zhao et al. (2018) near 5 au, those identified near 0.3 au are significantly smaller and have stronger magnetic fields, which is consistent with trends in SMFR radial evolution reported in Chen & Hu (2020), according to which SMFRs grow in size (Chen et al. 2019) and develop weaker magnetic field strengths with increasing radial distance from the Sun. These features can explain why the flux enhancement in Zhao et al. (2018) is much larger than the one for this event. Smaller SMFRs with stronger magnetic fields are more active and thus are better at accelerating particles than SMFRs that are larger with weaker magnetic fields (Xia & Zharkova 2020). As a thought experiment, consider two SMFR regions: one of them is not as effective at accelerating particles as the other, and both of them are observed by the same spacecraft over a specific energy range. We would observe a higher overall flux-enhancement in the region where the SMFRs are less effective at accelerating particles, because the more effective SMFR region would accelerate the particles out of the energy "field of view" more quickly and thus the spacecraft would observe fewer particles resulting in a smaller flux enhancement.

3.2. SMFR Acceleration Event of 1 May 1980

The second event with a flux-enhancement profile consistent with our theoretical prediction occurs between 30 April 1980 and 2 May 1980 (days 121–123 of 1980). It is not associated with any previously identified interplanetary shock in the ipshock.fi (see footnote 4) database; however, upon inspection

Table 1
SMFR Observations

Start Time (UT)	End Time (UT)	$\sqrt{\langle \delta u_l^2 \rangle}$ (m s^{-1})	σ_c^I (unitless)	B_0 (nT)	$\sqrt{\langle \delta B_l^2 \rangle}$ (nT)	$\langle N_p \rangle$ (#/cm^3)	$L_{l\perp}^c$ (au)
1978/4/30 17:00	1978/4/30 17:17	3.95E+04	9.34E-01	39.5523	19.33809988	57.63569722	0.001060619
1978/4/30 17:34	1978/4/30 18:08	7.14E+04	9.63E-01	32.6377	29.10176697	57.23493734	0.003150366
1978/4/30 19:20	1978/4/30 19:31	9.30E+04	9.80E-01	21.983	38.90315921	57.75457083	0.001644178
1978/5/1 0:53	1978/5/1 1:17	5.54E+04	9.39E-01	37.1447	26.09866139	55.635584	0.001178695
1978/5/1 1:46	1978/5/1 1:55	55367.87772	9.39E-01	19.3252	37.00618215	51.417725	0.001497344
1978/5/1 2:10	1978/5/1 2:22	37473.86266	9.22E-01	40.2876	17.19432374	51.854975	0.000339318
1978/5/1 10:11	1978/5/1 10:21	105020.499	9.52E-01	9.2575	49.33486637	57.97794091	0.001786635
1978/5/1 11:39	1978/5/1 11:49	102939.9453	9.82E-01	26.5092	41.61367016	59.63619545	0.001815884
1978/5/1 12:20	1978/5/1 12:34	114174.5581	0.9942341282	13.7565	43.27189812	59.79973	0.002495485
1978/5/1 21:20	1978/5/1 21:28	59845.87099	9.16E-01	45.8093	18.010629	53.47587778	0.001337191
1978/5/1 21:43	1978/5/1 22:33	117373.879	0.9727307059	15.3379	46.49261638	50.34004755	0.008727736
1979/1/13 13:29	1979/1/13 13:39	31582.795923	0.978581	4.706175	5.616962	10.78367182	0.000738081
1979/1/13 15:56	1979/1/13 16:50	9219.280624	−0.091884	7.357643	2.386892	7.504899822	0.009261096
1979/1/13 22:11	1979/1/13 22:23	23510.228186	0.946	6.529207	3.666973	5.644365	0.002444808
1979/1/13 22:43	1979/1/13 23:06	17436.000791	0.906223	7.23788	2.809392	5.5472375	0.004317586
1979/1/14 0:02	1979/1/14 0:15	10897.202845	0.748169	5.594426	2.345583	6.496817857	0.002711886
1979/1/14 0:38	1979/1/14 1:11	18415.440189	0.775234	4.479085	3.821926	6.729927304	0.002779401
1979/1/14 1:12	1979/1/14 1:43	11707.430776	0.882216	6.567754	2.104939	6.709254922	0.005706318
1979/1/14 1:45	1979/1/14 1:52	9635.574807	0.931597	6.073147	1.741567	8.462316111	0.001408441
1979/1/14 2:03	1979/1/14 2:28	12848.820911	0.905934	6.060181	2.376599	7.8356642	0.004592346
1979/1/14 3:42	1979/1/14 3:54	11335.039278	0.978192	7.111864	1.166138	6.386031667	0.002434228
1979/1/14 6:02	1979/1/14 6:09	29171.467761	0.615438	2.990586	7.212804	4.762549444	0.000685696
1979/1/14 6:51	1979/1/14 7:03	15999.90543	0.821127	7.859558	3.168786	5.109368929	0.001008443
1979/4/2 13:34	1979/4/2 13:43	6248.256118	0.056152	6.93043	2.324766	7.8424185	0.001162612
1979/4/2 15:20	1979/4/2 15:31	2817.628615	−0.128547	3.460604	4.236088	8.361669167	0.001461269
1979/4/2 17:28	1979/4/2 17:35	7227.949739	−0.037886	8.050103	2.475049	9.097792222	0.001142702
1979/4/2 18:29	1979/4/2 18:40	11062.798069	−0.789201	12.711667	2.754937	13.101735	0.001526583
1979/4/2 19:52	1979/4/2 20:01	22379.321896	−0.630645	3.383423	10.271583	14.9121575	0.000403295
1979/4/3 4:03	1979/4/3 4:16	33943.438629	−0.836949	4.709034	2.948144	9.881651429	0.001809008
1979/4/3 4:34	1979/4/3 4:48	149072.120907	−0.385908	10.360258	4.358445	10.12154156	0.001988163
1979/4/3 8:30	1979/4/3 8:53	5092.689167	0.231755	6.108708	2.701511	17.37970833	0.003167769
1979/4/3 9:56	1979/4/3 10:05	19038.407114	0.838505	0.748631	5.269143	17.373675	0.000892806
1979/4/3 10:59	1979/4/3 11:08	12179.154587	0.343778	5.526578	8.823641	9.277569545	0.001021766
1979/4/4 17:21	1979/4/4 17:35	15475.756622	0.733754	6.234427	4.090045	10.68308533	0.002320904
1979/4/4 17:46	1979/4/4 18:06	16328.525294	0.927246	6.429199	1.447801	13.85543636	0.003159776
1979/4/4 23:42	1979/4/4 23:59	31182.869564	0.899677	11.597689	3.003421	13.06355686	0.002707873
1979/4/5 0:13	1979/4/5 0:20	48255.612308	0.790618	7.355401	3.786946	13.12169722	0.001500694
1979/4/5 0:22	1979/4/5 0:33	21089.996485	0.815199	8.95197	1.69226	12.97961875	0.000219332
1979/4/5 3:22	1979/4/5 3:42	19204.379353	0.113332	10.188855	1.741686	15.75027905	0.003431501
1979/4/5 6:54	1979/4/5 7:02	9408.451351	0.507566	2.10822	5.706763	17.1071537	0.001239645
1979/4/5 8:15	1979/4/5 8:28	20131.230211	0.585085	4.106191	8.591082	19.03616857	0.000544151
1980/4/30 6:30	1980/4/30 6:42	5619.648563	−0.4333929191	8.8235	3.237798476	21.10045	0.001522111
1980/4/30 7:58	1980/4/30 8:56	2544.519129	−0.2345587774	6.2029	3.249310455	25.54635602	0.005681726
1980/4/30 9:49	1980/4/30 11:13	7030.402727	−0.1709014985	1.3863	5.883930386	25.03690647	0.009779977
1980/4/30 12:20	1980/4/30 12:29	3254.442615	0.460509272	6.8429	2.480049622	22.901415	0.000889523
1980/4/30 12:39	1980/4/30 14:34	5230.140303	−0.1221202688	3.6523	7.273536354	19.06261509	0.013946702
1980/4/30 14:35	1980/4/30 14:48	6492.8599	−0.2620979159	6.6234	6.106578079	17.74823055	0.001696744
1980/4/30 17:32	1980/4/30 17:41	10204.29241	−0.7912913145	4.869	4.941280652	30.077625	0.000519069
1980/4/30 17:41	1980/4/30 18:01	2199.308383	−0.08705006752	7.1919	5.192191956	30.7926119	0.001850207
1980/4/30 18:06	1980/4/30 18:54	5922.555421	−0.3673287668	6.9697	7.510142716	32.56823571	0.004285177
1980/5/1 5:18	1980/5/1 5:29	3521.778709	0.5268246802	7.8429	2.34552285	39.63756667	0.00135991
1980/5/1 5:45	1980/5/1 6:09	9580.540453	−0.5556051081	6.09	7.528737818	40.699922	0.002708765
1980/5/1 6:19	1980/5/1 6:32	9291.804766	0.1278730727	33.0064	9.955184459	66.42427976	0.002153308
1980/5/1 6:43	1980/5/1 7:22	16410.41186	0.4366267152	25.7165	15.47975839	60.977065	0.005829488
1980/5/1 7:22	1980/5/1 9:39	27122.02999	0.2215075915	11.7917	19.40783582	80.20660399	0.017400195
1980/5/1 10:48	1980/5/1 12:08	21662.15762	0.6689472525	17.4255	10.64762965	26.56091914	0.011166135
1980/5/1 12:41	1980/5/1 12:52	29642.4958	0.741710694	9.4793	17.11460987	34.97941667	0.000855321
1980/5/1 13:51	1980/5/1 15:05	34916.25032	0.3911194504	37.7558	33.62767888	55.38393667	0.007732391
1980/5/1 17:25	1980/5/1 17:33	13732.40147	−0.3620685724	11.1614	9.174181892	29.87225833	0.000966312

Table 1
(Continued)

Start Time (UT)	End Time (UT)	$\sqrt{\langle \delta u_I^2 \rangle}$ (m s^{-1})	σ_c^I (unitless)	B_0 (nT)	$\sqrt{\langle \delta B_I^2 \rangle}$ (nT)	$\langle N_p \rangle$ (#/cm^3)	$L_{I\perp}^c$ (au)
1980/5/1 19:10	1980/5/1 19:44	18259.06253	0.1938797066	25.7985	8.087129145	10.70145033	0.006585194
1980/5/1 20:02	1980/5/1 20:15	30413.0807	−0.5886443355	10.7251	11.68827886	14.88946393	0.002481809
1980/5/1 20:23	1980/5/1 21:16	25153.28794	−0.2517995594	24.3184	3.947291694	9.884305185	0.009003335
1980/5/1 21:26	1980/5/1 21:59	43981.68448	−0.7046039702	20.8502	14.84985393	9.785928382	0.002660882
1980/5/1 21:59	1980/5/1 22:18	20313.69948	−0.3410887334	23.5144	8.754573561	8.767843625	0.003750942
1980/5/2 7:54	1980/5/2 8:09	18715.60581	−0.522761734	13.8625	8.655747658	9.638555938	0.000669541
1980/5/2 8:50	1980/5/2 9:35	23445.95797	−0.733826612	11.9127	5.328218615	13.14791902	0.005920254
1980/5/2 10:26	1980/5/2 10:44	33102.55953	−0.893070396	11.6653	6.342877606	10.05700961	0.002606147
1980/5/2 10:54	1980/5/2 11:05	9358.927044	−0.8571500956	15.0898	1.852051044	10.44030917	0.001350575
1980/5/2 11:49	1980/5/2 12:06	70447.6358	−0.982181279	8.4785	11.10432413	9.032806667	0.003508634
1980/5/2 12:09	1980/5/2 12:18	21400.0475	−0.8747740701	11.9188	4.836269291	14.188625	0.001966541
1980/5/2 12:38	1980/5/2 12:47	21400.0475	−0.8747740701	11.9012	3.907375421	11.1641545	0.001380751
1980/5/2 13:33	1980/5/2 13:42	18577.17	−0.6439687796	9.9492	8.035681327	12.5821225	0.002248492
1980/5/2 16:15	1980/5/2 16:33	30228.15028	−0.8937573121	2.4539	6.821950389	10.22980474	0.003833451
1980/5/2 17:12	1980/5/2 17:30	19485.94956	−0.4926386892	10.8015	7.950812162	8.842733816	0.003239536
1980/5/2 17:42	1980/5/2 17:51	18452.60938	−0.4972097668	5.9732	4.839345464	9.26709	0.001413257
1980/5/2 17:56	1980/5/2 18:31	12516.75384	−0.6223592262	10.621	3.084996426	9.763558333	0.006484823
1980/5/2 18:35	1980/5/2 18:53	28607.19971	0.5694507492	2.5561	9.972858452	10.43384895	0.003910748
1980/5/2 18:56	1980/5/2 19:04	12521.50254	−0.8658756983	10.0196	2.590117474	9.144293333	0.000954613
1980/5/2 19:33	1980/5/2 19:54	16543.21917	−0.1404174398	9.9673	3.484357061	7.680447853	0.002669053

Note. These values are calculated from Grad–Shafranov reconstructions of the SMFRS identified in Chen & Hu (2020). Individual SMFR events are separated by an added horizontal line.

of the plasma and magnetic field data (see Figure 4), we note that there is a sharp jump in the magnetic field (b), the proton flow speed (c), the proton density (d), and the proton temperature (e) around day 122.25, which normally corresponds to an interplanetary shock. This could have gone unnoticed in the detection algorithm, due to missing periods of data that correspond well with the missing data in the particle counts data set. It is distinct from the 29 April 1978 SMFR acceleration event because the previous event seems to interrupt the decay of particle intensity after the interplanetary shock passes for just under a day and a half, whereas this event lasts for two days, occurs closer to an apparent interplanetary shock, and has a higher amplification factor. It appears that the overall decrease in the enhanced energetic particle flux before day 122.6, which we associate with SMFR acceleration, gets modified significantly by the more abrupt rise in the energetic particle flux peaking at the apparent interplanetary shock occurring on day 122.25. This implies that the energetic particle population undergoing DSA and the population experiencing SMFR acceleration are not clearly separated, such as in the 29 April 1978 SMFR acceleration event discussed above, so that some particles could be experiencing both DSA and SMFR acceleration. This could be another example of where a fraction of SMFR-accelerated particles are injected into DSA and vice versa (see also, Khabarova & Zank 2017), and where SMFR-accelerated energetic particle populations can thus serve as a significant source of suprathermal particles for injection into DSA at interplanetary shocks that have space weather implications. We also note a compression that corresponds to a gradual increase in the magnetic field, proton flow speed (a bit out of phase), and proton density, but an unexplained dip in the proton temperature that aligns with an SMFR identified in Chen & Hu (2020) that occurs from 1 May 1980 13:51:00–15:05:00 UT (day ∼122.6). Since We estimate this compression to have a width of approximately ∼0.008 au, making it much broader than the apparent interplanetary shock that passed Helios A on 1 May 1980. Because of the broadness, most particles cannot sample the full compression during one gyro-orbit. Therefore, we expect that acceleration due to this compression will be less significant when compared to DSA by the apparent interplanetary shock and acceleration due to SMFR acceleration. Evidence in support of this view includes the results from our data fits suggesting that the radial diffusion coefficient is quite small. Consequently, the energetic particles will be unable to sample the full compression ratio of the compressive structure (the radial mean free path is less than the width of the compression) whereby diffusive compression acceleration becomes less efficient than DSA. In summary, we only expect the shock to have a significant modifying effect on the enhanced energetic particle fluxes associated with SMFR acceleration. However, since this modifying effect occurs more toward the end of the decrease in the enhanced flux of SMFR-accelerated particles, we consider this to be a secondary effect on the overall enhanced flux profile that can still be fitted with our theoretical solution for SMFR acceleration, as is shown below.

Examining the data downstream of the apparent interplanetary shock, we note that the amplification factor of the enhanced energetic particle fluxes that we associated with SMFR acceleration (see Figure 5) at ∼0.59 au is greater than that of the 29 April 1978 event at ∼0.3 au (a factor of nearly two increase in radial distance), but that the amplification factor is still less than reported for the SMFR acceleration event reported at 5 au by Zhao et al. (2018). This additional result strengthens our contention that the energetic particle flux amplification factor for SMFR acceleration events grows as these events are advected with the radially expanding solar wind to larger distances from the Sun, where SMFRs expand and get weaker as reported by Chen & Hu (2020; see discussion in Section 3.1). Also, because the duration of the event is longer than the 29 April 1978 event, it follows that more SMFRs are involved in the acceleration process—and even though there are significant data gaps, this

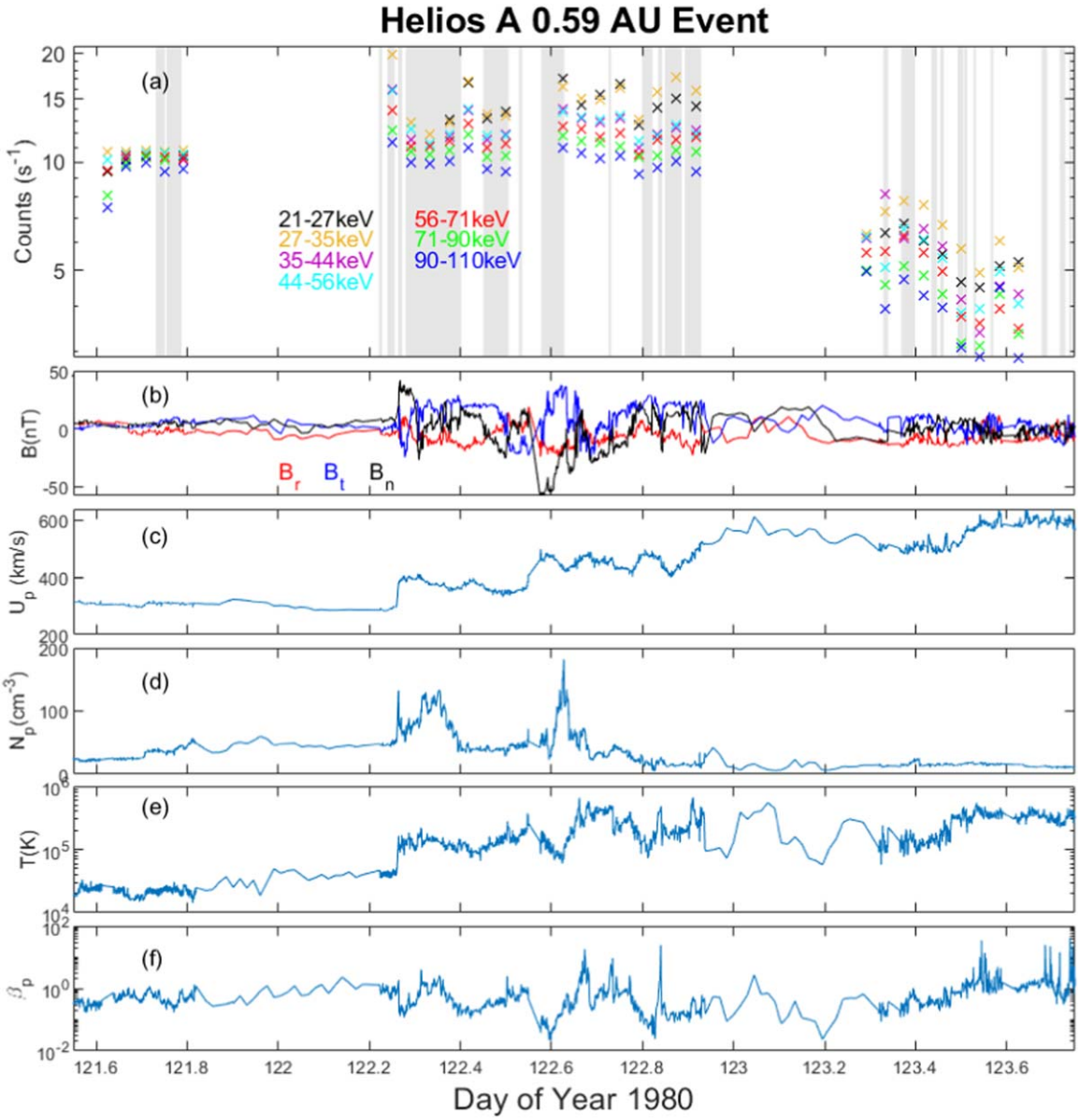

Figure 4. The top panel (a) shows the particle counts from 21 to 110 keV registered by the E8 detector on Helios A. The gray bars represent the time and duration of SMFRs identified by Chen & Hu (2020). The other panels show: (b) the magnetic field presented in the RTN coordinate system, (c) the proton flow speed as measured in the spacecraft frame, (d) the proton number density, (e) the proton temperature, (f) and the plasma beta, presented as a time series.

event represents an opportunity to do a statistically significant study on SMFRs that are actively accelerating particles (see Table 1 for SMFR parameters and Figure 6 for Grad–Shafranov reconstructions of selected SMFRs from the acceleration region).

We performed the same analysis as we did for the previous event, to determine whether the region we attribute to SMFR acceleration could be dominated by Alfvén waves. The analysis was inconclusive. The results exhibit large fluctuations in the normalized cross helicity and normalized residual energy immediately downstream of the apparent interplanetary shock, while yielding little information concerning the presence of Alfvén waves overall, and thus are not included.

3.3. SMFR Acceleration Events of 3 April 1979

Two SMFR acceleration events were identified, with one on either side of the interplanetary shock that passed by Helios A on 3 April 1979 at 19:45:57 UT (red dashed line labeled "shock" in the top left panel of Figure 7). The first event can only be partially explained and the second event cannot be explained with our theory. During Event A (ahead of the interplanetary shock), particle counts begin to increase around day 92.75 in 1979 and then fall back down to background levels near day 93.5, before the counts spike near the shock crossing later that day. The bottom left panel of Figure 7 shows the fluxes measured by the E8 detector from 21 to 353 keV for event A after normalizing them to the chosen injection point (red dashed line labeled "Injection Point"). While there is no consistent pattern in the flux-enhancement profile between 21 and 44 keV, it can be seen that the flux-enhancement profiles from 44 to 353 keV decrease in their amplification factor as energy increases, which is the opposite of what is predicted by our transport theory. However, the bottom right panel of Figure 7 shows the flux-enhancement profiles from 353 to 677 + keV of event A, which match the predictions from our

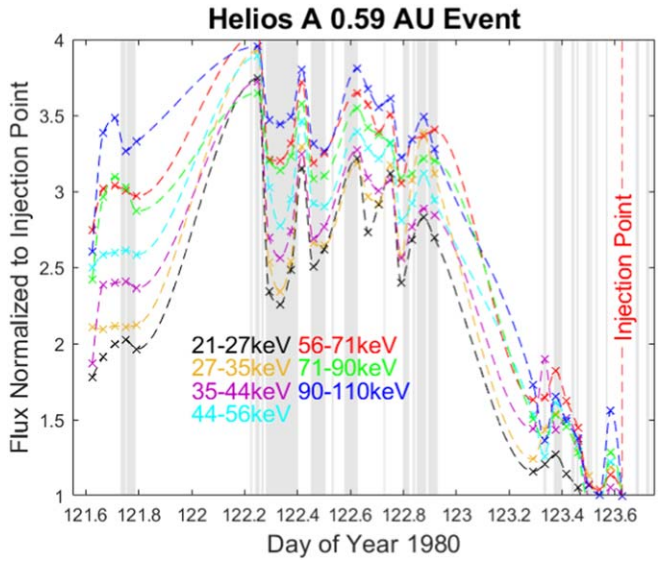

Figure 5. The flux-enhancement profile for the 1 May 1980 SMFR acceleration event at 0.59 au. The "x" symbols represent the measured flux normalized to the chosen injection point (dashed vertical line), and the dashed lines are a cubic interpolation of the measurements. The gray bars represent the time and duration of SMFRs identified by Chen & Hu (2020).

transport theory. Event A was not selected for the data fits, due to the plateau-like shape of the curves above 353 keV, which cannot be captured by the solution given by Equation (5).

The parameters of the SMFRs associated with this anomalous event can be found in Table 1. Our theory for SMFR acceleration applies in the limit that the energetic particle gyroradius is considerably less than the mean SMFR width, but the particles are still able to traverse and interact with numerous active SMFRs in order to experience efficient acceleration. This yields the theoretical prediction that the energetic particle flux amplification factor increases with particle energy. However, if the gyroradii in some SMFR acceleration event compared to the average SMFR width were considerably reduced, the lower suprathermal energy particles could get trapped inside SMFRs, thus being less likely to encounter active SMFRs that generate efficient energy gain. This could then produce the inverse relationship where the flux amplification factor decreases with increasing particle energy. The more mobile higher-energy particles, on the other hand, would still be able to interact with numerous active SMFRs to experience efficient acceleration and adhere to the flux amplification relationship predicted by our theory. This implies that, for some SMFR acceleration events, there should be a gyroradius threshold value such that, for gyroradii smaller than the threshold value, the inverse flux amplification relationship holds. For gyroradii larger than the threshold value flux, the amplification relationship predicted by the theory applies. We use the SMFR parameters given in Table 1 to calculate the average gyroradii for each energy channel available for Helios A E8 data normalized to the average SMFR width $L_{I\perp}^{c}$. The results of these calculations are presented in Table 2, where we can see that, above 353 keV, the gyroradii are above 7% of the average SMFR scale length. These are similar to the values calculated for the 29 April 1978 event (see again Table 2), which better follows the predictions of our transport theory. This could be a threshold value above which particles can more freely move from one SMFR to another and thus are more likely to encounter more active SMFRs and gain energy. However, the values calculated for the 1 May 1980 event are significantly smaller during an event that follows the predictions of our theory, so this is not an exact value (see Table 2). The event behind this interplanetary shock does not demonstrate this same behavior.

Event B (behind the interplanetary shock) is similarly puzzling, in that it demonstrates the same inverse amplification factor effect as event A. The interplanetary shock passed Helios A on 3 April 1979 at 19:45:57 UT, and the particle counts peak near the shock structure, as predicted by classical DSA theory. The particle counts then decay after the interplanetary shock passes, until day 94.5, where they reach background levels again. Around day 94.75, they begin to rise again and are far enough separated from the interplanetary shock to not be associated with it. From 56 to 279 keV, the flux-enhancement profiles amplification factors decay for rising energy, which cannot be captured by our transport theory. The parameters of the SMFRs associated with this anomalous event can be found in Table 1. Following the same procedure as above, we see that the gyroradii for each energy channel are not quite as large, compared to the average SMFR scale length, as they are for the previous event (see Table 2 for calculated values). However, the gyroradii do approach the threshold that was discussed above.

3.4. SMFR Acceleration Event of 13 January 1979

Another event that demonstrates a flux-enhancement profile that is not consistent with our transport theory occurs after an interplanetary shock that passes Helios A on 13 January 1979 at 08:00:21 UT. Figure 8 (left panel) shows the particle counts associated with the event. The particle counts peak just before the interplanetary shock passes Helios A and quickly decays downstream, following the predictions of classical DSA theory. Nearly half a day after the interplanetary shock passes (day 13.7), we see a smaller-sized jump, followed by a plateau in the particle counts until day 14.1, where the counts fall back down to background rates. Figure 8 (right panel) shows the flux-enhancement profile for 21 to 174 keV protons. The amplification factor associated with the plateau for each energy channel decreases with increasing particle energy. As in the previous example (Section 3.3), we believe that the inability of the particles to escape relatively "quiet" SMFRs could cause this inverse amplification factor to come about, and this can be demonstrated by the particle gyroradius being significantly smaller than than the perpendicular scale width of the SMFR (see Table 1 for the reconstructed SMFR parameters). Table 2 demonstrates the calculated gyroradii for each energy channel during the event, which reveals that they are smaller than 1% of the size of the SMFR. This lends credibility to the idea that these particles are "trapped" in the SMFRs and cannot easily escape.

4. Fits of SMFR-accelerated Energetic Particle Data

We fit the data for each new SMFR acceleration event using a Metropolis–Hastings Algorithm as described in Zhao et al. (2019) and Bonamente (2013), the underlying assumption being that each measurement is distributed as a Gaussian random variable. Then the likelihood of a set of parameters can be estimated by the chi-squared parameter: $\chi^2 = \Sigma_i (X_i - f_i(\theta))^2/\sigma_i^2$ where X_i are the in situ flux measurements, $f_i(\theta)$ are the calculated model values for each set of parameters (θ), and σ_i are the variance values for each measurement. Because of the assumptions associated with the Parker-type transport equations (i.e., the particle distributions

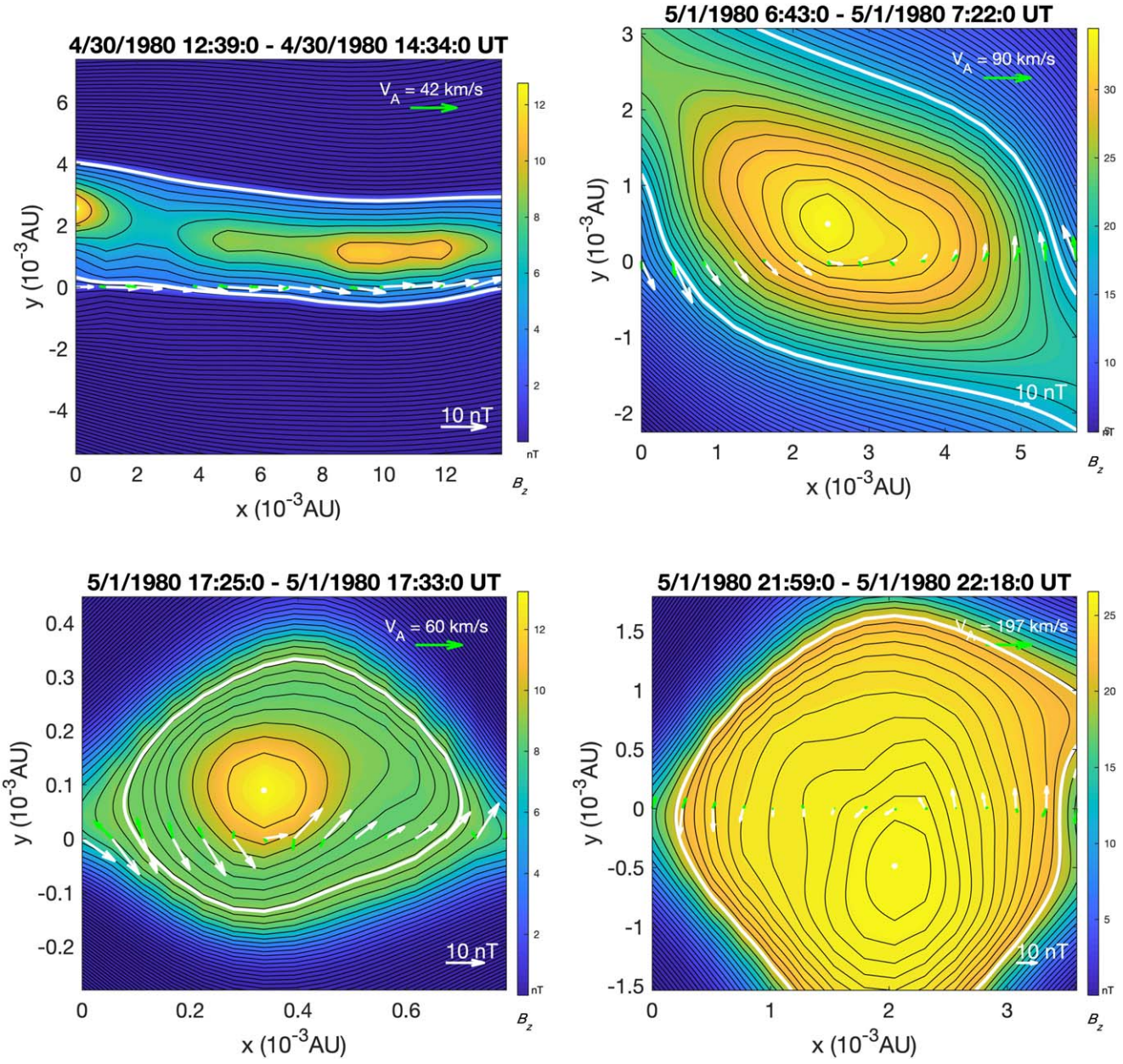

Figure 6. Grad–Shafranov reconstructions of some SMFRs from the 1 May 1980 event identified by Chen & Hu (2020). Displayed are the 2D SMFR twist or island field component (black contour lines) and the out-of-plane axial (guide) field component (colored regions). The white and green arrows indicate the magnetic field and flow vectors, respectively, along the path of the spacecraft.

are nearly isotropic), the data to be used for the fitting technique were calculated by averaging the particle counts over each of the 16 directions (from facing directly at the Sun rotating 360° in the ecliptic plane) in the E8 detector for a single energy channel ($\langle x\rangle = (1/m)\Sigma_1^{16} x_{\rm dir}$, where m is the number of measurements that are not missing) and then normalizing it to the energy range of the bin it was recorded in. Because we only use the E8 detector from Helios A, the geometric factor for each energy bin is the same. Therefore, to replicate a flux from one energy bin normalized to a flux from another energy bin, we can simply take particle counts for an energy bin divided by the energy range of that bin and normalize it to the same value for another energy bin. X_i was calculated by taking the minimum energy bin data from a specific event and normalizing it to the maximum energy bin data at the chosen injection point (i.e., $X_i = \langle x(r_i, p_{\rm min})\rangle / \langle x(r_0, p_{\rm max})\rangle$). The variances are then calculated in the typical manner ($\Delta_i^2 = (1/(m)(m-1))\Sigma_1^{16}(x_{\rm dir} - X_i)^2$); however, for the data fit, we use the normalized variance (i.e., $\sigma_i^2 = \Delta_i^2/\langle x(r_0, p_{\rm max})\rangle^2$). It should be noted that measurements that only include data from one direction (i.e., $m = 1$) are not used for the data fits. The model values are estimated by calculating the differential intensity from the analytical solution of the distribution function (see Equation (5)) using $J(r, p) = p^2 f(r, p)$, which was normalized in the same way as the other quantities (i.e., $f_i(\theta) = J(r_i, p_{\rm min})/J(r_0, p_{\rm max})$). This is done to include the physics that is contained in the exponent of the p/p_0 term—otherwise, normalizing by the same energy would eliminate the p/p_0 exponent altogether. By normalizing the lowest-energy flux

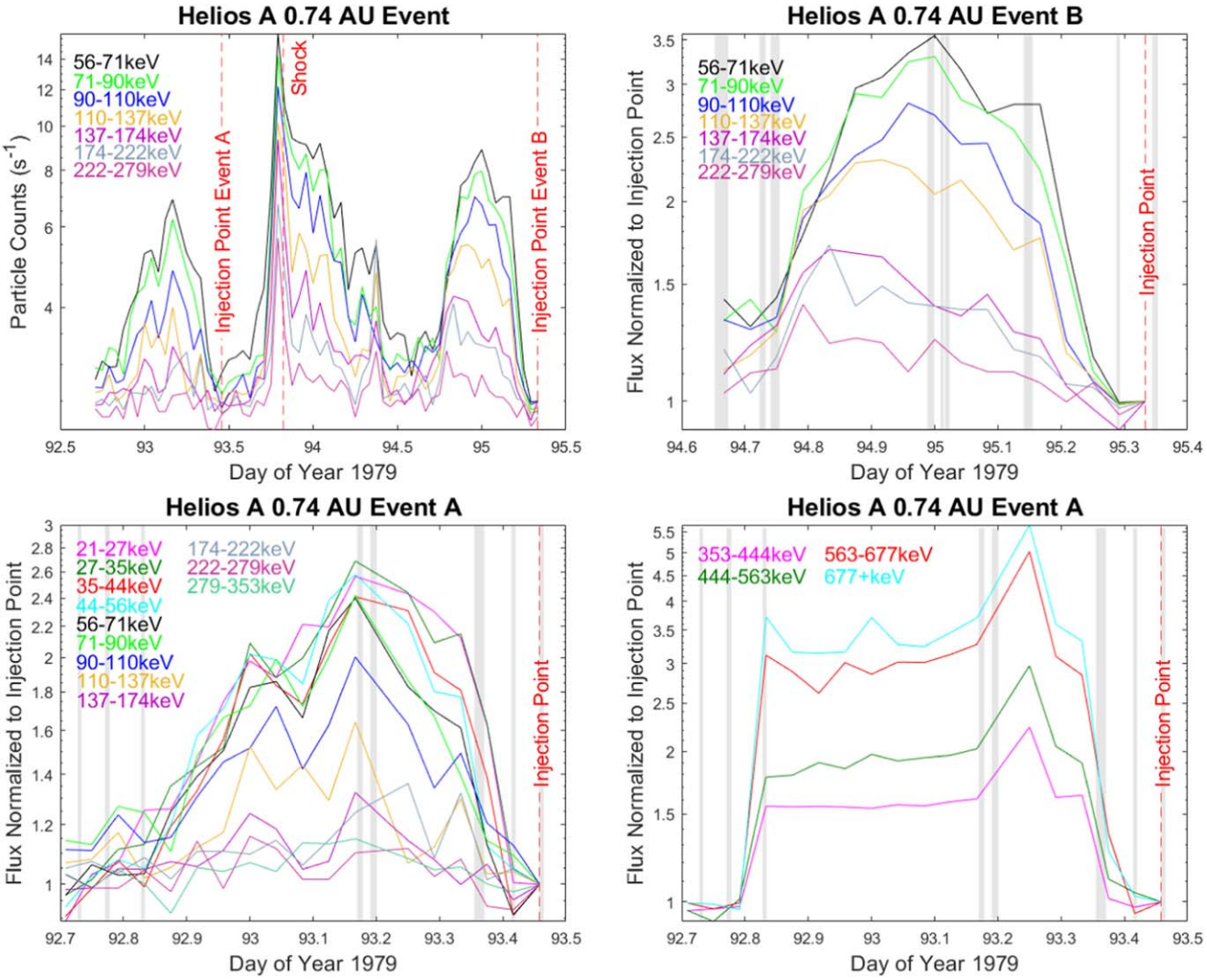

Figure 7. Top left: Particle counts from 56 to 279 keV in the E8 detector from Helios A showing the interplanetary shock that occurred on 3 April 1979 at 19:45:57 UT and the two anomalous flux-enhancement events nearby on both sides. Top right: Flux-enhancement factor increases inversely with particle energy for Event B behind the shock, contrary to the theoretical prediction. Bottom left: Flux-enhancement factor increases inversely with particle energy below 353 keV for Event A ahead of the shock. Bottom right: Flux-enhancement factor increases with particle energy as predicted by the theory for Event A above 353 keV ahead of the shock. The gray bars represent the time and duration of SMFRs identified by Chen & Hu (2020).

data (which should have the higher flux because there are more low-energy particles than high-energy particles) to the higher-energy flux, we seek to accentuate the differences between the model and the data, thus decreasing the amount of time needed to run the fit. Each Markov Chain is run for 10^6 steps. Five of the six parameters that are included in the model are varied (D_0, κ, u_{Er}, $v_{\rm esc}$, $\langle\nu^I_{\rm COM}\rangle$) to find the best-fit parameters (u_0 is calculated from the average plasma data observed by Helios A).

4.1. The SMFR Acceleration Event of 29 April 1978

Figure 9 shows the full theoretical solution (5) (solid lines) as fitted to the Helios A energetic particle data at 0.3 au ("x" symbols) with the Metropolis–Hastings algorithm. The theoretical fit is determined by finding the best-fit parameters, which are presented in Figure 10 and Equation (13). It is clear from Figure 10 that D_0, κ and $v_{\rm esc}$ have well-defined peaks with values much larger than the magnitude of the peak value for u_{Er} that is much smaller than the limiting value for u_{Er} inferred from the condition $u_{Er}^2/9\kappa D_0 < 1$, which is discussed above. The best-fit parameter for $\langle\nu^I_{\rm COM}\rangle$, on the other hand, has a nearly uniform distribution, indicating that the best-fit solution to the data is largely insensitive to its value. This can be understood by examining where $\langle\nu^I_{\rm COM}\rangle$ occurs in solution (5). Consider first the dependence of the exponent of r/r_0 on $\langle\nu^I_{\rm COM}\rangle$ in solution (5), given by

$$\bar{a} - \tilde{a}\frac{B}{2A} = -\left(1 - \frac{u_0 - u_{Er}}{2\kappa}\right) + \frac{u_{Er}}{6\kappa}\frac{(3 - (1/3D_0)[\langle\nu^I_{\rm COM}\rangle - u_{Er}u_0/\kappa + u_{Er}^2/\kappa - 2u_0])}{(1 - u_{Er}^2/9\kappa D_0)}.$$

Since we already know that the best data fit requires a relatively small value for $|u_{Er}|$, we can approximate the denominator of the last term to be one while neglecting the term with u_{Er}^2. Then, by determining the median and standard deviation values for

Table 2
Calculated Gyroradii for Each SMFR Event

Event	R_{sc} (au)	Energy (keV)	21–27	27–35	35–44	44–56	56–71	71–90	90–110	110–137	137–174	174–222	222–279	279–353	353–444	444–563	563–677	677+
1978/4/29	0.3	$r_g/L_{I\perp}^c(10^{-2})$	4.558	5.180	5.847	6.579	7.414	8.348	9.304	10.339	11.602	13.092	14.725	16.539	18.573	20.877	23.166	25.984
1979/1/13	0.93	$r_g/L_{I\perp}^c(10^{-3})$	1.502	1.707	1.927	2.168	2.444	2.751	3.066	3.408	3.824	4.315	4.853	5.451	6.121	6.881	7.635	8.564
1979/4/3 A	0.74	$r_g/L_{I\perp}^c(10^{-2})$	1.733	1.969	2.223	2.501	2.818	3.173	3.537	3.930	4.410	4.976	5.597	6.287	7.060	7.936	8.806	9.877
1979/4/3 B	0.74	$r_g/L_{I\perp}^c(10^{-2})$	1.563	1.776	2.005	2.256	2.542	2.862	3.190	3.545	3.978	4.489	5.049	5.670	6.368	7.158	7.943	8.909
1980/5/1	0.59	$r_g/L_{I\perp}^c(10^{-3})$	1.033	1.174	1.325	1.491	1.680	1.892	2.109	2.344	2.630	2.967	3.338	3.749	4.210	4.732	5.251	5.890

Note. Gyroradii were calculated using the average energy from each bin. The heliocentric distance of the spacecraft is also noted for each event in the second column.

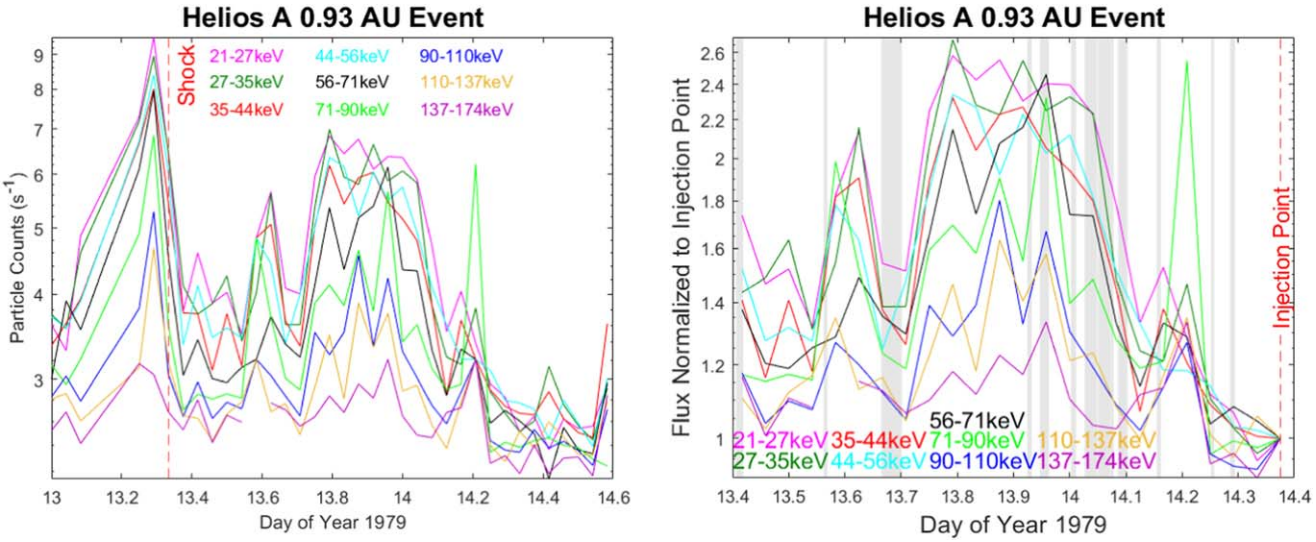

Figure 8. Left: Particle counts from 21 to 174 keV in the E8 detector from Helios A, showing the interplanetary shock that occurred on 13 January 1979 at 08:00:21 UT (shown as the red dashed line) and an anomalous flux-enhancement event immediately downstream of the shock. Right: Flux-enhancement factor increases inversely with particle energy, contrary to the theoretical prediction.

each parameter from Figure 10, we find that

$$\begin{aligned}\frac{D_0}{u_0} &= 6.41 \pm 2.35 \times 10^{-1},\\ \frac{\kappa}{u_0} &= 9.18 \pm 0.05 \times 10^{-2},\\ \frac{u_{Er}}{u_0} &= -5.66 \pm 1.70 \times 10^{-2},\\ \frac{v_{\rm esc}}{u_0} &= 8.99 \pm 2.61,\\ \frac{\overline{\langle \nu^I_{\rm COM}\rangle}}{u_0} &= 4.15 \pm 6.27. \end{aligned} \quad (13)$$

Plugging in the median values for all parameters in the expression for the exponent of r/r_0—except $\overline{\langle \nu^I_{\rm COM}\rangle}$, for which the maximum value (i.e., $\overline{\langle \nu^I_{\rm COM}\rangle}/u_0 \to 10$) is specified—reveals that the last term of the exponent is an order of magnitude lower than the first term (≈ -0.2 as compared to ≈ 4). Therefore, even if $\overline{\langle \nu^I_{\rm COM}\rangle}$ is maximized, it has minimal effect on the exponent of r/r_0.

Second, in the argument of the modified Bessel function in solution (5), $\overline{\langle \nu^I_{\rm COM}\rangle}$ is present in b, according to the expression

$$b = \sqrt{\left(1 - \frac{(u_0 - u_{Er})}{2\kappa}\right)^2 + \frac{v_{\rm esc}}{\kappa} + \frac{D_0}{4\kappa}\frac{(3 - (1/3D_0)[\overline{\langle \nu^I_{\rm COM}\rangle} - u_{Er}u_0/\kappa + u^2_{Er}/\kappa - 2u_0])^2}{(1 - u^2_{Er}/9\kappa D_0)}}.$$

Following the same procedure as for the previous term, we see that the combined size of the first term in b containing the geometric factor (size $\approx$16) and the escape term (size $\approx$90) is an order of magnitude greater than the final term ($\approx$6), meaning that in b the importance of $\overline{\langle \nu^I_{\rm COM}\rangle}$ is also minimal. Since b and the exponent of r/r_0, which are both weakly dependent on $\overline{\langle \nu^I_{\rm COM}\rangle}$, predominantly determine the spatial profile of the solution, it stands to reason that the fitting method cannot locate a highest probable value for $\overline{\langle \nu^I_{\rm COM}\rangle}$. Thus, we can reasonably rule out first-order Fermi acceleration due to the mean SMFR compression rate as the dominant SMFR acceleration mechanism in this event.

Similarly, given that u_{Er} is minimized by the fitting technique, combined with the fact that a large u_{Er}value causes $1 - u^2_{Er}/9\kappa D_0 < 0$, which leads to the full solution (Equation (5)) becoming complex, we can conclude that acceleration by the mean turbulent motional electric field parallel to the guide field, as expressed collectively by the combination of the mixed-derivative transport term (fifth transport term of Equation (4)) and the term modeling adiabatic heating for $u_{Er} < 0$ (in third transport term in Equation (4)), cannot dominate SMFR acceleration in these SMFR acceleration events. This leaves the second-order Fermi SMFR acceleration mechanism (D_0) as the SMFR acceleration mechanism that does most of the work accelerating particles. Che & Zank (2020) come to a similar conclusion using a particle-in-cell (PIC) simulation to investigate electron acceleration in an electron Kelvin–Helmholtz instability. The authors also agree that the SMFR acceleration mechanism due to island contraction is inefficient compared to the second-order Fermi process associated with stochastic inductive electric fields. In the interest of supporting this argument, we plot the second-order Fermi solution (Equation (8)) with the data in Figure 11 where the best-fit parameters from Equation (13) are used, showing that with second-order Fermi acceleration alone, one comes close to reproducing the observed flux enhancements. Nonetheless, a good reproduction of the observed flux enhancements does require a minor contribution from the mean parallel turbulent motional electric field in SMFRs collectively through the mixed-derivative transport term and the adiabatic heating term, as well as the term for first-order Fermi acceleration due to the average

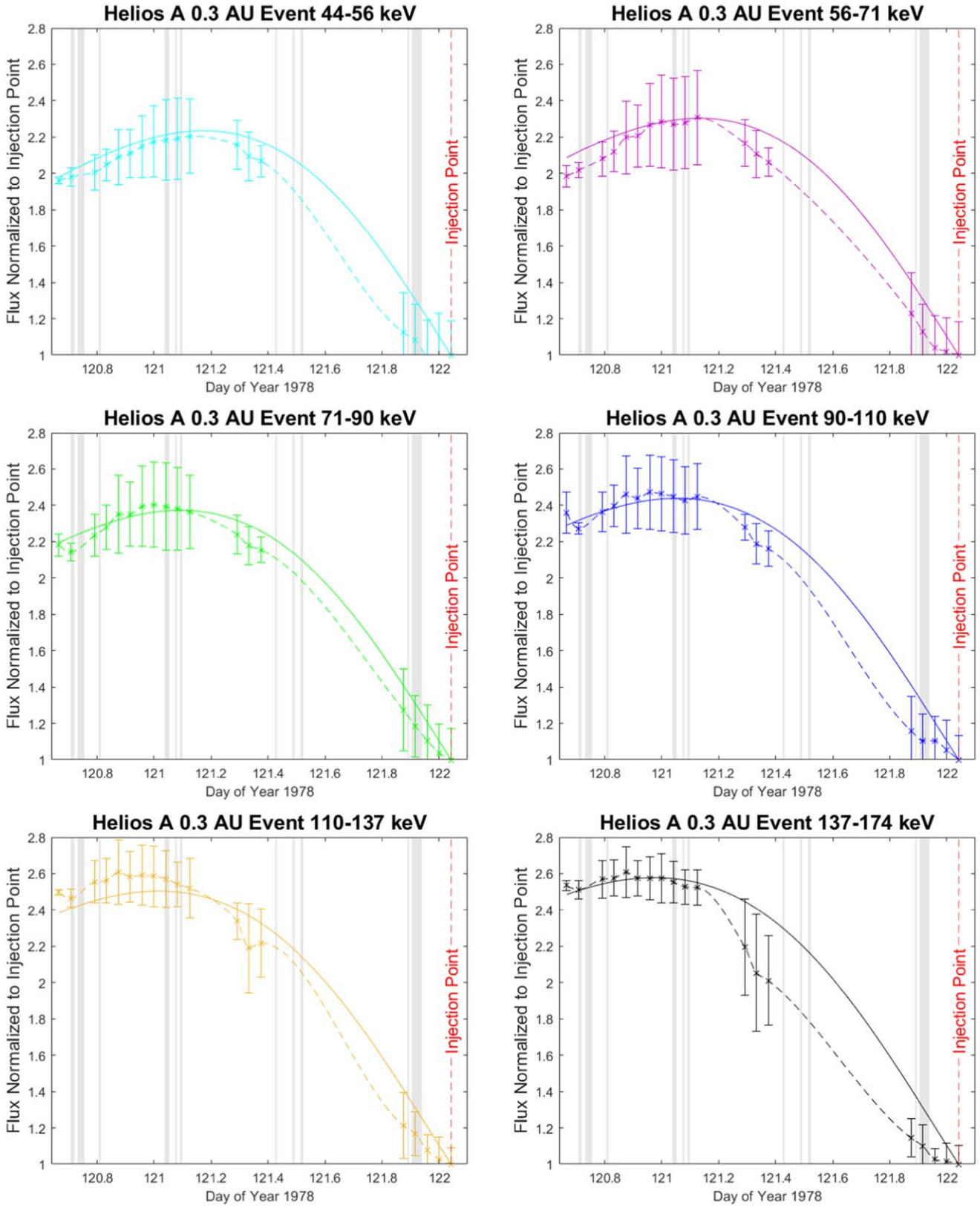

Figure 9. Full solution fit for the 29 April 1978 SMFR acceleration event energetic proton fluxes observed at 0.3 au for various particle energies. The energies follow the same color code as in Figure 2. The "*x*" symbols represent data points, the solid curves denote the fit of the full analytical solution to the data with the Metropolis–Hastings Algorithm, and the dashed lines represent a cubic interpolation of the data. Both the data and the theoretical curves for all particle energies were normalized to a value of one at the chosen particle source injection point indicated by the vertical dashed red line. The gray bars represent the time and duration of SMFRs identified by Chen & Hu (2020).

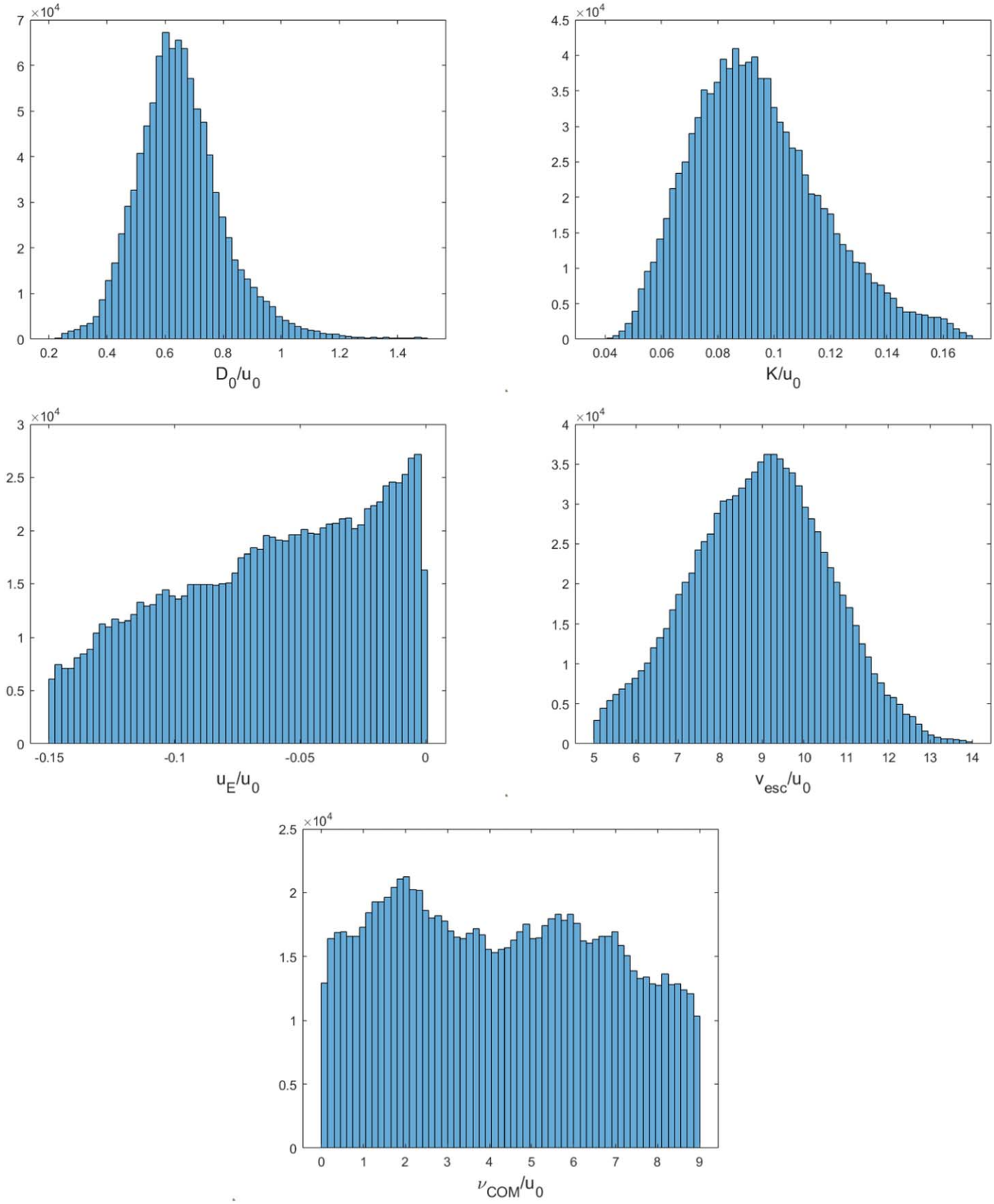

Figure 10. Probability distributions of fitting parameters normalized to the solar wind speed u_0 for various transport coefficients appearing in the analytical solution for SMFR acceleration as generated by the Metropolis–Hastings Algorithm for the 29 April 1978 SMFR acceleration event.

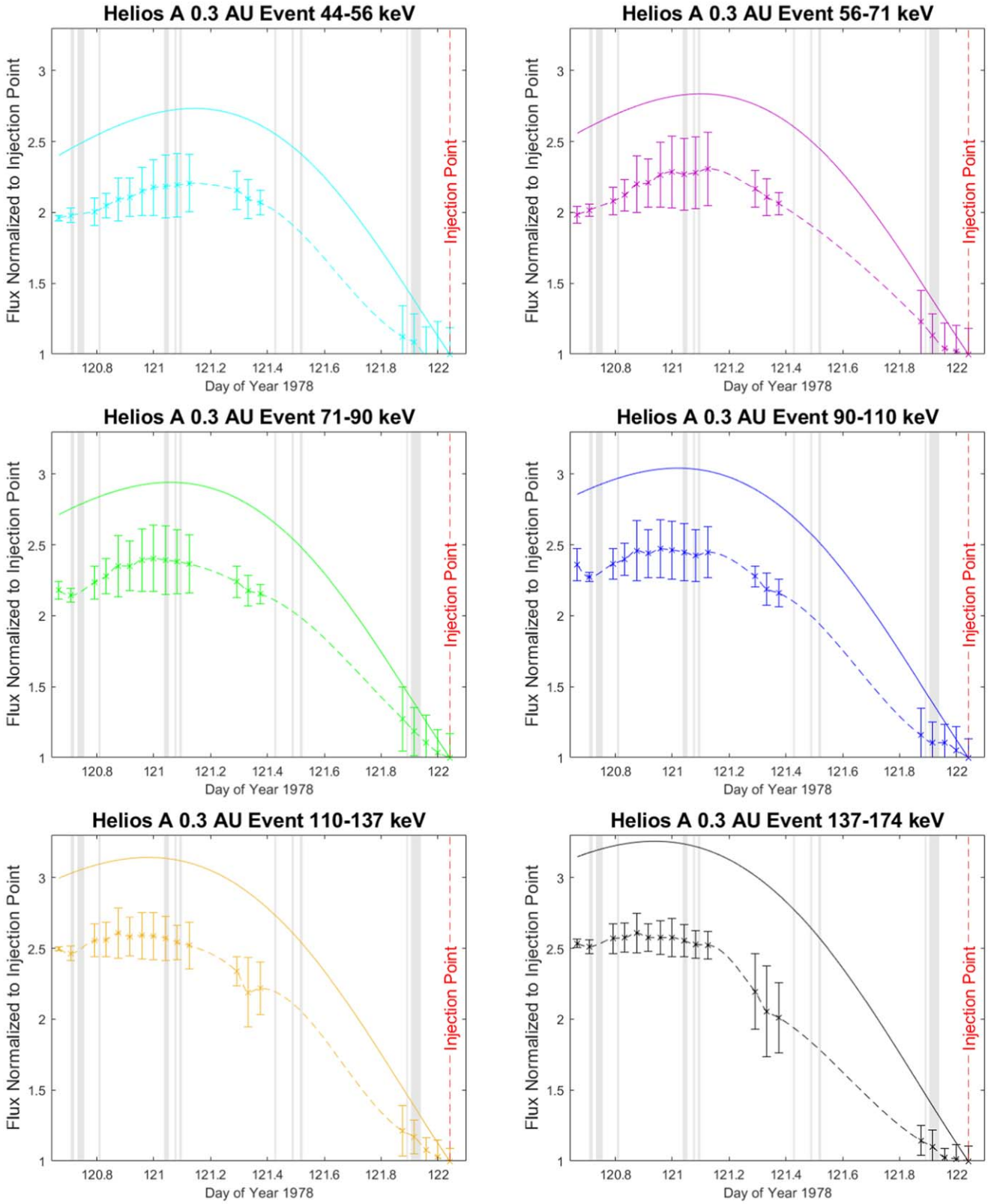

Figure 11. Second-order Fermi acceleration solution fit to the 29 April 1978 event energetic proton fluxes observed at 0.3 au for various particle energies. The energies follow the same color code as in Figure 2. The "x" symbols represent data points, and solid curves denote the fit of the full analytical solution to the data with the Metropolis–Hastings Algorithm. Both the data and the theoretical curves for all particle energies were normalized to a value of one at the chosen particle source injection point indicated by the vertical dashed line. The gray bars represent the time and duration of SMFRs identified by Chen & Hu (2020).

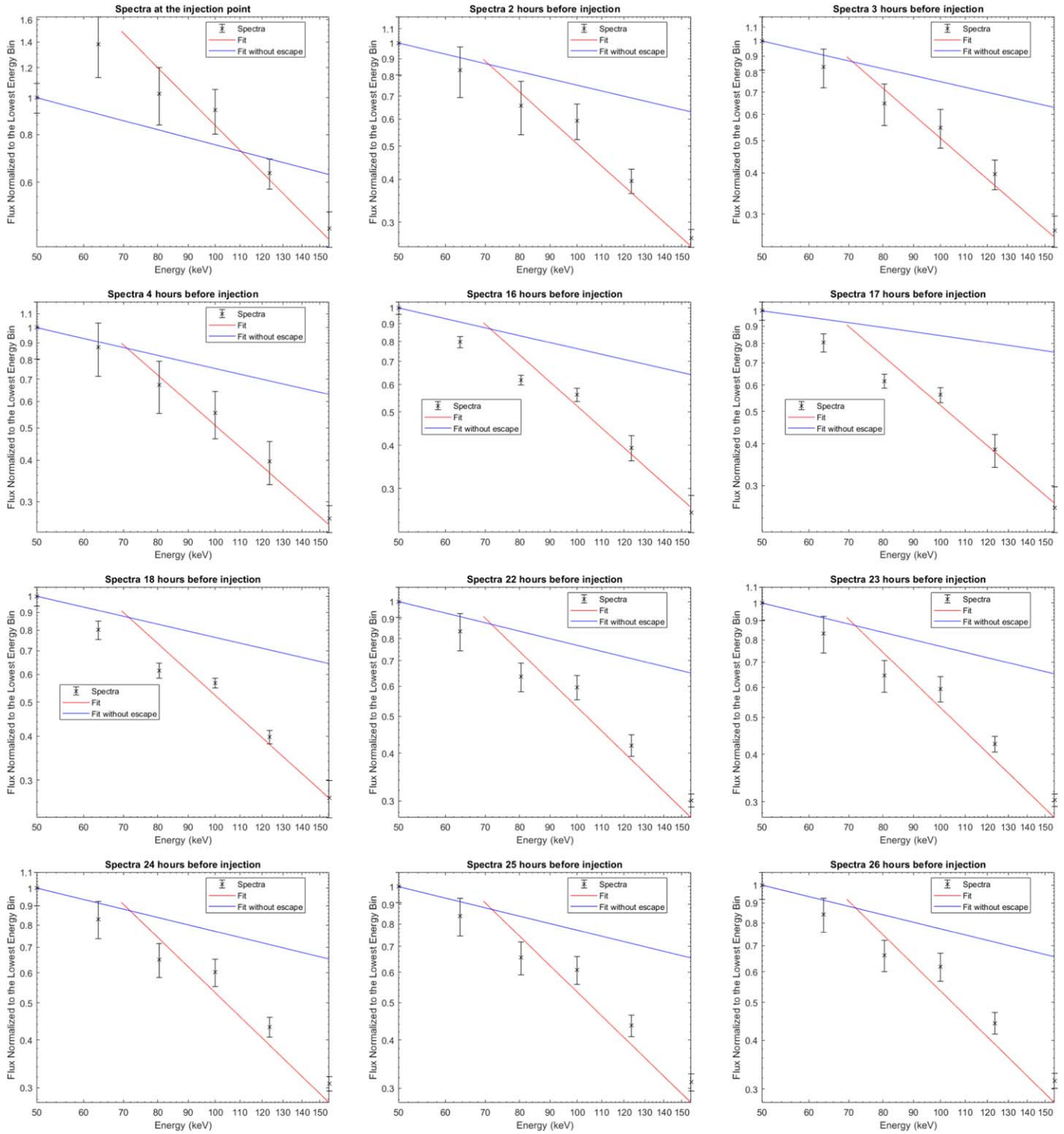

Figure 12. Observed energetic proton spectral flux data ("x"-symbols) of the 29 April 1978 SMFR acceleration event at 0.3 au as a function of particle kinetic energy in keV normalized to the flux value of the lowest energy bin. The solid red lines indicate the best fit of the full analytical solution to the data with the aid of the Metropolis–Hastings algorithm, while the blue lines represent the analytical solution without particle escape from the SMFR region.

SMFR compression rate. A minor role for the mixed-derivative transport in SMFR acceleration featured also in the results presented by Zhao et al. (2018).

Inspection of the best-fit values of the transport parameters listed in Equation (13) emphasizes that a strong escape term (large values for $v_{\rm esc}$) is vital to reproducing the observed spectral slopes (see Figure 12, where the spectral slopes excluding escape, the blue lines, are entirely too hard to reproduce observations, the "x" symbols) and spatial profiles. Consider now the expression for the spectral power-law index

predicted by the full solution in the high-energy limit at the particle injection position given by

$$\alpha = \frac{1}{2}\frac{(3-(1/3D_0)[\overline{\langle \nu^I_{\rm COM}\rangle} - u_{Er}u_0/\kappa + u^2_{Er}/\kappa - 2u_0])}{(1-u^2_{Er}/9\kappa D_0)} + \sqrt{\frac{\kappa}{D_0}\frac{1}{1-u^2_{Er}/9\kappa D_0}} \times \sqrt{\left(1-\frac{(u_0-u_{Er})}{2\kappa}\right)^2 + \frac{v_{\rm esc}}{\kappa} + \frac{D_0}{4\kappa}\frac{(3-(1/3D_0)[\overline{\langle \nu^I_{\rm COM}\rangle} - u_{Er}u_0/\kappa + u^2_{Er}/\kappa - 2u_0])^2}{(1-u^2_{Er}/9\kappa D_0)}}.$$

By inserting the best-fit values of Equation (13) into this expression, we estimate that $\alpha = 2.39$ ($f(p) \propto p^{-2.39}$) in the absence of particle escape ($v_{\rm esc} = 0$). This spectra is harder than the hardest possible accelerated spectrum due to second-order Fermi acceleration at the injection position ($\alpha \sim 3$ at $r = r_0$). Both other mechanisms allow for spectral slopes that are much harder than $\alpha \sim 3$ at the injection position (for compression acceleration $\alpha \sim 0$ in the strongest case, and for acceleration due to the component of the mean turbulent motional electric field parallel to the guide magnetic field as represented collectively by the mixed-derivative transport term and the adiabatic heating term $\alpha \sim 3/2$). This confirms our conclusion that, while second-order Fermi plays a dominant role in accelerating the particles, acceleration of the particles by the component of the mean turbulent motional electric field parallel to the guide/background magnetic field as represented collectively in the mixed-derivative transport term and the adiabatic heating term, as well as by the mean compression of the SMFR field, must play a non-negligible secondary role.

If we restore particle escape in the expression for α, we find that α increases strongly from $\alpha = 2.39$ to $\alpha = 4.71$. This illustrates the large role particle escape from the SMFR acceleration region plays in steepening the SMFR-accelerated particle spectrum to produce good fits of the theoretical solution to the data as shown in Figure 12. We also investigated the possibility that some of the spectral steepening can be attributed to self-consistent SMFR acceleration, where the energy exchange between energetic particles and SMFRs should be taken into account. For this purpose, we calculated the average magnetic pressure in the magnetic (twist) component for the identified SMFRs during this acceleration event and compared it to the pressure calculated from the energetic particle spectra. We find that the pressure in SMFR-accelerated particles is many orders of magnitude less than the magnetic pressure in the SMFRs, which leads to the conclusion that this event does not represent a time period when energetic particles are accelerated in a self-consistent manner by SMFRs. This confirms the correctness of using a test particle to model SMFR acceleration of energetic particles, and suggests that the escape term represents particles escaping from the SMFR region exclusively.

Another striking feature of the fit values in Equation (13) is how small the radial diffusion coefficient κ is. We speculate that, because the particles do not diffuse efficiently (κ is minuscule compared to other transport parameters; see Equation (13)), the ability of particles to freely move from one SMFR to another is primarily determined by the escape term, thus explaining its stature the data fit.

4.2. The SMFR Acceleration Event of 1 May 1980

As discussed above, we expect the shock, but not the compression, to have a significant modifying effect on the enhanced energetic particle fluxes associated with SMFR acceleration. However, since this modifying effect occurs more toward the end of the decrease in the enhanced flux of SMFR-accelerated particles, we consider this to be a secondary effect on the overall enhanced flux profile that can still be fitted with our theoretical solution for SMFR acceleration. The results from applying the Metropolis–Hastings algorithm to the 1 May 1980 event are eerily similar to those for the event in the previous section. Figure 13 displays the full theoretical solution (Equation (5)) fit (solid curves) that the Metropolis–Hastings algorithm determined for these data ("x" symbols). The results of the Metropolis–Hastings algorithm for each fitting parameter are displayed in Figure 14, from which we determined the median and standard deviation values for all the fitting parameters:

$$\begin{aligned}
\frac{D_0}{u_0} &= 8.47 \pm 0.50 \times 10^{-1},\\
\frac{\kappa}{u_0} &= 5.78 \pm 0.02 \times 10^{-2},\\
\frac{u_{Er}}{u_0} &= -6.38 \pm 0.46 \times 10^{-2},\\
\frac{v_{\rm esc}}{u_0} &= 10.23 \pm 6.67,\\
\frac{\overline{\langle \nu^I_{\rm COM}\rangle}}{u_0} &= 5.25 \pm 6.47. \qquad (14)
\end{aligned}$$

Examining the fitting parameters in Figure 14 and Equation (14) for this SMFR acceleration event observed at ~0.59 au leads to the same conclusions as for the acceleration event at ~0.3 au discussed in the previous section. As before, the fitting values for the mean SMFR compression rate $\langle \nu^I_{\rm COM}\rangle$, which determines first-order Fermi SMFR acceleration due to the mean SMFR compression rate, has a relatively uniform distribution in Figure 14 because of its low impact on the spatial profile of the solution. The fitting parameter u_{Er} associated with acceleration by the mean turbulent motional electric field parallel to the guide/background magnetic field is again minimized by the fitting procedure to be much smaller than the condition for a real solution ($u^2_{Er}/9\kappa D_0 < 1$). As in the previous acceleration event, this implies that second-order Fermi SMFR acceleration must be the dominant SMFR acceleration mechanism. This is confirmed by Figure 15, in which the second-order Fermi solution of Equation (8) (solid curves) is compared with the observations ("x" symbols). Similarly to the case of the 29 April 1978 event, here we see that the second-order Fermi mechanism alone brings one close to reproducing the observations, but that the other SMFR acceleration mechanisms are needed for a good data fit. Both first-order Fermi SMFR acceleration due to the mean SMFR compression rate, as well as acceleration by the mean turbulent motional electric field parallel to the guide field manifested in the mixed-derivative and the adiabatic heating transport terms, play a secondary but significant role in accelerating the particle population.

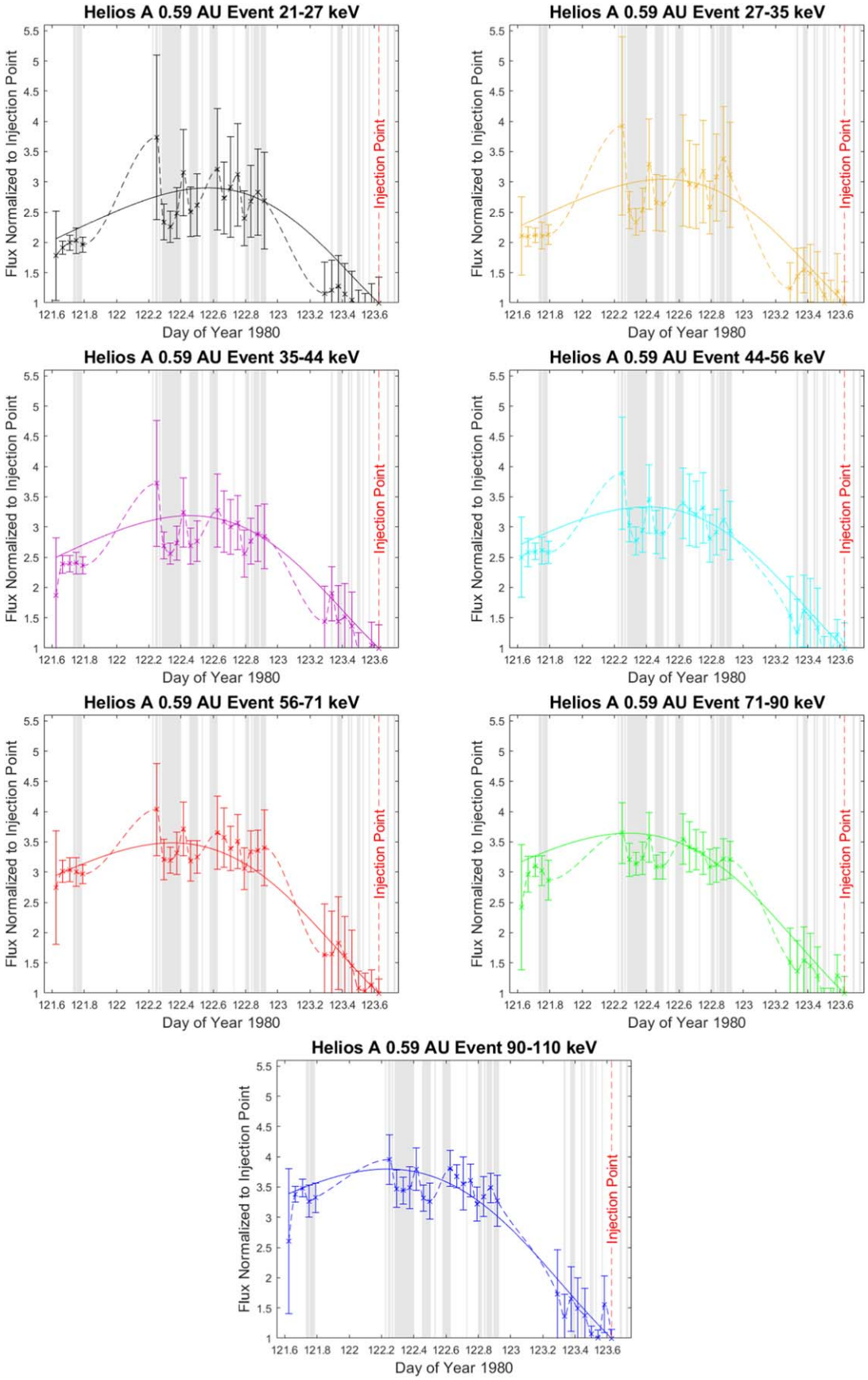

Figure 13. Same format as Figure 9.

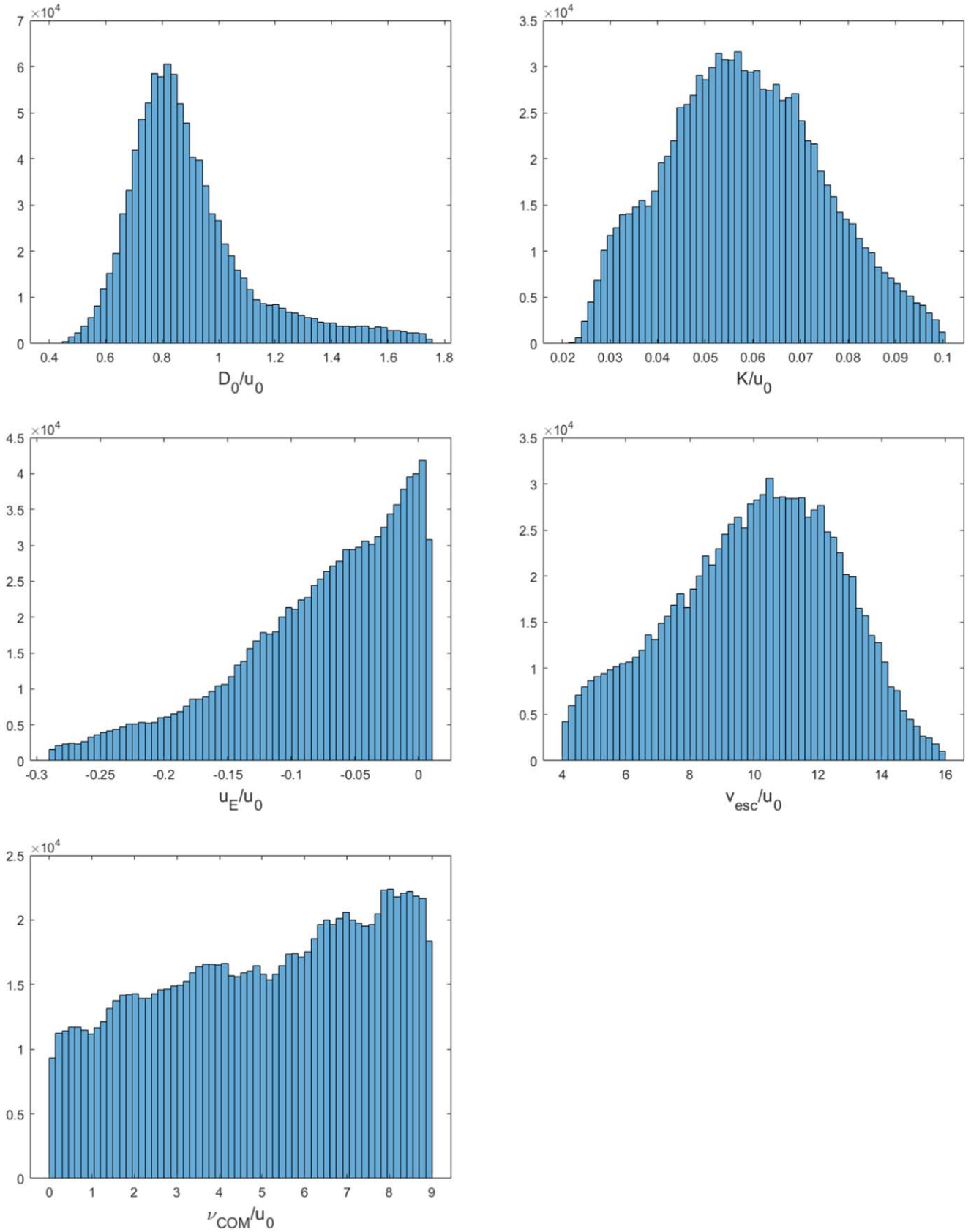

Figure 14. Probability distributions of fitting parameters normalized to the solar wind speed u_0 for various transport coefficients appearing in the analytical solution for SMFR acceleration as generated by the Metropolis–Hastings Algorithm for the 1 May 1980 SMFR acceleration event.

As in the previous event, we note that the escape term is large in comparison to the other transport parameters and that a self-consistent acceleration approach to modeling SMFR acceleration is not needed. Assuming no particle escape ($v_{\rm esc} = 0$), we find that our solution produces a hard accelerated spectrum with a power-law exponent $\alpha = 2.85$ in the high-energy limit based on the fitting parameters listed in Equation (14) ($f(p) \propto p^{-2.85}$), indicating a somewhat steeper spectrum compared to the previous event. Since the hardest possible accelerated spectrum for second-order Fermi acceleration in the high-energy limit is $\alpha = 3$, as discussed above, this is additional confirmation that other SMFR acceleration mechanisms do also contribute to SMFR acceleration. Such a hard spectrum cannot reproduce the observed spectral slopes (see Figure 16; blue lines represent the model without escape, and the "x" symbols represent the observations). When particle escape is retained (red lines in Figure 16), we estimate a substantial increase for α, such that $\alpha = 4.77$, thus generating the much steeper spectra needed for reproducing the observed spectral slopes as shown in Figure 16. This once again emphasizes the prominent role particle escape from the SMFR acceleration region plays in providing a good fit to the observations. As before, we investigated the possibility that some of the spectral steepening should be ascribed to self-consistent SMFR acceleration, by calculating the magnetic field pressure in the SMFRs and the pressure in the energetic particle spectrum. Once again, the pressure in the energetic particle spectrum was calculated to be many orders of magnitude lower than the pressure in the SMFR magnetic fields, thus supporting our test-particle approach to SMFR acceleration —which is simply too inefficient for a self-consistent approach—and ruling out that some of the escape should be attributed to self-consistent acceleration. Finally, the fitting approach again produced a small value for the radial diffusion coefficient (κ). Since efficient SMFR acceleration depends on particles being able to move freely between SMFRs, as discussed above, the large escape term might suggest a way to compensate for the lack of radial diffusion.

5. Individual SMFR Mechanisms of Second-order Fermi Acceleration

As was demonstrated in Section 4, we have determined that second-order Fermi SMFR acceleration is more important than first-order Fermi acceleration produced by the mean SMFR compression rate, as well as acceleration by the mean turbulent motional electric field parallel to the guide/background magnetic field, as it features collectively in the mixed-derivative transport term and the transport term containing the divergence of u_{Er}. It still needs to be determined which of the four basic SMFR acceleration mechanisms (those associated with SMFR compression (superscript "COM"), the component of SMFR shear flow parallel to the SMFR magnetic island field component (superscript "SH"), the parallel component of the non-inertial force associated with the acceleration of the SMFR flow parallel to the SMFR magnetic island field component (superscript "ACC"), and the component of the turbulent motional electric field force parallel to the guide field (superscript "E")) feature predominantly in second-order Fermi acceleration. Another complication is that these four mechanisms manifest themselves in both second-order Fermi acceleration due to energetic particle pitch-angle scattering in mean SMFR fields and in second-order Fermi acceleration due to fluctuations in SMFR fields. We choose to focus on the second-order Fermi associated with fluctuations in the SMFR fields. This is supported by recent PIC simulations of magnetic reconnection that emphasize second-order Fermi acceleration by random fluctuations in parallel electric fields as the main source of electron acceleration on small scales (Che & Zank 2020), and by previous observations in the large-scale solar wind that low-frequency turbulent motional electric fields parallel to the background magnetic field tend to be random (have a small average value; Marsch & Tu 1992). After having averaged over a finite particle speed interval consistent with the range of the observed accelerated particle spectra, the expressions of D_0 for each of the mechanisms are

$$
\begin{aligned}
D_0^{ICOM} &= r_0 \left\langle \frac{D_{pp}^{ICOM}}{p^2} \right\rangle_v = \frac{\sqrt{6c_k}}{15}\left[r_A^I - \frac{(\sigma_c^I)^2}{4}(r_A^I+1)^2\right]\left(\frac{\langle \delta B_I^2\rangle}{B_0^2}\right)^{1/2}\left(\frac{v_{A0}}{v_{\rm max}-v_{\rm min}}\right)\ln\left(\frac{v_{\rm max}}{v_{\rm min}}\right)\frac{v_{A0}r_0}{L_{I\perp}^c},\\
D_0^{ISH} &= r_0 \left\langle \frac{D_{pp}^{ISH}}{p^2} \right\rangle_v = \frac{\sqrt{6c_k}}{4}\left[r_A^I + \frac{41(\sigma_c^I)^2}{40}(r_A^I+1)^2\right]\left(\frac{\langle \delta B_I^2\rangle}{B_0^2}\right)^{5/2}\left(\frac{v_{A0}}{v_{\rm max}-v_{\rm min}}\right)\ln\left(\frac{v_{\rm max}}{v_{\rm min}}\right)\frac{v_{A0}r_0}{L_{I\perp}^c},\\
D_0^{IACC} &= r_0 \left\langle \frac{D_{pp}^{IACC}}{p^2} \right\rangle_v = \frac{\sqrt{6c_k}}{12}\left[r_A^I + \frac{3(\sigma_c^I)^2}{4}(r_A^I+1)^2\right]\left(\frac{\langle \delta B_I^2\rangle}{B_0^2}\right)^{3/2}\left(\frac{(u_0\sin(\psi))^2(v_{\rm max}^2 - v_{\rm min}^2)}{2v_{\rm max}^2 v_{\rm min}^2}\right)\\
&\quad\times\left(\frac{v_{A0}}{v_{\rm max}-v_{\rm min}}\right)\frac{v_{A0}r_0}{L_{I\perp}^c},\\
D_0^{IE} &= r_0 \left\langle \frac{D_{pp}^{IE}}{p^2} \right\rangle_v = \frac{\sqrt{6c_k}}{24}\left[r_A^I - \frac{(\sigma_c^I)^2}{4}(r_A^I+1)^2\right]\left(\frac{\langle \delta B_I^2\rangle}{B_0^2}\right)^{3/2}\left(\frac{Z}{A}\right)^2\left(\frac{L_{I\perp}^c}{d_i}\right)^2\left(\frac{v_{A0}}{v_{\rm max}-v_{\rm min}}\right)\\
&\quad\times\left[\frac{v_{A0}^2(v_{\rm max}^2 - v_{\rm min}^2)}{2v_{\rm max}^2 v_{\rm min}^2} - \left(\frac{v_{A0}}{c}\right)^2\ln\left(\frac{v_{\rm max}}{v_{\rm min}}\right)\right]\frac{v_{A0}r_0}{L_{I\perp}^c},
\end{aligned}
\tag{15}
$$

where $L_{I\parallel}$ is the SMFR length along the guide field $\approx 2L_{I\perp}^c$ (Weygand et al. 2011); $L_{I\perp}^c$ is the average SMFR diameter; γ is the Lorentz factor; v_{A0} is the Alfvén speed due to the guide

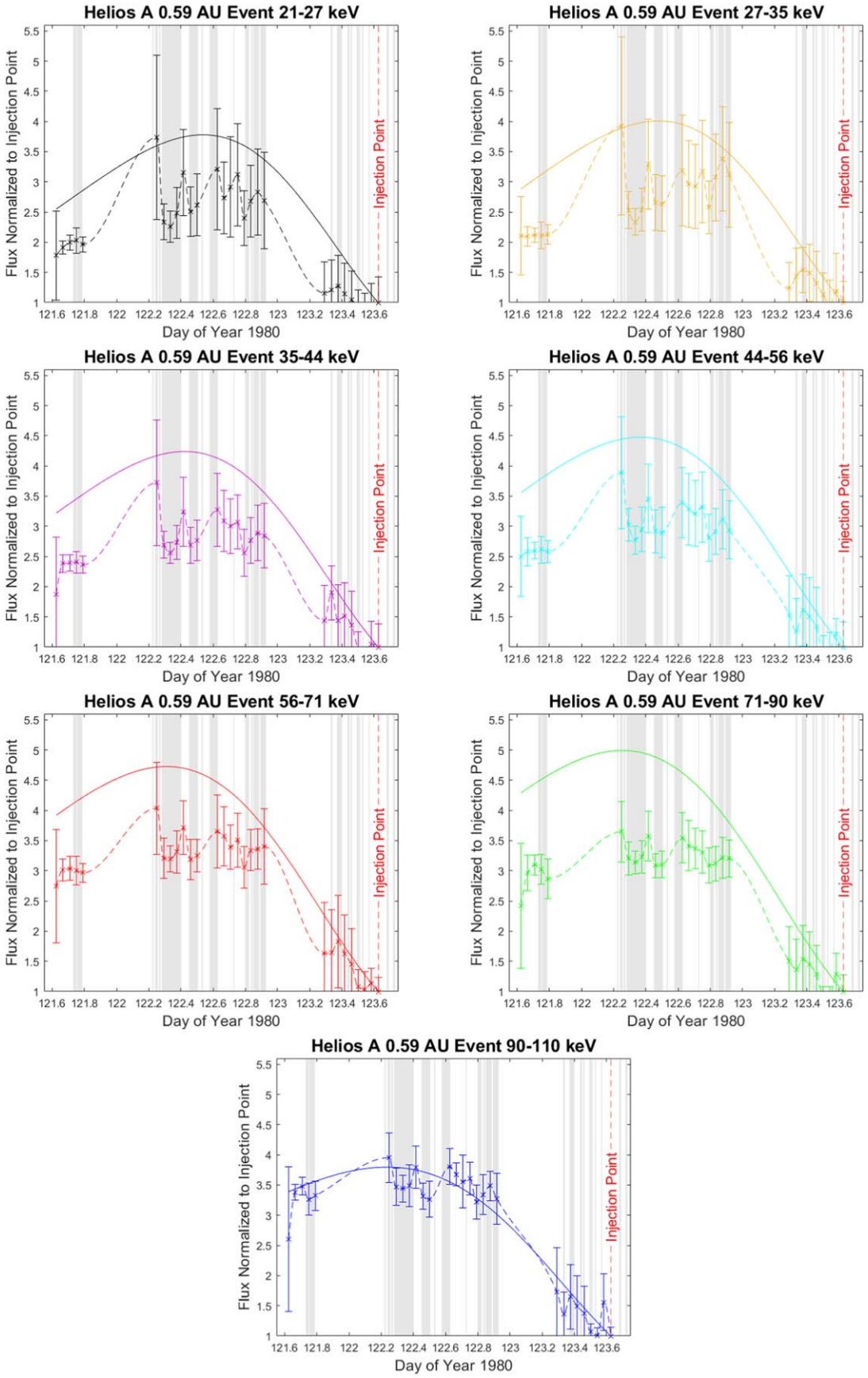

Figure 15. Same format as Figure 11.

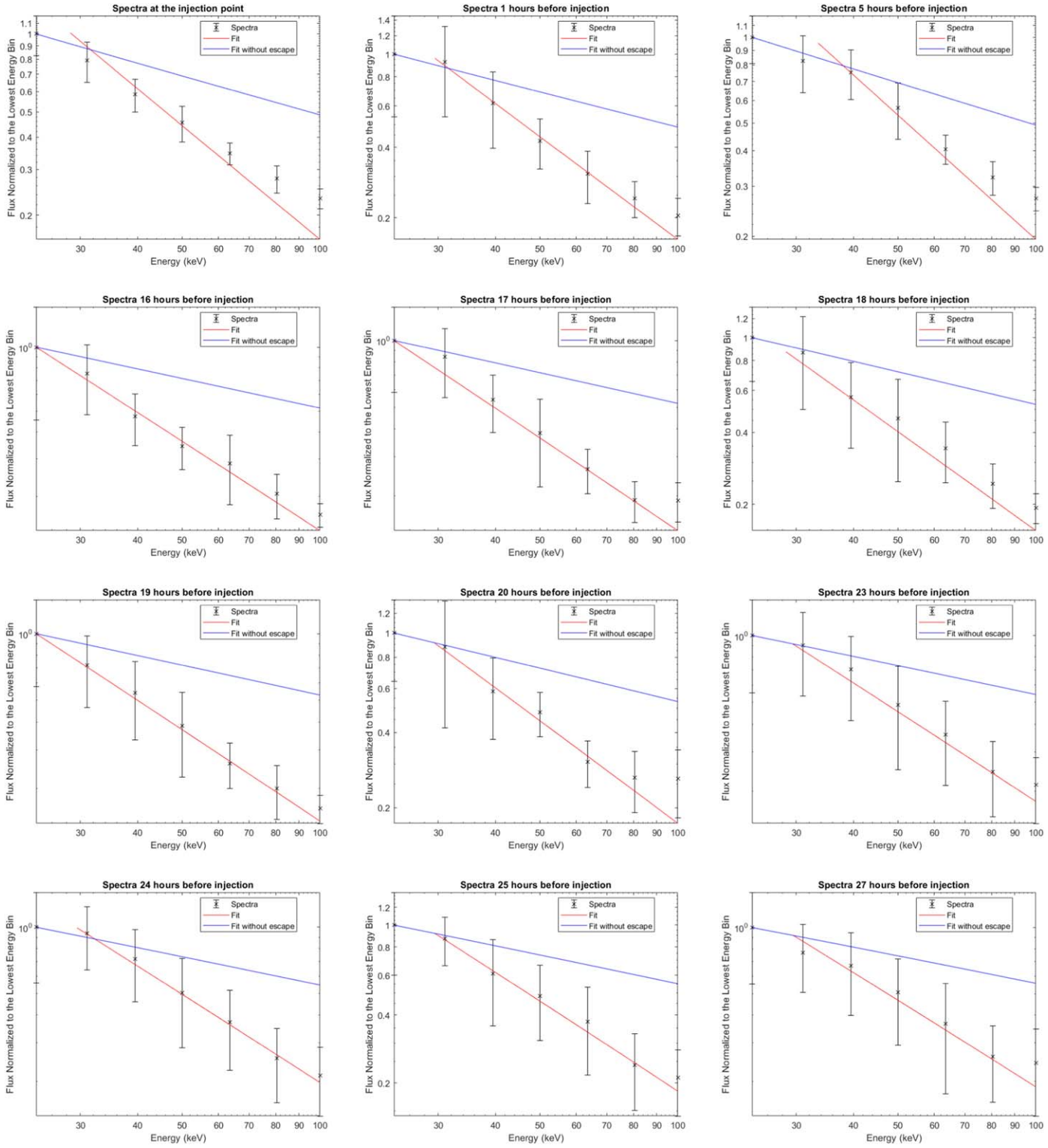

Figure 16. Observed energetic proton spectral flux data ("x" symbols) of the 1 May 1980 SMFR acceleration event at 0.59 au as a function of particle kinetic energy in keV normalized to the flux value of the lowest energy bin. The solid red lines indicate the best fit of the full analytical solution to the data with the aid of the Metropolis–Hastings algorithm, while the blue lines represent the analytical solution without particle escape from the SMFR region.

field; $\langle \delta B_I^2 \rangle$ refers to the average magnetic energy density in the magnetic island (twist) component of SMFRs; B_0^2 is associated with the magnetic energy density in the guide field; d_i is the ion inertial scale, or the gyroradius for the guide field if the particle speed equals the Alfvén speed due to the guide field

$$d_i = r_g(v = v_{A0}) = \frac{m_p v_{A0}}{eB_0} = \frac{m_p}{eB_0}\frac{B_0}{\sqrt{\mu_0 \rho_0}};$$

Table 3
SMFR Mechanism Calculations

Event (Spacecraft Position)		$\tau_{\kappa_\perp^I}$ (hr)	$\tau_{\kappa_\parallel^I}$ (hr)	D_0^{ICOM}/u_0	D_0^{IACC}/u_0	D_0^{ISH}/u_0	D_0^{IE}/u_0	K_0/u_0
1978/4/29	$C_k = 1$	5.002E-3	6.017E-4	5.807E-4	6.647E-8	5.479E-3	1.673	3.537E-3
(0.3 au)	$C_k \neq 1$	4.245E-3	7.180E-4	6.615E-4	7.802E-8	6.472E-3	1.881	3.001E-3
1980/5/1	$C_k = 1$	9.91E-2	1.54E-3	7.44E-4	2.50E-9	3.17E-6	13.24	1.97E-2
(0.59 au)	$C_k \neq 1$	1.40E-1	1.10E-3	5.27E-4	1.71E-9	2.20E-6	9.45	2.78E-2

Note. Calculations were performed using values presented in Table 1 in Equation (15). Individual SMFR events are separated by an added horizontal line.

r_A^I is the Alfvén ratio of the magnetic island component of SMFRs, defined in le Roux et al. (2018) as

$$r_A^I = \frac{\langle \delta u_I^2 \rangle}{\langle \delta v_{AI}^2 \rangle} = \frac{\langle \delta u_I^2 \rangle}{v_{A0}^2} \frac{B_0^2}{\langle \delta B_I^2 \rangle} = \langle \delta u_I^2 \rangle \frac{\mu_0 \rho_0}{\langle \delta B_I^2 \rangle} = \langle \delta u_I^2 \rangle \frac{\mu_0 m_p \langle N_p \rangle}{\langle \delta B_I^2 \rangle};$$

σ_c^I is the normalized cross helicity in the island plane; Z/A is the atomic number over the atomic mass number in AMU; m_p is the rest mass of a proton; $\langle N_p \rangle$ is the average particle density in the SMFR; and $v_{\max}$ and $v_{\min}$ are determined by the energy range over which SMFR acceleration is observed. The c_k term

$$\begin{aligned} c_k &= \frac{\pi}{2} \frac{L_{I\parallel}}{L_{I\perp}^c} \left(\frac{\langle \delta B_I^2 \rangle}{B_0^2} \right)^{1/2} \left(\tau_{\kappa_\parallel^I} \ll \tau_{\kappa_\perp^I} \right), \\ &= 1 \left(\tau_{\kappa_\parallel^I} \leqslant \tau_{\kappa_\perp^I} \right), \end{aligned}$$

is determined by the diffusion timescales parallel to the magnetic field ($\langle \tau_{\kappa_\parallel^I} \rangle_v = L_{I\parallel}^2 / \langle \kappa_\parallel^I \rangle_v$) and perpendicular diffusion timescales ($\langle \tau_{\kappa_\perp^I} \rangle_v = (L_{I\perp}^c)^2 / \langle \kappa_\perp^I \rangle_v$), where

$$\begin{aligned} \langle \kappa_\parallel^I \rangle_v = \frac{5}{6} \frac{L_{I\perp}^c}{\sqrt{6 c_k}} \left(\frac{\langle \delta B_I^2 \rangle}{B_0^2} \right)^{-1/2} \Bigg[v_{\max}^2 \sqrt{1 + r_A^I \left(\frac{v_{A0}}{v_{\max}} \right)^2} - v_{\min}^2 \sqrt{1 + r_A^I \left(\frac{v_{A0}}{v_{\min}} \right)^2} \\ + r_A^I v_{A0}^2 \ln \left[\frac{v_{\max}}{v_{\min}} \frac{1 + \sqrt{1 + r_A^I (v_{A0}/v_{\max})^2}}{1 + \sqrt{1 + r_A^I (v_{A0}/v_{\min})^2}} \right] \Bigg], \end{aligned}$$

$$\langle \kappa_\perp^I \rangle_v = \frac{3 c_k}{20} \left(\frac{\langle \delta B_I^2 \rangle}{B_0^2} \right) \langle \kappa_\parallel^I \rangle_v.$$

Details can be found in Appendix G. Note that these expressions were derived in the strong scattering limit (thus justifying our the assumption of near-isotropic energetic particle distributions) for suprathermal particles ($v_{A0}/v \gg 1$) assuming that random magnetic mirroring forces in SMFRs are the main cause of energetic particle pitch-angle scattering. The fast diffusion limit was imposed ($\tau_{\kappa_\perp} \ll \tau_c = L_{I\perp} / \langle \delta U_I^2 \rangle^{1/2}$, where τ_c is the SMFR turbulence correlation time), thus ensuring that energetic particles efficiently interact with multiple dynamic SMFRs, because our transport theory relies on the idea that efficient SMFR acceleration requires interaction with numerous SMFRs, as suggested by 3D simulations of magnetic reconnection (Dahlin et al. 2017; Che & Zank 2020; Li et al. 2021).

To accurately assess the strength of each mechanism during an SMFR acceleration event period, we calculate an average for each quantity featuring in the expressions listed in Equation (15) above. This is made difficult by the issue of significant gaps in Helios A data. To alleviate this issue, we weight each individual SMFR's parameters by its duration divided by the total duration of the SMFR acceleration event not including the time where measurements are missing. The weighted SMFR parameters are all added together to give an average SMFR parameter for the entire SMFR acceleration event. These calculations are based on parameters determined for each individual SMFR identified with the Grad–Shafranov method (Chen & Hu 2020) during every SMFR acceleration event discussed in this paper (see Table 1 for a complete list of the identified SMFRs including the specified parameters). Even though our transport coefficients were derived in the strong guide field ($B_0 \gg \langle \delta B_I^2 \rangle^{1/2}$), we assume that the transport coefficients are still reasonably accurate when $B_0 \geqslant \langle \delta B_I^2 \rangle^{1/2}$. On this basis, we neglected the contribution of SMFRs for which $B_0 < 2 \langle \delta B_I^2 \rangle^{1/2}$.

Using this method, the values for the calculated values of the separate D_0 mechanisms are reported for two SMFR acceleration events observed at distances less than 1 au from the Sun in Table 3. Comparing the calculated D_0values for each second-order Fermi SMFR acceleration mechanism in Table 3 to the total D_0values for all second-order Fermi SMFR mechanisms needed to fit the full solution (5) to the observed energetic particle fluxes of two SMFR acceleration events with the Metropolis–Hastings algorithm (see the D_0 values presented in Equations (13) and (14)) reveals that only one second-order Fermi mechanism has a D_0value on an order that is at or above that of the total D_0value we obtained from the data fits. This mechanism is the one associated with second-order Fermi acceleration by the variance of the turbulent motional electric field parallel to the guide/background field. A concern arises due to the fact that the D_0-values estimated for this second-order Fermi mechanism are much larger than the total D_0values for second-order Fermi mechanisms obtained with the data fits. This could be explained by the fact that there are significant gaps in the data. If the data gaps do represent time periods without SMFRs and are taken account in the averaging process, this could very well lower the average D_0values for this acceleration mechanism to match up with the total D_0values predicted by the data fits.

6. Summary and Conclusions

le Roux et al. (2019) presented an analytical solution of a Parker transport equation for energetic particle interaction with SMFRs in planar geometry, which unified for the first time all the SMFR acceleration mechanisms present in the equation. The solution is only valid for constant transport coefficients. In this paper, we extended the solution to spherical geometry. This enabled us to study the effect of the radial variation of the transport mechanisms, as well as additional transport mechanisms such as adiabatic energy loss in the radially expanding solar wind flow, on particle acceleration by SMFRs. Our main

goal was to fit the new solution to observed SMFR acceleration events in the inner heliosphere as a vehicle to make the first serious attempt to discover the dominating SMFR acceleration mechanisms in the inner heliosphere, which is still an unsolved problem. Two new events that were identified in Helios A E8 data cannot easily be explained by classical steady-state DSA theory: one of these events occurred when Helios A was near its perihelion (∼0.3 au), and another when Helios A was near 0.59 au. These events were identified as SMFR acceleration events because they overlap with previously identified SMFRs (Chen & Hu 2020) and their flux enhancements match predictions from our transport theory, namely that the associated amplification factor increases with particle energy. They are the first events of their kind to be identified and studied inside a radial distance of 1 au. A Metropolis–Hastings algorithm (Zhao et al. 2019) was employed to determine the best-fit parameters corresponding to each SMFR acceleration mechanism in the full solution (Equation (5)) for modeling the SMFR acceleration events. Combining the results from this effort with results from Grad–Shafranov reconstructions of SMFRs identified in the SMFR acceleration region, we determined that

1. Second-order Fermi SMFR acceleration plays a more important role in energetic particle acceleration by SMFRs than first-order Fermi SMFR acceleration due to the mean SMFR compression rate, as well as acceleration by the mean turbulent motional electric field component parallel to the guide/background magnetic field from the combination of the mixed-derivative transport term with the adiabatic heating term for the presented events, though these secondary mechanisms play a non-negligible role.
2. The second-order Fermi acceleration during these events is dominated by the SMFR mechanism associated with fluctuations in the turbulent motional electric field parallel to the guide/background magnetic field.
3. SMFR acceleration appears to become less efficient with increasing radial distance from the Sun.
4. Particles must be allowed to efficiently escape the SMFR acceleration region in order for observed spectral slopes and spatial profiles to be accurately reproduced.
5. For these events, the energetic particle pressures are too low to have a significant backreaction effect on SMFR structures, thus justifying our test-particle approach to energetic particle acceleration SMFRs.

K.V. acknowledges support from ASGC NASA Grant #80NSSC20M0044 and NASA Grant #80NSSC21K1319. This paper uses data from the Heliospheric Shock Database, generated and maintained at the University of Helsinki. J.l.R. acknowledges support from NASA Grants #80NSSC21K1319, #80NSSC20K1783, and #80NSSC19K0276, as well as NSF EPSCoR RIITrack-1 Cooperative Agreement OIA-1655280. Y.C. acknowledges support from NASA Grants #80NSSC19K0276, #80NSSC21K0003, and #80NSSC21K1763. L.Z. is partially supported by a NASA award #80NSSC20K1783. N.T. acknowledges support from NSF REU grant AGS-1460767. K.V. would also like to thank Dr. Massimillano Bonamente of the University of Alabama in Huntsville for discussions that were instrumental to the implementation of the Metropolis–Hastings algorithm, and Dr. Lan Jian of Goddard Space Flight Center for her assistance with data analysis techniques.

Appendix A
Full Solution

Grouping terms in Equation (4), we see

$$[u_0 - u_E^{Icoh}\cos(\psi) - 3\kappa]\frac{\partial f}{\partial r} - \kappa r\frac{\partial^2 f}{\partial r^2} + \left[-\frac{2u_0}{3} + \frac{\overline{\langle \nu_{\rm COM}^I\rangle}}{3} - \frac{2u_{EA}^{Icoh}\cos(\psi)}{3} - 3D_0\right]\frac{1}{r}\frac{\partial f}{\partial z}$$
$$- \frac{D_0}{r}\frac{\partial^2 f}{\partial z^2} - \frac{2}{3}u_E^{Icoh}\cos(\psi)\frac{\partial^2 f}{\partial r\partial z} + \frac{f v_{\rm esc}}{r} = \frac{dN/dt}{16\pi^2 r_0^2 p_0^3}\delta(r - r_0)\delta(z).$$

Choosing $u_E^{Icoh}\cos(\psi) = u_{Er}$, $\tilde{u} = u_0 - u_{Er}$, and $\bar{u} = u_0 + u_{Er} - \overline{\langle \nu_{\rm COM}^I\rangle}/2$, and dividing through by $-\kappa r$ gives

$$\frac{\partial^2 f}{\partial r^2} - \left[\frac{\tilde{u} - 3\kappa}{\kappa}\right]\frac{1}{r}\frac{\partial f}{\partial r} - \left[\frac{-2\bar{u}/3 - 3D_0}{\kappa}\right]\frac{1}{r^2}\frac{\partial f}{\partial z} + \frac{D_0}{\kappa r^2}\frac{\partial^2 f}{\partial z^2} + \frac{2u_{Er}}{3\kappa r}\frac{\partial^2 f}{\partial r\partial z}$$
$$- \frac{f v_{\rm esc}}{\kappa r^2} = -\frac{dN/dt}{16\pi^2\kappa r_0^3 p_0^3}\delta(r - r_0)\delta(z). \tag{A1}$$

Next, we apply the Laplace transform to Equation (A1) ($\overline{f}(r, \mu) = \int_0^\infty dz e^{-z\mu} f(r, z)$). By assumption, the transport coefficients in Equation (A1) (i.e., u_0, D_0, u_{Er}, κ, $v_{\rm esc}$, and $\overline{\langle \nu_{\rm COM}^I\rangle}$) are all independent of z. Similarly, because $z = 0$ means $p = p_0$ and we are only interested in particles where $p > p_0$, we ignore terms where $z = 0$. After applying the transform, Equation (A1) becomes

$$\frac{\partial^2 \overline{f}}{\partial r^2} - \left[\frac{\tilde{u} - 2u_{Er}/3 - 3\kappa}{\kappa}\right]\frac{1}{r}\frac{\partial \overline{f}}{\partial r} + \left[\frac{2\bar{u}\mu/3 + D_0(3 + \mu)\mu - v_{\rm esc}}{\kappa}\right]\frac{1}{r^2}\overline{f} = -\frac{dN/dt}{16\pi^2\kappa r_0^3 p_0^3}\delta(r - r_0). \tag{A2}$$

To solve Equation (A2), we first solve the homogeneous equation. For this purpose, we compare the homogeneous equation with (5.2.30) from Morse & Feshbach (1953):

$$\frac{d^2\psi}{dz^2} - \left(\frac{\lambda_1 + \lambda_2 - 1}{z}\right)\frac{d\psi}{dz} + \left(\frac{\lambda_1\lambda_2}{z^2}\right)\psi = 0,$$

whereby we get $\lambda_1 + \lambda_2 = \tilde{u}/\kappa - 2u_{Er}\mu/3\kappa - 2$ and $\lambda_1\lambda_2 = 2\bar{u}\mu/3\kappa + D_0(3 + \mu)\mu/\kappa - v_{\rm esc}/\kappa$. Considering that $(\lambda - \lambda_1)(\lambda - \lambda_2) = \lambda^2 - (\lambda_1 + \lambda_2)\lambda + \lambda_1\lambda_2 = 0$, it can then be rearranged to show

$$\lambda_\pm = \frac{1}{2}(\lambda_1 + \lambda_2) \pm \frac{1}{2}\sqrt{(\lambda_1 + \lambda_2)^2 - 4\lambda_1\lambda_2} = \frac{1}{2}(\lambda_1 + \lambda_2) \pm \sqrt{\frac{1}{4}(\lambda_1 + \lambda_2)^2 - \lambda_1\lambda_2}.$$

Inspection of the expressions for λ_+ and λ_- shows that $\lambda_+ = \lambda_1$ and $\lambda_- = \lambda_2$. Therefore, going forward we define $\lambda_+ = \lambda_1$ and $\lambda_- = \lambda_2$. It can then be shown that the term inside the square root is

$$\frac{1}{4}(\lambda_1 + \lambda_2)^2 - \lambda_1\lambda_2 = \left(1 - \frac{\tilde{u}}{2\kappa}\right)^2 + \frac{v_{\rm esc}}{\kappa} + \mu^2\overbrace{\left(\frac{u_{Er}^2}{9\kappa^2} - \frac{D_0}{\kappa}\right)}^{A} + \mu\underbrace{\left(\frac{2u_{Er}}{3\kappa}\left(1 - \frac{\tilde{u}}{2\kappa}\right) - \frac{2\bar{u}}{3\kappa} - \frac{3D_0}{\kappa}\right)}_{B}.$$

The solution to the homogeneous version of Equation (A2) can be expressed as $\overline{f} = C_+ r^{\lambda_+} + C_- r^{\lambda_-}$, where C_+ and C_- are constants. We complete the square inside the square root to simplify the algebraic steps that follow. In general, $A\mu^2 + B\mu = A(\mu + B/2A)^2 - B^2/4A$, and we get

$$\lambda_\pm = \overbrace{-\left(1 - \frac{\tilde{u}}{2\kappa}\right) - \frac{u_{Er}}{3\kappa}\mu}^{a} \pm \sqrt{\underbrace{\left(1 - \frac{\tilde{u}}{2\kappa}\right)^2 + \frac{v_{\rm esc}}{\kappa} - \frac{B^2}{4A}}_{b^2} - \underbrace{A^*\left(\mu + \frac{B}{2A}\right)^2}_{\xi^2}} = a \pm \sqrt{b^2 - \xi^2}, \tag{A3}$$

where $A = -A^*$, $B/2A = (3 - (1/3D_0)[u_{Er}(1 - \tilde{u}/2\kappa) - 2\bar{u}])/2(1 - u_{Er}^2/9\kappa D_0)$ and $B^2/4 = -D_0(3 - (1/3D_0)[u_{Er}(1 - \tilde{u}/2\kappa) - 2\bar{u}])^2/4\kappa(1 - u_{Er}^2/9\kappa D_0)$. We define $f_1(r) = r^{\lambda_+}$ and $f_2(r) = r^{\lambda_-}$, noting that $\lambda_+ > 0$ if $a < |\sqrt{b^2 - \xi^2}|$ and $\lambda_- < 0$ when $a < |\sqrt{b^2 - \xi^2}|$.

Following Morse & Feshbach (1953), we apply the method of variation of parameters to get a solution to the inhomogeneous Equation (A2):

$$\overline{f} = f_1(r)\left[C_+ - \int_a^r \frac{f_2(r')Q(r')}{W(r')}dr'\right] + f_2(r)\left[C_- + \int_a^r \frac{f_1(r')Q(r')}{W(r')}dr'\right],$$

where $Q(r) = -dN/dt\delta(r - r_0)/16\pi^2\kappa r_0^3 p_0^2$ and $W(r')$ is the Wronskian. To avoid unbounded solutions, we require $C_+ - \int_a^r dr' f_2(r')Q(r')/W(r') \to 0$ as $r \to \infty$. This gives us $C_+ = \int_a^\infty dr' f_2(r')Q(r')/W(r')$. Plugging this in gives

$$C_+ - \int_a^r \frac{f_2(r')Q(r')}{W(r')}dr' = \int_r^\infty \frac{f_2(r')Q(r')}{W(r')}dr',$$

which is allowed because Q, f_2, and W are all symmetric functions. By following the same process, it is easy to see $C_- + \int_a^r dr' f_1(r')Q(r')W(r') = \int_0^r dr' f_1(r')Q(r')/W(r')$. Applying these results,

$$\overline{f} = f_1(r)\left[\int_r^\infty \frac{f_2(r')Q(r')}{W(r')}dr'\right] + f_2(r)\left[\int_0^r \frac{f_1(r')Q(r')}{W(r')}dr'\right]. \tag{A4}$$

The integrals are now evaluated, whereby

$$\begin{aligned}\int_r^\infty \frac{f_2(r')Q(r')}{W(r')}dr' &= -\int_r^\infty \frac{r'^{\lambda_-}}{(\lambda_- - \lambda_+)} r'^{1-\lambda_+-\lambda_-}\frac{N\delta(r' - r_0)}{16\pi^2\kappa r_0^3 p_0^2}dr' \\ &= -\frac{N}{16\pi^2\kappa r_0^2 p_0^2(\lambda_- - \lambda_+)} r_0^{-\lambda_+}[1 - H(r - r_0)],\end{aligned}$$

where $H(r - r_0)$ is a step function at $r = r_0$. Following the same process results in

$$\int_0^r \frac{f_1(r')Q(r')}{W(r')}dr' = -\frac{dN/dt}{16\pi^2\kappa r_0^2 p_0^3(\lambda_- - \lambda_+)} r_0^{-\lambda_-} H(r - r_0).$$

After incorporating these results into Equation (A4):

$$\overline{f} = \frac{dN/dt}{32\pi^2\kappa r_0^2 p_0^3\sqrt{b^2 - \xi^2}}\left(\frac{r}{r_0}\right)^{\bar{a}}\left[\left(\frac{r}{r_0}\right)^{\mu\tilde{a}+\sqrt{b^2-\xi^2}}[1 - H(r - r_0)] + \left(\frac{r}{r_0}\right)^{\mu\tilde{a}-\sqrt{b^2-\xi^2}} H(r - r_0)\right]. \tag{A5}$$

Note that $(\lambda_- - \lambda_+) = a - \sqrt{b^2 - \xi^2} - a - \sqrt{b^2 - \xi^2} = -2\sqrt{b^2 - \xi^2}$ and $a = \bar{a} + \mu\tilde{a}$. To get the final result, the inverse Laplace transform is introduced ($f = (1/2\pi i)\int_{C-i\infty}^{C+i\infty} d\mu e^{\mu z}\overline{f}$). It is helpful to reshape the inverse Laplace transform into a Fourier cosine transform. For this purpose, the new variable $\tilde{\mu} = i\xi$ is introduced. Ignoring terms that are constant in terms of μ, we get

$$\begin{aligned}\int_{C-i\infty}^{C+i\infty}\left(\frac{r}{r_0}\right)^{\mu\tilde{a}+\sqrt{b^2-\xi^2}} e^{\mu z}\frac{1}{\sqrt{b^2 - \xi^2}}d\mu &= \frac{2i}{\sqrt{A^*}}\exp\left[-\frac{B}{2A}(z + \tilde{a}\ln(r/r_0)\right] \\ \times \int_0^\infty \left(\frac{r}{r_0}\right)^{\sqrt{b^2-\xi^2}} \frac{1}{\sqrt{b^2 - \xi^2}}\cos\left(\frac{\tilde{\mu}}{\sqrt{A^*}}(z + \tilde{a}\ln(r/r_0)\right)d\tilde{\mu}.\end{aligned}$$

To get the above expression, we applied $(r/r_0)^{-x} = \exp[-x\ln(r/r_0)]$ and $\exp[-iax] = \cos(-ax) + i\sin(-ax)$, and eliminated the integral with an odd integrand. After evaluating the remaining integral using the Fourier cosine transform #27 on p. 17 from Erdélyi (1954), we get

$$\begin{aligned}\int_{C-i\infty}^{C+i\infty}\left(\frac{r}{r_0}\right)^{\mu\tilde{a}+\sqrt{b^2-\xi^2}} e^{\mu z}\frac{1}{\sqrt{b^2 - \xi^2}}d\mu &= \frac{2i}{\sqrt{A^*}}\exp\left[-\frac{B}{2A}(z + \tilde{a}\ln(r/r_0)\right] \\ \times K_0\left[b\sqrt{(\ln(r_0/r))^2 + \frac{1}{A^*}(z + \tilde{a}\ln(r/r_0))^2}\right],\end{aligned}$$

where K_0 is the zeroth modified Bessel function of the second kind. Following the same steps, it can be shown

$$\int_{C-i\infty}^{C+i\infty}\left(\frac{r}{r_0}\right)^{\mu\tilde{a}-\sqrt{b^2-\xi^2}}e^{\mu z}\frac{1}{\sqrt{b^2-\xi^2}}d\mu=\frac{2i}{\sqrt{A^*}}\exp\left[-\frac{B}{2A}(z+\tilde{a}\ln(r/r_0)\right]\times K_0\left[b\sqrt{(\ln(r/r_0))^2+\frac{1}{A^*}(z+\tilde{a}\ln(r/r_0))^2}\right].$$

Applying these results to the inverse Laplace transform of Equation (A5) results in

$$f(r,p)=\frac{dN/dt}{32\pi^3\kappa r_0^2p_0^3\sqrt{A^*}}\left(\frac{r}{r_0}\right)^{\bar{a}-\frac{B}{2A}\tilde{a}}\left(\frac{p}{p_0}\right)^{-\frac{B}{2A}}\left(K_0\left[b\sqrt{(\ln(r_0/r))^2-\frac{1}{A}(\ln(p/p_0)+\tilde{a}\ln(r/r_0))^2}\right]\times[1-H(r-r_0)]+K_0\left[b\sqrt{(\ln(r/r_0))^2-\frac{1}{A}(\ln(p/p_0)+\tilde{a}\ln(r/r_0))^2}\right]H(r-r_0)\right).$$

The two terms of the solution can be unified into a single expression whereby the step functions can be discarded

$$f(r,p)=\frac{dN/dt}{32\pi^3\kappa r_0^2p_0^3\sqrt{A^*}}\left(\frac{r}{r_0}\right)^{\bar{a}-\frac{B}{2A}\tilde{a}}\left(\frac{p}{p_0}\right)^{-\frac{B}{2A}}\times K_0\left[b\sqrt{(\ln(r/r_0))^2+\frac{1}{A^*}(\ln(p/p_0)+\tilde{a}\ln(r/r_0))^2}\right]. \tag{A6}$$

The terms in the solution are

$$b=\sqrt{\left(1-\frac{(u_0-u_{Er})}{2\kappa}\right)^2+\frac{v_{\rm esc}}{\kappa}+\frac{D_0}{4\kappa}\frac{(3-(1/3D_0)[\overline{\langle\nu^I_{\rm COM}\rangle}-u_{Er}u_0/\kappa+u_{Er}^2/\kappa-2u_0])^2}{(1-u_{Er}^2/9\kappa D_0)}}, \tag{A7}$$

$$\frac{B}{2A}=\frac{1}{2}\frac{(3-(1/3D_0)[\overline{\langle\nu^I_{\rm COM}\rangle}-u_{Er}u_0/\kappa+u_{Er}^2/\kappa-2u_0])}{(1-u_{Er}^2/9\kappa D_0)}, \tag{A8}$$

$$A^*=\frac{D_0}{\kappa}\left(1-\frac{u_{Er}^2}{9\kappa D_0}\right), \tag{A9}$$

$$\bar{a}=-\left(1-\frac{u_0-u_{Er}}{2\kappa}\right), \tag{A10}$$

$$\tilde{a}=-\frac{u_{Er}}{3\kappa}. \tag{A11}$$

Appendix B
High-energy Limit

Here, we use the large-argument limit of the modified Bessel function of the second kind, $K_0(w)\sim\sqrt{\pi/2w}e^{-w}$, $|w|\gg1$, as a consequence of assuming that the momentum is much greater than the injection momentum, $p/p_0\gg1$, and requiring that $r/r_0>1$. Applying this to Equation (A6) yields

$$f(r,p)=\frac{dN/dt}{32\pi^3\kappa r_0^2p_0^3}\sqrt{\frac{\pi}{2}}\,(b\sqrt{A^*}\ln(p/p_0))^{-1/2}\left(\frac{r}{r_0}\right)^{\bar{a}-\tilde{a}B/2A}\left(\frac{p}{p_0}\right)^{-B/2A-b/\sqrt{A^*}}. \tag{B1}$$

Analysis of the r/r_0 exponent shows that it is clearly positive. Thus, for increasing radial distances $r>r_0$, sufficiently close to $r=r_0$, the particle distribution function increases. The exponent of r/r_0 can be written as

$$\bar{a}-\tilde{a}\frac{B}{2A}=-1+\frac{-\overline{\langle\nu^I_{\rm COM}\rangle}+2u_0}{2u_{Er}}\left[\frac{1}{1-u_{Er}^2/9\kappa D_0}-1\right]+\frac{u_0}{2\kappa}\left[\frac{1}{1-u_{Er}^2/9\kappa D_0}\right].$$

Applying the constraint $0 < 1 - u_{Er}^2/9\kappa D_0 < 1$ means that the -1 in the second term is dominated by the positive term with $1 - u_{Er}^2/9\kappa D_0$ in the denominator.

Appendix C
Large Radial Distance Limit

In this limit, we assume that the radial position, r, is much greater than the injection position $r/r_0 \gg 1$, $p/p_0 > 1$, and apply the large-argument limit to the modified Bessel function of the second kind. Applying these assumptions to Equation (A6) gives

$$f(r,p) = \frac{dN/dt}{32\pi^3\kappa r_0^2 p_0^3}\sqrt{\frac{\pi}{2}}\left(b\sqrt{D_0 A^*/\kappa}\,\ln(r/r_0)\right)^{-1/2}\left(\frac{r}{r_0}\right)^{\bar{a}-\tilde{a}B/2A-b\sqrt{D_0/\kappa A^*}}\left(\frac{p}{p_0}\right)^{-B/2A}. \tag{C1}$$

Upon examining terms, it is clear that $b > 0$ and real if $9D_0\kappa > u_{Er}^2$, whereby the final term in the exponent of r/r_0 has a negative contribution to the exponent as a whole. Defining $q = (3 - 1/3D_0[\overline{\langle\nu_{\rm COM}^I\rangle} - u_{Er}u_0/\kappa + u_{Er}^2/\kappa - 2u_0])$, we see that the exponent of r/r_0 can be rewritten as

$$\bar{a} - \tilde{a}\frac{B}{2A} - b\sqrt{\frac{D_0}{\kappa A^*}} = -\left(1 - \frac{u_0 - u_{Er}}{2\kappa}\right) + \frac{u_{Er}}{6\kappa}\frac{\kappa}{D_0}\frac{q}{A^*} - \sqrt{\frac{1}{(1 - u_{Er}^2/9\kappa D_0)}}$$
$$\times\sqrt{\left[-\left(1 - \frac{(u_0 - u_{Er})}{2\kappa}\right) + \sqrt{\frac{D_0}{4\kappa}}\frac{\kappa q}{D_0 A^*}\right]^2 + \frac{v_{\rm esc}}{\kappa} - 2\left(1 - \frac{(u_0 - u_{Er})}{2\kappa}\right)\sqrt{\frac{D_0}{4\kappa}}\frac{\kappa q}{D_0 A^*}}.$$

Examining the terms including q/A^*, and assuming that $A^* > 0 \Rightarrow \sqrt{D_0/4\kappa} > |u_{Er}|/6\kappa$, we thus conclude that the term under the square root is larger in magnitude than the term outside the square root. Then, if $q > 0$ and $u_{Er} < 0$, the whole exponent is negative, but if we allow $q < 0$, then the individual terms need to be examined to determine the sign of the exponent. From the condition above, we know $\sqrt{D_0/4\kappa} > |u_{Er}|/6\kappa$. This can be expressed as

$$G = -\left(1 - \frac{u_0 - u_{Er}}{2\kappa}\right) + \frac{u_{Er}}{6\kappa}\frac{\kappa}{D_0}\frac{q}{A^*} < -\left(1 - \frac{(u_0 - u_{Er})}{2\kappa}\right) + \sqrt{\frac{D_0}{4\kappa}}\frac{\kappa q}{D_0 A^*} = F,$$

and in general, if we take three numbers (F, G, and M) that obey $F > G$ and $M > 0$, then it must follow that $\sqrt{F^2 + M} > G$. Therefore, if

$$M = \frac{v_{\rm esc}}{\kappa} - 2\left(1 - \frac{(u_0 - u_{Er})}{2\kappa}\right)\sqrt{\frac{D_0}{4\kappa}}\frac{\kappa q}{D_0 A^*} > 0,$$

the distribution function decreases with increasing radial distance in the large radial distance limit.

Appendix D
Second-order Fermi Limit

The second-order Fermi acceleration limit is obtained by letting $u_{Er} \to 0$ and $\overline{\langle\nu_{\rm COM}^I\rangle} \to 0$ in the complete solution given by Equation (A6). This yields

$$f(r,p) = \frac{dN/dt}{32\pi^3 r_0^2 p_0^3\sqrt{\kappa D_0}}\left(\frac{r}{r_0}\right)^{-(1-u_0/2\kappa)}\left(\frac{p}{p_0}\right)^{-3/2(1+2u_0/9D_0)} K_0[b^*\sqrt{(\ln(r/r_0))^2 + \kappa z^2/D_0}], \tag{D1}$$

where

$$b^* = \sqrt{1 + \left(\frac{u_0}{2\kappa}\right)^2 + \frac{v_{\rm esc}}{\kappa} + \frac{9D_0}{4\kappa} + \frac{u_0^2}{9D_0\kappa}}.$$

In the limit of strong second-order Fermi acceleration ($D_0 \gg 1$), we can simplify the argument of the modified Bessel function before taking its large-argument limit. Then, solution (D1) simplifies to

$$f(r,p) = \frac{dN/dt}{32\pi^3 r_0^2 p_0^3\sqrt{D_0}}\sqrt{\frac{\pi}{3\sqrt{D_0\kappa}\,\ln(r/r_0)}}\left(\frac{r}{r_0}\right)^{-(1-u_0/2\kappa)-3/2\sqrt{D_0/\kappa}}\left(\frac{p}{p_0}\right)^{-3/2}, \tag{D2}$$

which yields the hardest possible power law in momentum with an exponent of $-3/2$. Note that taking the strong acceleration limit close to the particle source ($r \rightarrow r_0$) produces a softer power law with exponent -3 because then

$$f(r, p) = \frac{dN/dt}{32\pi^3 r_0^2 p_0^3 \sqrt{D_0 \kappa}} \sqrt{\frac{\pi}{3\ln(p/p_0)}} \left(\frac{r}{r_0}\right)^{-(1-u_0/2\kappa)} \left(\frac{p}{p_0}\right)^{-3}. \tag{D3}$$

This yields that the accelerated particle spectrum tends to becomes harder with increasing radial distance upstream of the particle injection position ($r = r_0$) as particles with different energies diffuse in the direction of the solar wind flow.

Appendix E
Limit of Acceleration by the Mean Turbulent Motional Electric Field Parallel to Guide/Background Magnetic Field

E.1. Solution from the Parker Equation

Going back to (A1), ignoring terms containing $\overline{\langle \nu^I_{\rm COM} \rangle}$ and D_0, and assuming that $u_{Er} = -|u_{Er}| < 0$ (defining $|u_{Er}| = u^*_{Er}$), we get

$$\frac{\partial^2 f}{\partial r^2} - \left[\frac{u_0 + u^*_{Er} - 3\kappa}{\kappa}\right]\frac{1}{r}\frac{\partial f}{\partial r} + \left[\frac{2/3(u_0 - u^*_{Er})}{\kappa}\right]\frac{1}{r^2}\frac{\partial f}{\partial z} - \frac{2u^*_{Er}}{3\kappa r}\frac{\partial^2 f}{\partial r \partial z} - \frac{f\nu_{\rm esc}}{\kappa r^2} = -\frac{dN/dt}{16\pi^2 \kappa r_0^3 p_0^3}\delta(r - r_0)\delta(z). \tag{E1}$$

Applying the Laplace transform to (E1) as before gives

$$\frac{\partial^2 \overline{f}}{\partial r^2} - \left[\frac{u_0 + u^*_{Er} - 3\kappa + 2u^*_{Er}\mu/3}{\kappa}\right]\frac{1}{r}\frac{\partial \overline{f}}{\partial r} + \left[\frac{2\mu/3(u_0 - u^*_{Er}) - \nu_{\rm esc}}{\kappa}\right]\frac{1}{r^2}\overline{f} = -\frac{dN/dt}{16\pi^2 \kappa r_0^3 p_0^3}\delta(r - r_0)\delta(z).$$

As was done above, we apply the approach by Morse & Feshbach (1953) to solve this second-order partial differential equation containing the effects of spherical geometry. We find that

$$\lambda_\pm = -\left(1 - \frac{u_0 + u^*_{Er}}{2\kappa}\right) + \frac{u^*_{Er}\mu}{3\kappa} \pm \sqrt{\left[-\left(1 - \frac{u_0 + u^*_{Er}}{2\kappa}\right) + \frac{u^*_{Er}\mu}{3\kappa}\right]^2 + \frac{\nu_{\rm esc}}{\kappa} - \frac{2\mu}{3\kappa}(u_0 - u^*_{Er})}.$$

The argument of the square root can be rewritten as

$$\underbrace{\left(1 - \frac{u_0}{u^*_{Er}}\right)\left(1 + \frac{u_0}{u^*_{Er}} - \frac{u_0 + u^*_{Er}}{\kappa}\right) + \frac{\nu_{\rm esc}}{\kappa}}_{\nu^2} + \underbrace{\left(\frac{u^*_{Er}}{3\kappa}\right)^2\left[\mu - \frac{3\kappa}{u^*_{Er}}\left(\frac{u_0}{u^*_{Er}} - \frac{u_0 + u^*_{Er}}{2\kappa}\right)\right]^2}_{\varepsilon^2}.$$

The method of variation of parameters is applied to produce the solution:

$$\overline{f} = \frac{dN/dt}{32\pi^2 \kappa r_0^2 p_0^3 \sqrt{\nu^2 + \varepsilon^2}}\left(\frac{r}{r_0}\right)^{-(1-(u_0+u^*_{Er})/2\kappa)+\mu u^*_{Er}/3\kappa} \times \left[\left(\frac{r}{r_0}\right)^{\sqrt{\nu^2+\varepsilon^2}}[1 - H(r - r_0)] + \left(\frac{r}{r_0}\right)^{-\sqrt{\nu^2+\varepsilon^2}} H(r - r_0)\right].$$

Consider the inverse Laplace transform of the solution for $\overline{f}$ after introducing the new variable $\mu = 3\kappa/u^*_{Er}[\varepsilon + (u_0/u^*_{Er} - (u_0 + u^*_{Er})/2\kappa)]$. After evaluating this inverse transform with the aid of the inverse Laplace transform (24) listed on page 248 of Erdélyi (1954), we finally get

$$f(r, p) = \frac{3dN/dt}{32\pi^2 r_0^2 p_0^3 u^*_{Er}}\left(\frac{r}{r_0}\right)^{-(1-u_0/u^*_{Er})}\left(\frac{p}{p_0}\right)^{3\kappa/u^*_{Er}(u_0/u^*_{Er} - (u_0+u^*_{Er})/2\kappa)} \times J_0\left(\nu\left(\frac{3\kappa}{u^*_{Er}}\right)\sqrt{z}\sqrt{z + \frac{2u^*_{Er}}{3\kappa}\ln(r/r_0)}\right)\left[H\left(\frac{3\kappa z}{u^*_{Er}} + 2\ln(r/r_0)\right)[1 - H(r - r_0)] + H(r - r_0)\right], \tag{E2}$$

where J_0 is the Bessel function of the first kind and $\nu = \sqrt{(1 - u_0/u^*_{Er})(1 + u_0/u^*_{Er} - (u_0 + u^*_{Er})/\kappa) + \nu_{\rm esc}/\kappa}$. The oscillatory nature of the solution generated by the presence of J_0, which can cause f_0 to become negative, can be removed if we assume that ν is imaginary. We now have two options. One possibility is that $(1 - u_0/u^*_{Er}) < 0$ and $(1 + u_0/u^*_{Er} - (u_0 + u^*_{Er})/\kappa) > 0$. Since this

approach yields a modified Bessel function of the first kind I_0 that increases with radial distance, the desired peak in the particle distribution can only be achieved if the exponent of r/r_0 is negative—which is not the case. Thus, we choose the remaining option, where $(1 - u_0/u_{Er}^*) > 0$ and $(1 + u_0/u_{Er}^* - (u_0 + u_{Er}^*)/\kappa) < 0$. The first inequality indicates that $u_{Er}^* > u_0$. The second is a bit more more difficult to interpret, but reveals that $\kappa < u_{Er}^*$. For ν to be imaginary, the first term in the expression for ν must be more important than the second term $v_{\rm esc}/\kappa$. This follows by imposing the additional requirement that $u_{Er}^* > v_{\rm esc}$. More simply, ν will become imaginary by taking the large u_{Er}^* limit. When ν is imaginary, we can apply $I_\nu(z) = e^{\mp(i\nu\pi/2)}J_\nu(ze^{\pm}(i\pi/2))$. Using the Euler relations $e^{\mp(i\pi/2)} = \cos((\pi/2)) \mp i\sin((\pi/2)) = \mp i$ and defining $\nu = -i^2\nu = -i\nu^*$, where $\nu^* = i\nu$, we get

$$f(r,p) = \frac{3dN/dt}{32\pi^2 u_{Er}^* r_0^2 p_0^3}\left(\frac{r}{r_0}\right)^{-(1-u_0/u_{Er}^*)}\left(\frac{p}{p_0}\right)^{3\kappa/u_{Er}^*(u_0/u_{Er}^* - (u_0+u_{Er}^*)/2\kappa)} \times I_0\left[\nu^*\left(\frac{3\kappa}{u_{Er}^*}\right)\sqrt{z}\sqrt{z + \frac{2u_{Er}^*}{3\kappa}\ln(r/r_0)}\right]\left[\left[1 - H(r-r_0)\right]H\left(\frac{3\kappa}{u_{Er}^*}z + 2\ln(r/r_0)\right) + H(r-r_0)\right], \tag{E3}$$

where $\nu^* = \sqrt{-(1 - u_0/u_{Er}^*)(1 + u_0/u_{Er}^* - (u_0 + u_{Er}^*)/\kappa) - v_{\rm esc}/\kappa}$.

E.1.1. Limit from the Full Solution

Starting with (A6) (the full solution containing all the acceleration mechanisms), we investigate what approach we need to follow to recover (E2). To start, we assume that $\overline{\langle \nu_{\rm COM}^I \rangle} \to 0$, $D_0 \to 0$, and $u_{Er} = -u_{Er}^*$, whereby

$$\frac{D_0}{4\kappa}\frac{(3 - (1/3D_0)[\overline{\langle \nu_{\rm COM}^I \rangle} - u_{Er}u_0/\kappa + u_{Er}^2/\kappa - 2u_0])^2}{(1 - u_{Er}^2/9\kappa D_0)} = -\left(\frac{(u_0 + u_{Er}^*)}{2\kappa} - \frac{u_0}{u_{Er}^*}\right)^2.$$

Then b simplifies to

$$b = \sqrt{\left(1 - \frac{(u_0 - u_{Er})}{2\kappa}\right)^2 + \frac{v_{\rm esc}}{\kappa} - \left(\frac{(u_0 + u_{Er}^*)}{2\kappa} - \frac{u_0}{u_{Er}^*}\right)^2} = \sqrt{\left(1 - \frac{u_0}{u_{Er}}\right)\left(1 + \frac{u_0}{u_{Er}} - \frac{(u_0 + u_{Er}^*)}{\kappa}\right) + \frac{v_{\rm esc}}{\kappa}} = \nu.$$

By applying the limit $D_0 \to 0$, the expression for $A^* = D_0/\kappa - u_{Er}^{*2}/9\kappa^2 \to -u_{Er}^{*2}/9\kappa^2$. Following the same assumptions,

$$\frac{1}{2}\frac{(3 - (1/3D_0)[\overline{\langle \nu_{\rm COM}^I \rangle} - u_{Er}u_0/\kappa + u_{Er}^2/\kappa - 2u_0])}{(1 - u_{Er}^2/9\kappa D_0)} = \frac{3}{2} - \frac{1}{6}\frac{u_{Er}^*u_0/\kappa - 2u_0}{-u_{Er}^{*2}/9\kappa} = \left(\frac{3\kappa}{u_{Er}^*}\right)\left(\frac{u_0 + u_{Er}^*}{2\kappa} - \frac{u_0}{u_{Er}^*}\right).$$

Therefore, the exponent of r/r_0 becomes

$$\bar{a} - \tilde{a}\frac{B}{2A} = -\left(1 - \frac{u_0 + u_{Er}^*}{2\kappa}\right) - \left(\frac{u_0 + u_{Er}^*}{2\kappa} - \frac{u_0}{u_{Er}^*}\right) = -\left(1 - \frac{u_0}{u_{Er}^*}\right).$$

The argument of the last square root in the Bessel function of (A6) can be simplified to become

$$(\ln(r/r_0))^2 + \frac{1}{A^*}(z + \tilde{a}\ln(r/r_0))^2 = (\ln(r/r_0))^2 - \frac{9\kappa^2}{u_{Er}^{*2}}\left(z + \frac{u_{Er}^*}{3\kappa}\ln(r/r_0)\right)^2 = -\left(\frac{3\kappa}{u_{Er}^*}\right)z\left[z + \frac{2u_{Er}^*}{3\kappa}\ln(r/r_0)\right].$$

Applying these results to (A6) gives

$$f(r,p) = \frac{dN/dt}{32\pi^3\kappa r_0^2 p_0^3}\sqrt{-\frac{9\kappa^2}{u_{Er}^{*2}}}\left(\frac{r}{r_0}\right)^{-(1-u_0/u_{Er}^*)}\left(\frac{p}{p_0}\right)^{3\kappa/u_{Er}^*(u_0/u_{Er}^* - (u_0+u_{Er}^*)/2\kappa)} \times K_0\left[\nu i\left(\frac{3\kappa}{u_{Er}^*}\right)\sqrt{z}\sqrt{z + \frac{2u_{Er}^*}{3\kappa}\ln(r/r_0)}\right].$$

A Hankel function can now be introduced using the identity $K_n(w) = -(i\pi/2)e^{-in\pi/2}\bar{H}_n^{(2)}(we^{-i\pi/2})$, where $\bar{H}$ is the Hankel function or Bessel function of the third kind valid for $-(\pi/2) < \mathrm{ph}(w) < \pi$. Considering that ν, $3\kappa/u_{Er}^*$, and z are all positive, then only the

last square root can affect the phase of the total argument of K_0. If we specify a phase of $\pi/2$ ($x = ix$‘, where $x' > 0$ in the identity), it implies in our application of the identity that the last square root must be real. Our requirement is then $z + 2u^*_{Er}/3\kappa \ln(r/r_0) > 0$. Since $z > 0$ by assumption, the inequality can only be violated when $r < r_0$ sufficiently. To fulfill the inequality in this case, we introduce the additional constraint $3\kappa/u^*_{Er} z + 2\ln(r/r_0) > 0$. After incorporating the Hankel function, and the abovementioned inequalities in terms of Heaviside step functions, the solution becomes

$$f(r,p) = \frac{3idN/dt}{32\pi^3 u^*_{Er} r_0^2 p_0^3}\left(\frac{r}{r_0}\right)^{-(1-u_0/u^*_{Er})}\left(\frac{p}{p_0}\right)^{3\kappa/u^*_{Er}(u_0/u^*_{Er}-(u_0+u^*_{Er})/2\kappa)}\left(-\frac{i\pi}{2}\right)$$
$$\times \overline{H}_0^{(2)}\left[\nu\left(\frac{3\kappa}{u^*_{Er}}\right)\sqrt{z}\sqrt{z + \frac{2u^*_{Er}}{3\kappa}\ln(r/r_0)}\right]\left[\left[1 - H(r - r_0)\right]H\left(\frac{3\kappa}{u^*_{Er}}z + 2\ln(r/r_0)\right) + H(r - r_0\right)\right].$$

Note that $\bar{H}_0^{(2)}(z) = J_0(z) - iY_0(z)$. Since we are not interested in the imaginary part of the solution (the distribution function should be real), we discard Y_0 in order to reproduce (E2) exactly, except for a factor of one half out front, because then

$$f(r,p) = \frac{1}{2}\frac{3dN/dt}{32\pi^2 u^*_{Er} r_0^2 p_0^3}\left(\frac{r}{r_0}\right)^{-(1-u_0/u^*_{Er})}\left(\frac{p}{p_0}\right)^{3\kappa/u^*_{Er}(u_0/u^*_{Er}-(u_0+u^*_{Er})/2\kappa)}$$
$$\times J_0\left[\nu\left(\frac{3K}{u^*_{Er}}\right)\sqrt{z}\sqrt{z + \frac{2u^*_{Er}}{3\kappa}\ln(r/r_0)}\right]\left[\left[1 - H(r - r_0)\right]H\left(\frac{3\kappa}{u^*_{Er}}z + 2\ln(r/r_0)\right) + H(r - r_0\right)\right]. \quad \text{(E4)}$$

Appendix F
Compression Acceleration Limit

F.1. Solution from the Parker Equation

Going back to Equation (A1) and ignoring terms that include u_{Er} and D_0, we get

$$\frac{\partial^2 f}{\partial r^2} - \left[\frac{u_0 - 3\kappa}{\kappa}\right]\frac{1}{r}\frac{\partial f}{\partial r} + \left[\frac{u^*/3}{\kappa}\right]\frac{1}{r^2}\frac{\partial f}{\partial z} + -\frac{f v_{\rm esc}}{\kappa r^2} = -\frac{dN/dt}{16\pi^2\kappa r_0^3 p_0^3}\delta(r - r_0)\delta(z), \quad \text{(F1)}$$

where $u^* = \overline{\langle \nu^I_{\rm COM}\rangle} - 2u_0$. Applying the Laplace transform as before yields

$$\frac{\partial^2 \overline{f}}{\partial r^2} - \left[\frac{u_0 - 3\kappa}{\kappa}\right]\frac{1}{r}\frac{\partial \overline{f}}{\partial r} + \left[-\frac{\mu u^*/3 - v_{\rm esc}}{\kappa}\right]\frac{1}{r^2}\overline{f} = -\frac{dN/dt}{16\pi^2\kappa r_0^3 p_0^3}\delta(r - r_0).$$

By applying again the approach outlined in Morse & Feshbach (1953), it can be shown that

$$\lambda_\pm = -\left(1 - \frac{u_0}{2\kappa}\right) \pm \sqrt{\left(1 - \frac{u_0}{2\kappa}\right)^2 - \mu\frac{u^*}{3\kappa} + \frac{v_{\rm esc}}{\kappa}}.$$

With the aid of the method of variation of parameters, we find that

$$\overline{f} = \frac{dN/dt}{32\pi^2\kappa r_0^2 p_0^3}\frac{1}{\sqrt{p'}}\left(\frac{r}{r_0}\right)^{-(1-u_0/2K)}\left[\left(\frac{r}{r_0}\right)^{\sqrt{p'}}[1 - H(r - r_0)] + \left(\frac{r}{r_0}\right)^{-\sqrt{p'}}H(r - r_0)\right],$$

where $p' = (1 - u_0/2\kappa)^2 + v_{\rm esc}/\kappa + \mu u^*/3\kappa$ and $\mu = 3\kappa/u^*[p' - (1 - u_0/2\kappa)^2 - v_{\rm esc}/\kappa]$. After evaluating the inverse Laplace transform of solution $\overline{f}$ with the aid of transform #6 on p. 246 in Erdélyi (1954), we finally get

$$f(r,p) = \frac{dN/dt}{32\pi^3 r_0^2 p_0^3}\sqrt{\frac{3\pi}{\kappa(\overline{\langle \nu^I_{\rm COM}\rangle} - 2u_0)\ln(p/p_0)}}\left(\frac{p}{p_0}\right)^{-3\kappa\frac{(1-u_0/2\kappa)^2+v_{\rm esc}/\kappa}{\overline{\langle \nu^I_{\rm COM}\rangle}-2u_0}}\left(\frac{r}{r_0}\right)^{-(1-u_0/2\kappa)} \times \exp\left[-\frac{1}{4}(\ln(r/r_0))^2\,\frac{\overline{\langle \nu^I_{\rm COM}\rangle} - 2u_0}{3\kappa\ln(p/p_0)}\right]. \tag{F2}$$

At the particle source position $r = r_0$, this solution simplifies to a pure power law in momentum given by

$$f(r,p) = \frac{dN/dt}{32\pi^3 r_0^2 p_0^3}\sqrt{\frac{3\pi}{\kappa(\overline{\langle \nu^I_{\rm COM}\rangle} - 2u_0)\ln(p/p_0)}}\left(\frac{p}{p_0}\right)^{-3\kappa\frac{(1-u_0/2K)^2+v_{\rm esc}/\kappa}{\overline{\langle \nu^I_{\rm COM}\rangle}-2u_0}}.$$

F.2. Compression Acceleration Limit of the Full Solution

Starting with (A6) (the full solution containing all the acceleration mechanisms), we want to see what limits we can take to get back (F2) (the solution only including compression acceleration). To begin, we set $u_{Er} = 0$. This gives the following simplifications: $A^* = D_0/\kappa(1 - u_{Er}^2/9\kappa D_0) \to D_0/\kappa$,

$$b = \sqrt{\left(1 - \frac{u_0 - u_{Er}}{2\kappa}\right)^2 + \frac{v_{\rm esc}}{\kappa} + \frac{D_0}{4\kappa}\frac{(3 - (1/3D_0)[\overline{\langle \nu^I_{\rm COM}\rangle} - u_0 u_{Er}/\kappa + u_{Er}^2/\kappa - 2u_0])^2}{1 - u_{Er}^2/9\kappa D_0}}$$
$$= \sqrt{\left(1 - \frac{u_0}{2\kappa}\right)^2 + \frac{v_{\rm esc}}{\kappa} + \frac{D_0}{4\kappa}\left(3 - \frac{u^*}{3D_0}\right)^2},$$

where $u^* = \overline{\langle \nu^I_{\rm COM}\rangle} - 2u_0$ as before. After applying $u_{Er} = 0$

$$\overline{a} - \frac{B}{2A}\tilde{a} = -\left(1 - \frac{u_0}{2\kappa}\right),$$

$$-\frac{B}{2A} = -\frac{3}{2} + \frac{1}{6D_0}\frac{\overline{\langle \nu^I_{\rm COM}\rangle} - u_0 u_{Er}/\kappa - 2u_0}{1 - u_{Er}^2/9\kappa D_0} = \frac{1}{2}\left(-3 + \frac{u^*}{3D_0}\right),$$

which means the distribution function becomes

$$f(r,p) = \frac{dN/dt}{32\pi^3 r_0^2 p_0^3\sqrt{D_0\kappa}}\left(\frac{r}{r_0}\right)^{-(1-u_0/2\kappa)}\left(\frac{p}{p_0}\right)^{1/2(-3+u^*/3D_0)} \times K_0\left[\sqrt{\left(1 - \frac{u_0}{2\kappa}\right)^2 + \frac{v_{\rm esc}}{\kappa} + \frac{D_0}{4\kappa}\left(3 - \frac{u^*}{3D_0}\right)^2}\sqrt{(\ln(r/r_0))^2 + \frac{\kappa z^2}{D_0}}\right].$$

After defining $q = -u^*/3D_0$ and letting $D_0 \to 0$, we find that $|q| \gg 1$, and thus $b = \sqrt{(1 - u_0/2\kappa)^2 + v_{\rm esc}/\kappa + D_0/\kappa(q/2)^2}$. Let us examine the argument of the modified Bessel function:

$$\sqrt{\left(1 - \frac{u_0}{2\kappa}\right)^2 + \frac{v_{\rm esc}}{\kappa} + \frac{D_0}{\kappa}\left(\frac{q}{2}\right)^2}\sqrt{(\ln(r/r_0))^2 + \frac{\kappa z^2}{D_0}} = \frac{|q|z}{2}\sqrt{1 + \frac{\kappa}{D_0}\frac{(1 - u_0/2\kappa)^2 + v_{\rm esc}/\kappa}{(q/2)^2}} \times \sqrt{1 + \frac{D_0}{\kappa z^2}(\ln(r/r_0))^2}.$$

Note the ordering of the size of the terms in the square roots given that $|q| \gg 1$ and $D_0 \ll 1$. This means that both square roots can be simplified to $\sqrt{1+x}$, where $x \ll 1$ followed by a Taylor expansion on each about $x = 0$ (i.e., $\sqrt{1+x} = 1 + x/2 - x^2/8 + x^3/16 - ...$). Keeping the first two terms of each expansion only, we see that the argument of the modified Bessel function becomes

$$\frac{|q|z}{2}\left[1 + \frac{\kappa}{2D_0}\frac{(1-u_0/2\kappa)^2 + v_{\rm esc}/\kappa}{(q/2)^2}\right]\left[1 + \frac{D_0}{2\kappa z^2}(\ln(r/r_0))^2\right] = z\left[\frac{|q|}{2} + \frac{\kappa}{2D_0}\frac{(1-u_0/2\kappa)^2 + v_{\rm esc}/\kappa}{(|q|/2)}\right]$$
$$\times\left[1 + \frac{D_0}{2\kappa z^2}(\ln(r/r_0))^2\right] = z\left[\underbrace{\frac{|q|}{2}}_{0(1/\varepsilon)} + \underbrace{3\kappa\frac{(1-u_0/2\kappa)^2 + v_{\rm esc}/\kappa}{u^*}}_{0(\varepsilon)}\right]$$
$$+ \frac{D_0}{2\kappa z}(\ln(r/r_0))^2\left[\underbrace{\frac{|q|}{2}}_{0(1)} + \underbrace{3\kappa\frac{(1-u_0/2\kappa)^2 + v_{\rm esc}/\kappa}{u^*}}_{0(\varepsilon^2)}\right].$$

Here, $\varepsilon \ll 1$, and therefore $D_0 \sim O(\varepsilon)$, $q \sim O(1/\varepsilon)$. Because we have a term of $O(1/\varepsilon)$, we can apply the large-argument limit of the modified Bessel function ($\lim_{z\to\infty} K_0(z) = \sqrt{\pi/2z}\,e^{-z}$). In order to reobtain (F2), we keep only the term of $O(1/\varepsilon)$ in the square root, because it gives the dominant contribution. However, in the exponent of the large-argument limit, only the terms of $O(1)$ and $O(\varepsilon)$ are retained so as not to let the solution decay to zero:

$$\sqrt{\frac{\pi}{2z|q|/2}}\left(\frac{p}{p_0}\right)^{-|q|/2 - 3\kappa\frac{(1-u_0/2\kappa)^2 + v_{\rm esc}/\kappa}{u^*}}\exp\left[-\frac{D_0}{4\kappa z}|q|(\ln(r/r_0))^2\right]$$
$$= \sqrt{\frac{3\pi D_0}{u^* z}}\left(\frac{p}{p_0}\right)^{-3\kappa\frac{(1-u_0/2\kappa)^2 + v_{\rm esc}/\kappa}{u^*}}\exp\left[-\frac{1}{4}(\ln(r/r_0))^2\frac{u^*}{3\kappa z}\right].$$

Plugging in this result, we see

$$f(r,p) = \frac{dN/dt}{32\pi^3 r_0^2 p_0^3}\sqrt{\frac{3\pi}{\kappa(\overline{\langle\nu^I_{\rm COM}\rangle} - 2u_0)\ln(p/p_0)}}\left(\frac{p}{p_0}\right)^{-3\kappa\frac{(1-u_0/2\kappa)^2 + v_{\rm esc}/\kappa}{\overline{\langle\nu^I_{\rm COM}\rangle} - 2u_0}}\left(\frac{r}{r_0}\right)^{-(1-u_0/2\kappa)}$$
$$\times\exp\left[-\frac{1}{4}(\ln(r/r_0))^2\frac{\overline{\langle\nu^I_{\rm COM}\rangle} - 2u_0}{3\kappa\ln(p/p_0)}\right], \tag{F3}$$

thus reproducing (F2).

Appendix G
The Separate Second-order Fermi SMFR Acceleration Mechanisms

le Roux et al. (2019) introduce their pitch angle averaged momentum diffusion coefficient as

$$D^I_{pp} = D^0_{pp} + D^{Icoh}_{pp} + D^{Istoch}_{pp}, \tag{G1}$$

which is made up of three different classes of momentum diffusion (le Roux et al. 2019). D^0_{pp} deals with momentum diffusion due to energetic particles undergoing pitch-angle scattering when interacting with the large-scale solar wind fields, and can be written as

$$D^0_{pp} = p^2\frac{1}{5}(\boldsymbol{b}_0\boldsymbol{b}_0 : \sigma^{\rm sh})^2\frac{\kappa^{I2}_\parallel}{v^2} + p^2\left[\left(\frac{q\boldsymbol{E}_0}{p} - \frac{1}{v}\frac{d\boldsymbol{u}_0}{dt}\right)\cdot\boldsymbol{b}_0\right]^2\frac{\kappa^{I1}_\parallel}{v^2},$$

where $\sigma^{\rm sh}$ is the solar wind shear flow tensor, $\boldsymbol{E}_0$ is the nonideal background electric field, $d\boldsymbol{u}_0/dt$ represents the acceleration of the solar wind flow, and $\kappa^{I1}_\parallel$ and $\kappa^{I2}_\parallel$ denote the parallel diffusion coefficient as a consequence of particle pitch-angle scattering by random magnetic mirroring forces in SMFRs that originate from the first anisotropic moment (superscript of "1") of the focused transport equation and the second anisotropic moment (superscript of "2") of the focused transport equation, respectively.

D_{pp}^{Icoh} makes up the second class of momentum diffusion generated because particles undergo pitch-angle scattering while they interact with mean SMFR fields (le Roux et al. 2019):

$$D_{pp}^{Icoh} = \overbrace{p^2\frac{1}{5}\left(\frac{1}{3}\langle\nu^I_{\rm COM}\rangle\right)^2\frac{\kappa_\parallel^{I2}}{v^2}}^{D^{Icoh}_{\rm COM}} + \overbrace{p^2\frac{1}{5}(\langle\nu^I_{\rm INC}\rangle)^2\frac{\kappa_\parallel^{I2}}{v^2}}^{D^{Icoh}_{\rm INC}} + \overbrace{p^2(\langle\nu^I_{\rm ACC}\rangle)^2\frac{\kappa_\parallel^{I1}}{v^2}}^{D^{Icoh}_{\rm ACC}} + \underbrace{p^2(\langle\nu^I_{E}\rangle)^2\frac{\kappa_\parallel^{I1}}{v^2}}_{D^{Icoh}_{E}},$$

which is made up of four separate SMFR mechanisms that all accelerate particles. $\langle\nu^I_{\rm COM}\rangle$ represents the average SMFR compression acceleration rate, $\langle\nu^I_{\rm INC}\rangle$ is the average incompressible parallel shear flow acceleration rate, $\langle\nu^I_{\rm ACC}\rangle$ is the mean SMFR parallel flow acceleration, and $\langle\nu^I_{E}\rangle$ is the acceleration rate associated with average turbulent motional electric field parallel to the guide/background magnetic field (le Roux et al. 2019).

The final class of momentum diffusion, D_{pp}^{Istoch}, is caused by particles responding to statistical fluctuations in the SMFR fields and can be expressed as (le Roux et al. 2019)

$$D_{pp}^{Istoch} = \overbrace{p^2\left[\frac{2}{15}\langle(\delta\nu^I_{\rm COM})^2\rangle\tau_{\rm dec1} - \left(\frac{2}{5}\langle\delta\nu^I_{\rm COM}\delta\nu^I_{\rm REF}\rangle\tau_{\rm dec1}\right)^2\frac{\kappa_\parallel^{I1}}{v^2}\right]}^{D^{Istoch}_{\rm COM}} + \overbrace{p^2\frac{1}{3}\langle(\delta\nu^I_{E})^2\rangle\tau_{\rm dec1}}^{D^{Istoch}_{E}}$$
$$+ \underbrace{p^2\left[\frac{1}{5}\langle(\delta\nu^I_{\rm INC})^2\rangle\tau_{\rm dec1} - \left(\frac{1}{5}\langle\delta\nu^I_{\rm INC}\delta\nu^I_{\rm REF}\rangle\tau_{\rm dec1}\right)^2\frac{\kappa_\parallel^{I1}}{v^2}\right]}_{D^{Istoch}_{\rm INC}} + \underbrace{p^2\frac{1}{3}\langle(\delta\nu^I_{\rm ACC})^2\rangle\tau_{\rm dec1}}_{D^{Istoch}_{\rm ACC}},$$

where $\langle(\delta\nu^I_{\rm COM})^2\rangle$ is the variance in the SMFR compression rate, $\delta\nu^I_{\rm REF}$ represents random fluctuations in the energetic particle pitch-angle rate of change due to fluctuations in the magnetic mirroring force in the SMFRs, $\langle(\delta\nu^I_{\rm REC})^2\rangle$ is the variance in the acceleration rate due to fluctuations in turbulent motional electric field parallel to the guide/background magnetic field, $\langle(\delta\nu^I_{\rm INC})^2\rangle$ is the variance in the SMFR incompressible parallel shear flow acceleration rate, and $\langle(\delta\nu^I_{\rm ACC})^2\rangle$ is the variance in the parallel reconnection electric field acceleration rate. See Equations (10)–(12) in le Roux et al. (2019) for details. Each momentum diffusion term is weighted by one of two timescales that determines its contribution to the total momentum diffusion coefficient. The two timescales of note are the scattering timescale ($\kappa_\parallel^{I1}/v^2$ or $\kappa_\parallel^{I2}/v^2$) and the decorrelation timescale ($\tau_{\rm dec}$). The scattering timescale is defined as the average timescale on which we would expect energetic particles to experience scattering and diffuse due to interaction with smaller, gyroscale-size SMFR scattering centers. These scattering centers are assumed to be present inside the main larger-scale SMFRs with which the energetic particles interact at the same time, the latter with gyroradii much smaller than the width of the main SMFRs. The decorrelation timescale, on the other hand, describes the timescale on which particles, diffusing inside the main, larger-scale SMFRs, experience decorrelated electromagnetic fields and plasma flow associated with the main SMFRs (diffusive crossing timescale). See le Roux et al. (2015) for more information. Thus, our theory operates in the strong scattering limit whereby the Parker-type transport equation we apply in this paper, limited to cases where the distribution function is nearly isotropic due to strong scattering, is an appropriate choice. Therefore, we expect the scattering timescale to be the smallest timescale in our problem. Consequently, because particles are scattering continuously inside SMFRs, we expect the scattering timescale to be the smallest timescale in the problem. Similarly, because particles are scattering the whole time that they are inside SMFRs, we expect $\tau_{\rm dec} \gg \kappa_\parallel^{I1}/v^2$ and $\kappa_\parallel^{I2}/v^2$, so we only retain the terms that do not include $\kappa_\parallel^{I1}/v^2$ or $\kappa_\parallel^{I2}/v^2$.

Therefore, only the third class of momentum diffusion D_{pp}^{Istoch} remains. This class focuses on stochastic acceleration due statistical fluctuations in SMFR flow and fields. In D_{pp}^{Istoch}, there are four stochastic acceleration mechanisms, as discussed above, which we label now as D_{pp}^{IE} because of the variance in the turbulent motional electric field parallel to the guide/background magnetic field $\langle(\delta\nu^I_{E})\rangle^2$, D_{pp}^{IACC} due to the variance in the acceleration of the plasma flow parallel to the SMFR magnetic island field component $\langle(\delta\nu^I_{\rm ACC})\rangle^2$, D_{pp}^{ISH} because of the variance in the SMFR plasma shear flow parallel to the SMFR magnetic island field component $\langle(\delta\nu^I_{\rm INC})\rangle^2$, and D_{pp}^{ICOM} due to the variance in the SMFR flow compression rate in the 2D plane perpendicular to the guide/background magnetic field of the $\langle(\delta\nu^I_{\rm COM})\rangle^2$. After recasting the four variance expressions in a useful form for application to observations of

SMFRs (for more details, see le Roux et al. 2018), the momentum diffusion coefficients can finally be expressed as

$$D_{pp}^{IE} = p^2 \frac{\sqrt{6c_k}}{24}\left[r_A^I - \frac{(\sigma_c^I)^2}{4}(r_A^I+1)^2\right]\left(\frac{\langle \delta B_I^2\rangle}{B_0^2}\right)^{3/2}\left(\frac{z}{A}\right)^2\left(\frac{v_{A0}}{v\gamma}\right)^2\left(\frac{L_{I\perp}^c}{d_i}\right)^2\left(\frac{v_{A0}}{v}\right)\frac{v_{A0}}{L_{I\perp}^c},$$

$$D_{pp}^{IACC} = p^2 \frac{\sqrt{6c_k}}{12}\left[r_A^I + \frac{3(\sigma_c^I)^2}{4}(r_A^I+1)^2\right]\left(\frac{\langle \delta B_I^2\rangle}{B_0^2}\right)^{3/2}\left(\frac{u_0\sin(\psi)}{v}\right)^2\left(\frac{v_{A0}}{v}\right)\frac{v_{A0}}{L_{I\perp}^c},$$

$$D_{pp}^{ISH} = p^2 \frac{\sqrt{6c_k}}{4}\left[r_A^I + \frac{41(\sigma_c^I)^2}{40}(r_A^I+1)^2\right]\left(\frac{\langle \delta B_I^2\rangle}{B_0^2}\right)^{5/2}\left(\frac{v_{A0}}{v}\right)\frac{v_{A0}}{L_{I\perp}^c},$$

$$D_{pp}^{ICOM} = p^2 \frac{\sqrt{6c_k}}{15}\left[r_A^I - \frac{1(\sigma_c^I)^2}{4}(r_A^I+1)^2\right]\left(\frac{\langle \delta B_I^2\rangle}{B_0^2}\right)^{1/2}\left(\frac{v_{A0}}{v}\right)\frac{v_{A0}}{L_{I\perp}^c},$$

where $L_{I\parallel}$ is the SMFR length along the guide field $\approx 2L_{I\perp}^c$ (Weygand et al. 2011); $L_{I\perp}^c$ is the SMFR diameter; γ is the Lorentz factor; v_{A0} is the Alfvén speed due to the guide field; $\langle \delta B_I^2\rangle$ is associated with the average magnetic energy density in the island; B_0^2 is associated with the magnetic energy density in the guide field; d_i is the ion inertial scale, or the gyroradius for the guide field if the particle speed equals the Alfvén speed due to the guide field

$$d_i = r_g(v = v_{A0}) = \frac{m_p v_{A0}}{eB_0} = \frac{m_p}{eB_0}\frac{B_0}{\sqrt{\mu_0\rho_0}};$$

r_A^I is the Alfvén ratio, defined by le Roux et al. (2018) as

$$r_A^I = \frac{\langle \delta u_I^2\rangle}{\langle \delta v_{AI}^2\rangle} = \langle \delta u_I^2\rangle\frac{\mu_0\rho_0}{\langle \delta B_I^2\rangle} = \langle \delta u_I^2\rangle\frac{\mu_0 m_p\langle N_p\rangle}{\langle \delta B_I^2\rangle};$$

σ_c^I is the normalized cross helicity in the island plane; Z/A is the atomic number over the atomic mass number in AMU; m_p is the rest mass of a proton; and $\langle N_p\rangle$ is the average particle density in the SMFR. The c_k term,

$$\begin{aligned} c_k &= \frac{\pi}{2}\frac{L_{I\parallel}}{L_{I\perp}^c}\left(\frac{\langle \delta B_I^2\rangle}{B_0^2}\right)^{1/2} (\tau_{\kappa_\parallel^I} \ll \tau_{\kappa_\perp^I}),\\ &= 1 (\tau_{\kappa_\parallel^I} \leqslant \tau_{\kappa_\perp^I}),\end{aligned}$$

is determined by the parallel ($\tau_{\kappa_\parallel^I} = L_{I\parallel}^2/\kappa_\parallel^I$) and perpendicular diffusion timescales ($\tau_{\kappa_\perp^I} = (L_{I\perp}^c)^2/\kappa_\perp^I$). However, because the analytical solutions only apply to $D_0 = r_0 D_{pp}^{Istoch}$ values for momentum diffusion that are independent of particle speed, even though all the contributions to D_{pp}^{Istoch} are a function of particle speed, we average the above expressions over a specified range of particle speeds consistent with the observed range of SMFR acceleration events:

$$\begin{aligned}
D_0^{ICOM} &= r_0\left\langle\frac{D_{pp}^{ICOM}}{p^2}\right\rangle_v = \frac{\sqrt{6c_k}}{15}\left[r_A^I - \frac{(\sigma_c^I)^2}{4}(r_A^I+1)^2\right]\left(\frac{\langle \delta B_I^2\rangle}{B_0^2}\right)^{1/2}\left(\frac{v_{A0}}{v_{\max}-v_{\min}}\right)\ln\left(\frac{v_{\max}}{v_{\min}}\right)\frac{v_{A0}r_0}{L_{I\perp}^c},\\
D_0^{ISH} &= r_0\left\langle\frac{D_{pp}^{ISH}}{p^2}\right\rangle_v = \frac{\sqrt{6c_k}}{4}\left[r_A^I + \frac{41(\sigma_c^I)^2}{40}(r_A^I+1)^2\right]\left(\frac{\langle \delta B_I^2\rangle}{B_0^2}\right)^{5/2}\left(\frac{v_{A0}}{v_{\max}-v_{\min}}\right)\ln\left(\frac{v_{\max}}{v_{\min}}\right)\frac{v_{A0}r_0}{L_{I\perp}^c},\\
D_0^{IACC} &= r_0\left\langle\frac{D_{pp}^{IACC}}{p^2}\right\rangle_v = \frac{\sqrt{6c_k}}{12}\left[r_A^I + \frac{3(\sigma_c^I)^2}{4}(r_A^I+1)^2\right]\left(\frac{\langle \delta B_I^2\rangle}{B_0^2}\right)^{3/2}\left(\frac{(u_0 sin(\psi))^2(v_{\max}^2 - v_{\min}^2)}{2v_{\max}^2 v_{\min}^2}\right)\\
&\quad\times\left(\frac{v_{A0}}{v_{\max}-v_{\min}}\right)\frac{v_{A0}r_0}{L_{I\perp}^c},\\
D_0^{IE} &= r_0\left\langle\frac{D_{pp}^{IE}}{p^2}\right\rangle_v = \frac{\sqrt{6c_k}}{24}\left[r_A^I - \frac{(\sigma_c^I)^2}{4}(r_A^I+1)^2\right]\left(\frac{\langle \delta B_I^2\rangle}{B_0^2}\right)^{3/2}\left(\frac{Z}{A}\right)^2\left(\frac{L_{I\perp}^c}{d_i}\right)^2\left(\frac{v_{A0}}{v_{\max}-v_{\min}}\right)\\
&\quad\times\left[\frac{v_{A0}^2(v_{\max}^2 - v_{\min}^2)}{2v_{\max}^2 v_{\min}^2} - \left(\frac{v_{A0}}{c}\right)^2\ln\left(\frac{v_{\max}}{v_{\min}}\right)\right]\frac{v_{A0}r_0}{L_{I\perp}^c},
\end{aligned} \tag{G2}$$

where $v_{\max}$ and $v_{\min}$ are determined from the energy ranges over which each event is fit.

ORCID iDs

Keaton Van Eck https://orcid.org/0000-0002-8303-8105
Jakobus le Roux https://orcid.org/0000-0001-9199-2890
Yu Chen https://orcid.org/0000-0002-0065-7622
Ling Ling Zhao https://orcid.org/0000-0002-4299-0490
Noah Thompson https://orcid.org/0000-0002-9603-3370

References

Adhikari, L., Zank, G. P., & Zhao, L.-L. 2019, ApJ, 873, 72
Bieber, J. W., Wanner, W., & Matthaeus, W. H. 1996, JGRA, 101, 2511
Bonamente, M. 2013, Statistics and Analysis of Scientific Data (New York: Springer)
Cane, H. V., Reames, D. V., & von Rosenvinge, T. T. 1988, JGR, 93, 9555
Cartwright, M. L., & Moldwin, M. B. 2010, JGRA, 115, A08102
Che, H., & Zank, G. P. 2020, ApJ, 889, 11
Chen, Y., & Hu, Q. 2020, ApJ, 894, 25
Chen, Y., Hu, Q., & le Roux, J. A. 2019, ApJ, 881, 58
Chian, A. C.-L., Feng, H. Q., Hu, Q., et al. 2016, ApJ, 832, 179
Dahlin, J. T., Drake, J. F., & Swisdak, M. 2017, PhPl, 24, 092110
Drake, J. F., Swisdak, M., & Fermo, R. 2013, ApJL, 763, L5
Drake, J. F., Swisdak, M., Schoeffler, K. M., Rogers, B. N., & Kobayashi, S. 2006, GeoRL, 33, L13105
Drury, L. O. 1983, RPPh, 46, 973
Erdélyi, A. 1954, Tables of Integral Transforms: Based, in Part, on Notes Left by Harry Bateman, Tables of Integral Transforms: Based, in Part, on Notes Left by Harry Bateman No. v. 1 (New York: McGraw-Hill)
Gosling, J. T., Skoug, R. M., Haggerty, D. K., & McComas, D. J. 2005, GeoRL, 32, L14113
Hu, Q., Zheng, J., Chen, Y., le Roux, J., & Zhao, L. 2018, ApJS, 239, 12
Hunana, P., & Zank, G. P. 2010, ApJ, 718, 148
Jones, F., & Ellison, D. 1991, SSRv, 58, 259
Karimabadi, H., Roytershteyn, V., Vu, H., et al. 2014, PhPl, 21, 062308
Khabarova, O., Zank, G. P., Li, G., et al. 2015, ApJ, 808, 181
Khabarova, O. V., & Zank, G. P. 2017, ApJ, 843, 4
Khabarova, O. V., Zank, G. P., Li, G., et al. 2016, ApJ, 827, 122
Lario, D., Ho, G. C., Decker, R. B., et al. 2003, in AIP Conf. Proc. 697, SOLAR WIND TEN: Proc. of the Tenth Int. Solar Wind Conf. (Melville, NY: AIP), 640
le Roux, J. A., & Webb, G. M. 2007, ApJ, 667, 930
le Roux, J. A., Webb, G. M., Khabarova, O. V., Zhao, L.-L., & Adhikari, L. 2019, ApJ, 887, 77
le Roux, J. A., Zank, G. P., & Khabarova, O. V. 2018, ApJ, 864, 158
le Roux, J. A., Zank, G. P., Webb, G. M., & Khabarova, O. 2015, ApJ, 801, 112
le Roux, J. A., Zank, G. P., Webb, G. M., & Khabarova, O. V. 2016, ApJ, 827, 47
Li, X., Guo, F., Li, H., & Li, G. 2015, ApJL, 811, L24
Li, X., Guo, F., & Liu, Y.-H. 2021, PhPl, 28, 052905
Malandraki, O., Khabarova, O., Bruno, R., et al. 2019, ApJ, 881, 116
Marsch, E., & Tu, C. Y. 1992, in COSPAR Coll. Ser. 3, Solar Wind Seven (Paris: Committee on Space Research), 549
Matsumoto, Y., Amano, T., Kato, T. N., & Hoshino, M. 2015, Sci, 347, 974
Matthaeus, W. H., Goldstein, M. L., & Roberts, D. A. 1990, JGRA, 95, 20673
Morse, P. M., & Feshbach, H. 1953, Methods of Theoretical Physics (New York: McGraw-Hill)
Porsche, H. 1975, RF, 19, 223
Vlahos, L., & Isliker, H. 2018, PPCF, 61, 014020
Weygand, J., Matthaeus, W., Dasso, S., & Kivelson, M. 2011, JGRA, 116, A08102
Xia, Q., & Zharkova, V. 2020, A&A, 635, A116
Zank, G. P., Adhikari, L., Hunana, P., et al. 2017, ApJ, 835, 147
Zank, G. P., Dosch, A., Hunana, P., et al. 2011, ApJ, 745, 35
Zank, G. P., Hunana, P., Mostafavi, P., et al. 2015, ApJ, 814, 137
Zank, G. P., le Roux, J. A., Webb, G. M., Dosch, A., & Khabarova, O. 2014, ApJ, 797, 28
Zank, G. P., & Matthaeus, W. H. 1992, JPlPh, 48, 85
Zank, G. P., & Matthaeus, W. H. 1993, PhFlA, 5, 257
Zhao, L.-L., Zank, G. P., Hu, Q., et al. 2019, ApJ, 886, 144
Zhao, L.-L., Zank, G. P., Khabarova, O., et al. 2018, ApJL, 864, L34
Zheng, J., Hu, Q., Chen, Y., & le Roux, J. 2017, JPhCS, 900, 012024